PHASE-FIELDS AND THE RENORMALIZATION GROUP: A CONTINUUM APPROACH TO MULTISCALE MODELING OF MATERIALS

BY

BADRINARAYAN P. ATHREYA

B. E., University of Bombay (V. J. T. I.), 2000
M. S., University of Colorado at Boulder, 2002

THESIS

Submitted in partial fulfillment of the requirements
for the degree of Doctor of Philosophy in Mechanical Engineering
in the Graduate College of the
University of Illinois at Urbana-Champaign, 2006

Urbana, Illinois

Abstract

Important phenomena in materials processing, such as dendritic growth during solidification, involve a wide range of length scales from the atomic level up to product dimensions. The phase-field approach, enhanced by optimal asymptotic methods and adaptive mesh refinement, copes with a part of this range of scales, from few tens of microns to millimeters, and provides an effective continuum modeling technique for moving boundary problems. A serious limitation of the usual representation of the phase-field model however, is that it fails to keep track of the underlying crystallographic anisotropy, and thus is unable to capture lattice defects and model polycrystalline microstructure without non-trivial modifications. The phase-field crystal (PFC) model on the other hand, is a phase field equation with periodic solutions that represent the atomic density. It natively incorporates elasticity, and can model formation of polycrystalline films, dislocation motion and plasticity, and nonequilibrium dynamics of phase transitions in real materials. Because it describes matter at the atomic length scale however, it is unsuitable for coping with the range of length scales in problems of serious interest. This thesis takes a first step towards developing a unified multiscale approach spanning all relevant lengths, from the nanoscale up, by combining elements from the phase-field and phase-field crystal modeling approaches, perturbative renormalization group theory, and adaptive mesh refinement.

A chapter of this thesis also examines the effect of confinement on dendritic growth, during equiaxed solidification in a pure material and the directional solidification of a dilute binary alloy, using phase-field models.

For my parents and Vaish

Acknowledgements

I take this opportunity to thank my advisors, Professors Jonathan Dantzig and Nigel Goldenfeld, for their wisdom and direction that has largely shaped this work, and also for the independence granted to me to pursue my ideas. Their advice has proved an invaluable asset to my education and professional development at UIUC. I also thank them both for being such wonderful teachers, specifically Jon for his *Materials Processing* course which stimulated my interest in modeling and computation. I am indebted to Nigel for introducing me to powerful methods in mathematical physics, such as *Renormalization Group Theory* and *Perturbation Theory*, which were crucial to progress. I finally thank them both for taking a sincere interest in my career, and for bringing several wonderful employment opportunities to my attention.

A word of thanks to our various collaborators—Mike Greenwood and Professor Nik Provatas at McMaster University for being kind enough to share their adaptive grid module and visualization software with us, Professor Ken Elder at Oakland University for several valuable discussions, and Jun-Ho Jeong and Shan Liu for their finite element code and directional solidification data, respectively, without which the work reported in Chapter 2 would not have been possible.

I also wish to thank—Professor Charles Tucker, for encouraging me to apply for the Teaching Fellowship and also for being my inspiration to teach which culminated in one of my most satisfying experiences as a graduate student, Professor Armand Beaudoin for discussions and career advice, all my teachers here at UIUC, M. E. department staff—Amanda Houser, and Kathy Smith for their general help and support, and Christopher Goldsmith for computer-related support.

I have really enjoyed working with my present and former colleagues—Anthony, Zhi, Roy, Shawn, and Mark, and am grateful for their help and advice in various matters, and interesting conversation on practically everything. I thank Anthony Chang for his useful inputs as we both contemplated our career paths, and Roy Maske for being a dependable and true friend. I also thank Nicholas Guttenberg, for several eye-opening discussions that taught me something new each time, and my friends Deepak and Satya, for their company and conversation over numerous cups of coffee. I was very lucky in the last year to have had terrific roommates in Pinaki, Sandeep and Tapan, whose friendship, camaraderie, and insanity, provided a happy diversion from work.

Finally, I thank my parents and my wife Vaishnevi for their unconditional love and support through different stages in my academic life, and to them I dedicate my work.

I gratefully acknowledge the financial support that this work received from the National Science Foundation via grant NSF-DMR-01-21695, and the Mechanical and Industrial Engineering Alumni Association Teaching Fellow Award in 2005.

The sciences do not try to explain, they hardly even try to interpret, they mainly make models. By a model is meant a mathematical construct which, with the addition of certain verbal interpretations, describes observed phenomena. The justification of such a mathematical construct is solely and precisely that it is expected to work.

—Neumann (1903-1957)

Table of Contents

List of Figures

List of Tables

Chapter 1

Introduction

1.1 Problem definition

A fundamental theoretical and computational challenge in materials modeling is that of simultaneously capturing dynamics occurring over a wide range of length and time scales, under processing conditions. The challenge stems from the fact that unlike simple crystalline solids, real materials, which are produced under a wide range of processing conditions, are polycrystalline, and contain lattice imperfections, dislocations and grain boundaries that have a strong bearing on mechanical response. Accurate prediction of emergent material properties requires resolution of phenomena from the nanoscale up. A classic example of such a multiscale problem is dendritic growth, a phenomenon seen in the solidification of undercooled melts, which involves the capillary length $\sim 10^{-9}$m, the scale of the pattern $\sim 10^{-6}$m, and the diffusion length $\sim 10^{-4}$m, which together span length scales over five orders of magnitude, and heat/solute transport through diffusion which occurs on time scales of $\sim 10^{-3}$s. Dislocation modeling is another multiscale problem where atomic resolution is needed at the level of the dislocation core (order of angstroms), while long range elastic field interactions are typically treated with a continuum description. Fig. 1.1 depicts broadly, some of the key problems of interest to materials scientists at their relevant length and time scales.

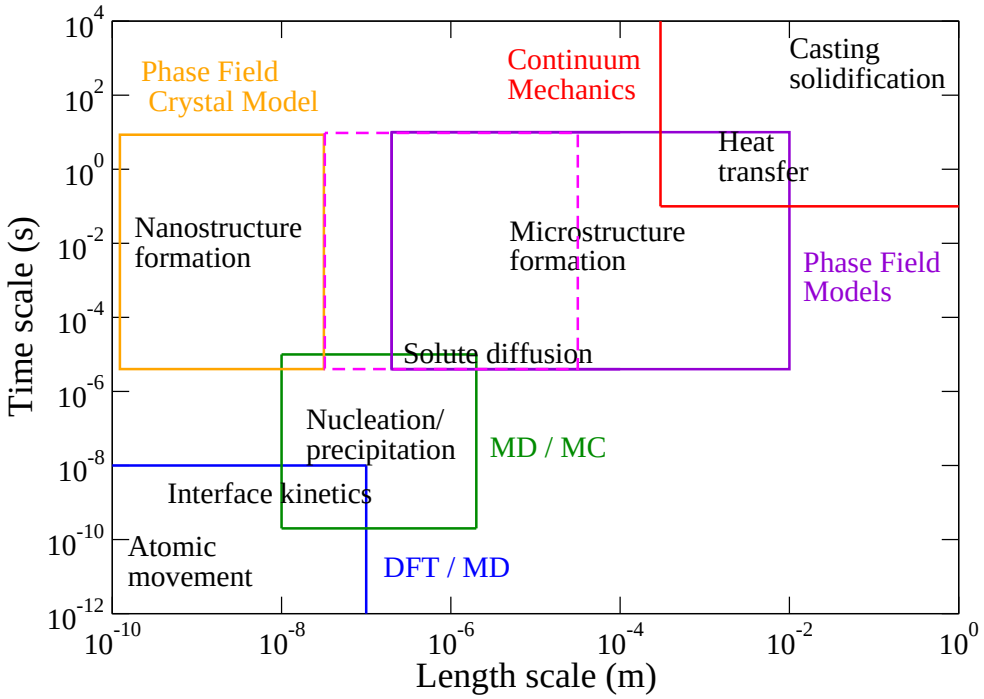

Figure 1.1: Materials phenomena and modeling approaches at various length and time scales.

Thus, progress in rational material design requires a fundamental understanding of the way in which important properties, such as hardness, yield strength, fracture toughness, and ductility, emerge as the mesoscale is approached, which is intricately connected to the physics at smaller length scales. The question we wish to address in this dissertation is, how can the properties at nano-, meso- and intermediate scales simultaneously be captured quantitatively and predictively?

1.2 Approach

A number of computational approaches to handle the range of length scales have been proposed recently [1], including quasi-continuum methods [2–5], the heterogeneous multiscale method [6, 7], multi-scale molecular dynamics [8–11], multigrid variants [12] and phase field models [13–16]. Some of these use a combination of two or more of the following schemes (atomistic and continuum models), as appropriate, for different levels of

resolution: density functional methods that provide a quantum mechanical description, which is necessary when there is significant departure from equilibrium conditions, for example, at the tip of a crack or in a chemical reaction; molecular dynamics or Monte Carlo methods when deviations from equilibrium are smaller, and a coarse-grained description with continuum fields at the mesoscale where equilibrium conditions are anticipated. A notable example is the quasi-continuum method [2–5] which combines molecular dynamics on the fine scale with finite element analysis at a coarser level and has had some measure of success in simulating fracture and predicting interactions between a few isolated dislocations. A handicap that diminishes the effectiveness, and hence limits the application of several of these methods, is the process of merging descriptions at different levels. Lack of a continuous transition between scales can induce artifacts, such as spurious reflections in a transition region between two levels, and is a major theoretical challenge [7, 17].

One *continuum* approach that has had plenty of success of late in the multiscale modeling of solidification problems, is the phase-field model, which through effective use of adaptive mesh refinement [18, 19], now spans $3-4$ orders of magnitude in length scales from micron up (see Fig.1.1). However, it suffers from being unable to model polycrystalline systems (a worthy exception being an extension developed by Kobayashi and co-workers [20, 21], and Warren [16]), and elastic and plastic effects without complicated augmentation [22–26], and is therefore limited in its application.

Keeping as our principal objective, the ability to model polycrystalline microstructure while resolving nanoscale defects, we propose a novel *continuum* approach to these difficulties in this dissertation, by combining the phase field crystal (PFC) formalism [27, 28] with renormalization group (RG) [29, 30] and related methods (see, e.g. [31]), developed for the analysis of hydrodynamic instabilities in spatially-extended dynamical systems [32–39]. We present coarse-grained equations, from which the atomic density can readily be reconstructed, and show that this approach is capable of generating high fidelity representations of materials processing dynamics. Moreover, we demonstrate that these equations—analogues of rotationally-covariant amplitude and phase equations in

fluid convection [40]—are computationally tractable and amenable to adaptive grid techniques, which allows modeling across scales.

Our approach is based on a form of the RG which unifies singular perturbation theory [32], and is a fully systematic way to extract universal or large scale structures from spatially-extended dynamical systems. The basic idea is to start, not with a molecular dynamics model at the nanoscale, but with a density functional description (in this context, the phase field crystal model [27, 28], see Fig. 1.1), whose equilibrium solutions are periodic density modulations. A system that is periodic at the nanoscale can be parameterized in terms of a uniform phase vector and an amplitude: the amplitude describes the maximum variations in the density of the system through the unit cell, while the phase vector describes spatial rotations. A system with underlying periodicity, but which also contains defects or other nanostructure, can be represented by a density wave whose amplitude is practically constant everywhere except near a defect, and a phase vector that is essentially uniform inside crystals, varying near grain boundaries and defects. This observation suggests that the amplitude/phase of the density are appropriate dynamical variables to use for describing spatially-modulated nanoscale structure in a mesoscopic system. Once these quantities are determined, the actual structure at the nanoscale (and above) can be reconstructed. Because the field variables themselves (not the density) are spatially mostly uniform, adaptive mesh refinement can be used effectively to extend the nanoscale modeling capability of the PFC model to micro- length scales, as shown by the dashed box in Fig. 1.1.

1.3 Dissertation outline

We start off in Chapter 2 by studying a simple problem pertaining to the solidification of pure materials and dilute binary alloys in confinement, where we investigate the effect of finite boundaries on interface morphology and dendrite tip selection using a standard three dimensional phase-field model. Our results highlight the power of this modeling technique. We discuss some of its limitations in Chapter 3 while laying the foundation for

another type of phase-field model, the PFC model [27,28]. We describe the mathematics of this model in detail and then present a gallery of results which illustrates its versatility as well as its limitations. We devote Chapter 4 entirely to the derivation of coarse-grained amplitude and phase equations from the PFC model using: (a) different variants of the RG and (b) the method of multiple scales, in the process discovering an operating order ambiguity in the current implementation of the RG methods which leads to a discrepancy between results obtained from (a) and (b). We propose a resolution to this ambiguity, which leads to the convergence of all methods at a certain order in the perturbation expansion. We numerically validate these equations in Chapter 5, via quantitative comparisons with solutions to the PFC equation, and demonstrate their computational advantage over the PFC equation. In Chapter 6, we develop a hybrid adaptive grid implementation of the amplitude/phase equations which allows us to extend the modeling capability of the PFC equation to micro- length scales. We conclude in Chapter 7 with some future directions for our work.

1.4 Publications

Parts of this thesis have already been published in peer-reviewed journals and conference proceedings. Chapter 2 in its entirety will appear in the September issue of *Philosophical Magazine* [41] (2006), while parts of it have already appeared in *TMS Proceedings* [42] (2004) and the *International Journal of Modern Physics* [43] (2005). Chapter 4 has been published in *Physical Review E* [44] (2006). Parts of Chapter 5 have appeared in *Physical Review E* [45] (2005) and the *Journal of Statistical Physics* [46] (2006). Chapter 6 is pending submission to *Physical Review E*.

Chapter 2

Solidification in Confinement

2.1 Background

Dendrites are one of the basic microstructural patterns seen in solidified metals. The mechanical behavior of the solidified product is often decided by the length scales set by these patterns. Study of dendritic growth is therefore motivated by the need to predict these length scales. The fundamental quantities that completely describe the growth of a dendrite at steady state under a given set of external conditions are its tip velocity and radius, which together define the so called "operating state". Despite considerable advances in the understanding of solidification science, discrepancies still arise when one attempts to compare theoretical predictions of dendrite operating states with experimental observations. We find that some of these discrepancies derive from differences between the ideal conditions assumed in theoretical treatments, and those experienced by materials under actual experimental situations.

The first theoretical treatment of the "free" dendrite growth problem was presented by Ivantsov [47]. He considered a pure dendrite, modeled as a paraboloid of revolution with tip curvature ρ_{tip}, growing into an infinite undercooled melt with temperature $T \to T_\infty$ far from the advancing tip. The dendrite was assumed to be isothermal at the melting temperature T_m, and to be growing along its axis at constant velocity V_{tip} in a shape-preserving way. Ivantsov found a solution to the thermal transport problem, in which the

dimensionless undercooling $\Delta = (T_m - T_\infty)/(L_f/c_p) = \mathcal{I}(Pe)$ where $Pe = \rho_{tip}V_{tip}/2D$ is the Péclet number, D is the thermal diffusivity, and $\mathcal{I}$ is the Ivantsov function. The temperature has been scaled by the characteristic temperature L_f/c_p, with L_f being the latent heat of fusion and c_p the specific heat.

This solution presented a conundrum, because it showed that the transport problem alone did not uniquely specify the operating state of the dendrite, i.e., the single combination of ρ_{tip} and V_{tip} observed in experiments. Additional considerations, such as the effect of curvature on the melting point [48], stability [49, 50] and eventually the anisotropy of the surface tension [51–53], led to a second condition $\sigma^* = 2d_0D/\rho_{tip}^2V_{tip}$ where σ^* is called the *selection constant*, and d_0 is the capillary length. The combination of Ivantsov's solution (modified for surface tension and its anisotropy) and the condition σ^* is constant gives a unique operating state. Numerical simulations using the phase-field method [14] at large values of Δ, have found agreement with the predictions of this body of work, known as *microscopic solvability theory.*

Glicksman and co-workers developed experimental techniques for studying the solidification of pure materials, with the objective of observing the operating state. They performed experiments with phosphorous [54], and transparent analog alloys like succinonitrile (SCN) [55] and pivalic acid (PVA) [56]. The results of these careful experiments found some areas of agreement with microscopic solvability theory, in particular, the value of σ^* was found to be constant, but the operating combination of ρ_{tip} and V_{tip} did not agree. Provatas, *et al.* were able to explain this discrepancy by showing that for the low undercooling conditions found in the experiments, interaction between neighboring dendrite branches [57, 58] affected the operating state.

Experiments have also been performed to examine the role of superimposed fluid flow on dendritic growth. Gill and coworkers [59, 60] used SCN in a special cylindrical chamber with a bellows to effect fluid flow. Bouissou and Pelcé [61] performed experiments with a flowing alloy of PVA and a seed confined between microscope slides. Saville and Beaghton [62] presented a theoretical analysis which extended Ivantsov's solution to consider the superimposed flow. Jeong *et al.* [19] performed phase-field simulations of these

experiments, and once again found discrepancies with theory. They conjectured that the differences arose because of the effect of finite containers in the experiments, leading to boundary conditions which differed from the assumptions of infinite media used in the theory.

Dendrite tip theories for constrained growth, such as directional solidification of dilute binary alloys between microscope slides, have been developed by Trivedi [63] and, Kurz and Fisher [64]. They have shown that a relationship of the form $\rho_{tip}^2 V_{tip} =$ constant, should hold for constrained growth just as in free dendrite growth. Early experiments by Somboonsuk *et al.* [65] in samples with slide separation greater than 150 μm have shown excellent agreement with this theory. However, in recent studies Liu *et al.* [66] have demonstrated that experimental results start to deviate significantly from theory when the slide separation approaches the scale of the primary dendrite spacing.

In this chapter, the role of confinement on dendritic growth will be studied systematically. Since *every* experiment is performed in a finite container, this finite size effect cannot be ignored. Our numerical experiments are conducted using phase-field models for both pure materials as well as binary alloys. For the binary alloy, recent experimental data from Liu *et al.* [66], provides us with a nice benchmark against which to test our numerical predictions.

2.2 Phase-field modeling

2.2.1 Phase-field model, adaptive grids and numerical methods

The objective in a general solidification problem is to solve the equations governing thermal and solute transport, subject to boundary conditions on the solid-liquid interface (moving boundary) and elsewhere. If melt convection is to be modeled, one needs to solve the momentum equations for fluid flow simultaneously with the above transport equations. Imposing the interface boundary conditions upon discretizing the governing equations poses a difficulty however, since the interface, as it evolves, will not in general align itself with a fixed set of mesh points.

The phase-field method eliminates the sharp liquid-solid boundary by introducing evolution equations for a continuous order parameter $\phi \in [-1, 1]$, where $\phi = -1, +1, 0$ corresponds to liquid, solid and interface respectively. Thus, the arduous task of solving the transport equations separately in liquid and solid domains while simultaneously satisfying boundary conditions on arbitrarily shaped interfaces, is replaced by that of solving a system of coupled differential equations; one for the evolution of ϕ and one for each of the transport variables (temperature, concentration and velocity). Phase-field modeling has been an active area of research in the past decade, and we refer the interested reader to original work by Langer [13], Karma and Rappel [14], and Beckermann *et al.* [15] for derivations of the phase-field equations and selection of phase-field parameters ensuring convergence to the original sharp interface problem.

The phase-field model introduces a parameter W_0 that connotes the finite width of the now 'smeared' interface. Karma and Rappel [14] showed that the model converges to the sharp interface equations when $p = W_0 V_{tip}/D \ll 1$, where D is the thermal or concentration diffusion coefficient, and V_{tip} is the nominal tip velocity of the dendrite. Resolving the interface on a discrete mesh requires that the mesh spacing $\Delta x \sim W_0$, while demanding that the diffusion field not interact with the boundaries leads to the domain size $L_B \gg D/V_{tip}$. Satisfying these requirements causes calculations on regular meshes to quickly reach the limit of available computing resources. For example, if we choose $p = 0.01$, fix $L_B V_{tip}/D = 10$, and enforce $\Delta x = W_0$, then we find that the number of grid points per dimension on a regular mesh should be at least $L_B/W_0 = 1000$. This makes computations challenging on regular meshes even in 2-D, while 3-D computations may not be practical at all, depending on available computing power.

We have mitigated this problem successfully by solving the equations on an adaptive finite element mesh [19, 58]. In three dimensions, we use eight-noded trilinear brick elements stored using an octree data structure. A local error estimator indicates refinement or coarsening of the mesh, and this permits tracking of the interface as well as resolution of gradients in the other fields. There are six degrees of freedom at each node (three velocities, pressure, temperature/concentration and ϕ), and a typical computation reaches

well over one million unknowns. The finest elements (Δx_{min}), which are distributed near the interface, now need to be order of W_0.

For our studies on pure materials, we have used a finite element discretization of the 3-D phase-field model developed by Karma and Rappel [14]. In order to account for the effects of melt convection we adopt the formulation presented by Beckermann *et al.* [15], who use an averaging method for the flow equations coupled to the phase-field. By appropriate choice of phase-field parameters we have ensured zero interface kinetics, which is a valid assumption for the range of undercooling we are concerned with.

For our alloy simulations, we have used Karma's one sided (vanishing solid diffusivity) phase-field model [67, 68], with a frozen temperature approximation. In a directional solidification arrangement, for certain values of the problem parameters (particularly when simulating real materials), a considerable amount of time can elapse before the transients vanish and the solid-liquid interface reaches steady state. In that time, the interface can encounter the end of the simulation box if the equations are solved in a reference frame that is fixed globally, and if the box is not large enough to contain the diffusion field. To alleviate this difficulty, we have solved the phase-field equations in a coordinate frame translating with the pulling speed. This saves some computational expense by allowing us the use of smaller boxes. We have not investigated the effect of melt convection in our numerical experiments with alloys.

In a recent article, Echebarria *et al.* [68] have emphasized that the same choice of phase-field parameters that produced zero interface kinetics in the pure material cannot also ensure this condition in the alloy model. This is due to the presence of certain additional terms in the kinetic parameter β, that arise out of accounting for the discontinuity in the concentration field at the interface in a model with vanishing solid diffusivity. To ensure that the kinetic coefficient is negligible at the interface, the phase-field relaxation time τ needs to be made temperature dependent in this region by setting

$$\tau = \tau_0 \left[1 - (1-k) \frac{z - V_p t}{l_T} \right]. \tag{2.1}$$

Here τ_0 is the usual relaxation time, k is the partition coefficient, z is the distance from the interface, V_p is the pulling velocity, t is time and l_T is the thermal length [67].

We evolve the nonlinear order parameter equation using a Forward-Euler time stepping scheme, while the linear thermal/solute transport equations are solved using the Crank-Nicholson scheme with a diagonally preconditioned conjugate gradient solver. The transport equations typically converge in fewer than five iterations per time step. The 3-D flow equations for the pure material are solved using the semi-implicit approximate projection method (SIAPM) [69]. Details of the above numerical methods and the finite element formulation are omitted here, as they have been presented elsewhere [19].

2.2.2 Geometry, initial and boundary conditions

Our three dimensional simulation domain is the rectangular parallelepiped illustrated in Fig. 2.1, with edge lengths along the x, y and z axes; L_x, L_y and δ respectively. The edges of the box are oriented along $\langle 100 \rangle$ cubic crystallographic directions.

For the pure material, the initial condition is a spherical solid seed with a radius greater than the critical nucleation radius, centered at the origin depicted in Fig. 2.1. Because of the inherent symmetry in the growth of the seed, it is usually sufficient to model one octant in three dimensional space. However, if forced fluid convection is incorporated along a particular direction, then the solidification rates into and counter to this direction become unequal. For example, if there is a flow parallel to the x axis, $x = 0$ is no longer a plane of symmetry. To account for this break in symmetry, we have to model at least a quadrant of space, with $z = 0$ and $y = 0$ as planes of symmetry.

In the simulations with the pure material, the dimensionless thermal field u is subjected to zero flux ($\nabla u \cdot \mathbf{n} = 0$) boundary conditions on all surfaces. Fluid flow, when it is included in our study, is imposed as an inlet boundary condition U_∞, normal to the face $x = -L_x/2$. The velocity field is subjected to symmetry boundary conditions on the domain walls, and is forced to vanish in the solid ($\phi = 1$) by an appropriate formulation of the momentum equations (see [15]). We fix the lateral dimensions of the simulation box ($L_x = 512$ and $L_y = 256$ are typical values), and study the interface evolution as a

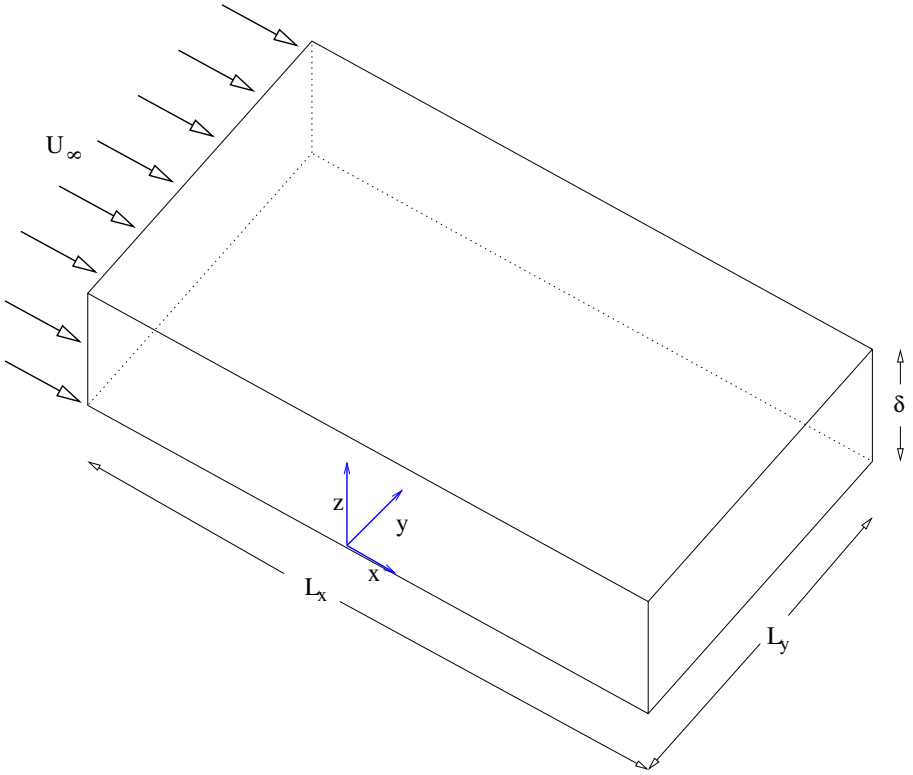

Figure 2.1: Simulation Domain. All surfaces are modeled as symmetry planes in pure material simulations, whereas the surfaces $y = 0$ and $y = L_y$ are periodic boundaries in the alloy simulations.

function of δ, which is varied from 128 to 4. For very small δ (≤ 8), steady growth conditions are reached relatively quickly for large undercooling. To save on computational cost in these runs (where $\Delta x_{min} = 0.5$), we sometimes use shorter lengths for L_x and L_y, chosen to ensure that the diffusion field does not interact with the ends (in the x and y directions) of the box. For smaller Δ however, it typically takes much longer to reach steady conditions, and when melt convection is included, it can take impractically long CPU times to get converged results. For these cases, we terminate our runs when the tip radius/velocity versus time curves start to even out. Fortunately, it turns out that the behavior we are interested in appears for combinations of δ and Δ where steady state conditions are always achieved.

In the alloy simulations, the initial condition is a planar interface at $x = X_0$, perturbed by randomly spaced finite amplitude fluctuations. The box in these simulations is taken to represent the shallow channel between microscope slides where directional solidification conditions are imposed, viz. a fixed thermal gradient moving at a constant speed V_p. Once again, in this arrangement we study the influence of the depth of the channel δ (or equivalently the sample film thickness), on interface morphology. To minimize the diffusion field's interaction with the lateral boundaries, L_x and L_y are chosen to be relatively large (~ 256). We enforce zero flux boundary conditions on the concentration field, on the surfaces $x = L_x/2 = -L_x/2$ and $z = 0 = \delta$, while periodic boundary conditions are imposed on the boundaries $y = 0$ and $y = L_y$. The rationale behind periodic boundary conditions is to be able to simulate an infinite domain in y.

Unless otherwise stated, on each boundary, we employ the same type of boundary condition on the phase-field variable ϕ, as we do on the transport variable. Where $\nabla\phi \cdot \mathbf{n} = 0$, the material "wets" the boundaries, and the corresponding contact angle is 90^o. Sémoroz *et al.* have previously used this technique to capture wetting of solid surfaces, with a two-dimensional phase-field model for binary alloys [70]. We also show a calculation with $\phi = -1$ on the boundaries, which is equivalent to making the material "non-wetting" (contact angle = 0^o). The real contact condition probably lies somewhere in between these two extremes.

2.3 Effect of small δ in a pure material

In this section, we report the effect of changing δ on the tip of a pure material dendrite, evolving along the negative x axis (upstream direction when flow is present). We simulated the cases shown in Table 2.1. We used a fixed value for the four-fold anisotropy in all our simulations ($\epsilon_4 = 0.05$). We have not corrected for grid anisotropy [14] in these calculations, but work at a grid spacing where its effect is known to be small [58].

Table 2.1: Pure material simulations.

Case	Δ	U_∞	δ
1(a)-(f)	0.55	0	128,64,32,16,8,4
2(a)-(f)	0.55	5	128,64,32,16,8,4
3(a)-(e)	0.25	0	128,64,32,16,8
4(a)-(f)	0.25	5	128,64,32,16,8,4
5(a)-(d)	0.15	0	128,64,32,16
6(a)-(e)	0.15	5	128,64,32,16,8

We use the following values for parameters in our calculations: thermal diffusivity $D = 4$, nominal interface width $W_0 = 1$, time scale for interface kinetics $\tau_0 = 1$, coupling parameter $\lambda = 6.383$, capillary length $d_0 = 0.1385$ (which leads to zero interface kinetics), kinematic viscosity $\nu = 92.4$, and Prandtl number $Pr = 23.1$.

2.3.1 "Wetting" boundary conditions, $\nabla\phi \cdot \mathbf{n} = 0$

To make ideas more concrete, we choose cases 3 and 4 as a representative subset of our computations and present detailed analyses on those runs. Figures 2.2 and 2.3 show the upstream dendrite's tip velocity and radius respectively, as functions of the box height δ.

In these plots, δ and ρ_{tip} were made dimensionless by scaling them with d_0, and V_{tip} is scaled by D/d_0. We compute the tip radii ρ_{xz} and ρ_{xy} along two principal planes using

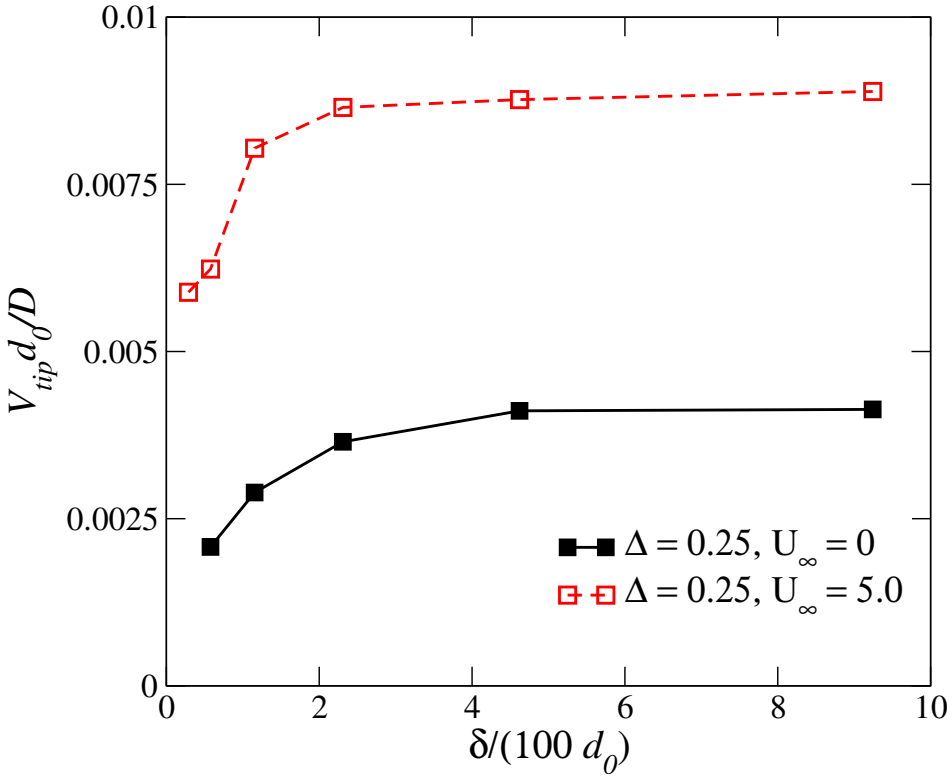

Figure 2.2: Tip velocity vs. δ, corresponding to cases 3 and 4 in Table 2.1.

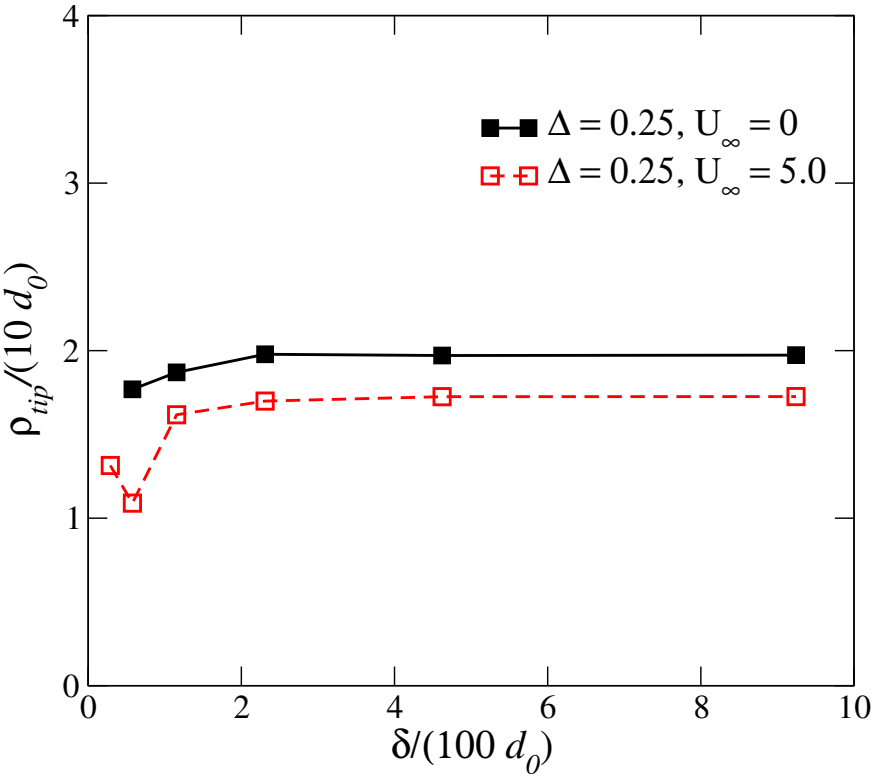

Figure 2.3: Tip radius vs. δ, corresponding to cases 3 and 4 in Table 2.1.

the method of Jeong *et al.* [19], and estimate the mean tip radius by the formula

$$\rho_{tip} = 2\left(\frac{1}{\rho_{xy}} + \frac{1}{\rho_{xz}}\right)^{-1}. \tag{2.2}$$

We can see from Fig. 2.2 that for large values of δ, the tip velocity remains relatively unaffected by the box height. However, as we go to very small heights V_{tip} decreases quite dramatically. As δ is decreased, there is also a gradual decrease in the tip radius ρ_{tip}. Clearly enough, box height has a pronounced effect on tip dynamics. Fluid flow induces a parallel shift in these curves. The dendrite tip velocity increases uniformly in the presence of flow [19]. On the other hand, the tip radius is lower than the case with pure diffusion.

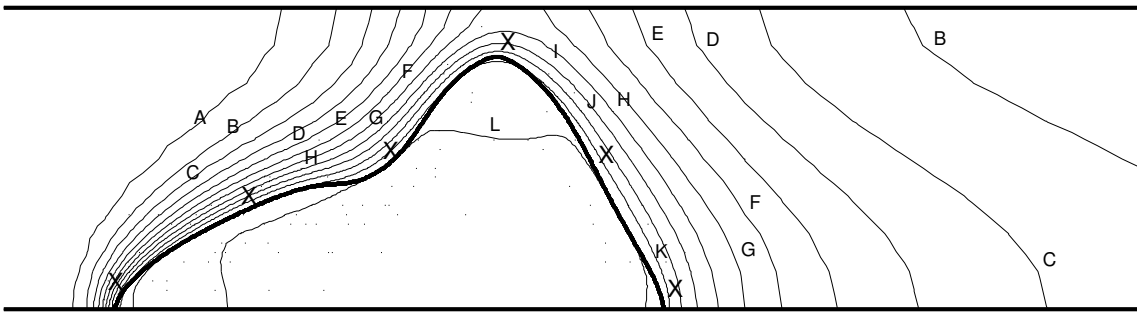

(a) $\delta = 64$ corresponding to Case 4(b). u ranges from A ≡ -0.24 to L ≡ 0.008

(b) $\delta = 8$, corresponding to Case 4(e). u ranges from A ≡ -0.24 to L ≡ 0.008

Figure 2.4: Temperature contours for two different box heights when $\Delta = 0.25$ and $U_\infty = 5.0$. In each case, the letter X symbolizes the dendrite outline (bold contour), under steady growth conditions. Notice that the contours near the dendrite tip are more spread out when δ is smaller.

The observed trends can be explained as follows. As long as δ is sufficiently large, the thermal field enveloping the dendrite will interact with the upper boundary at a distance that is relatively far behind the tip. In particular, the thickness of the thermal boundary layer near the tip remains unaffected by this interaction. However, as δ is decreased, this

thickness can grow quite rapidly. We illustrate this effect by examining the temperature profile in the x-z plane, as shown in Fig. 2.4. It is evident that the temperature contours are more spread out in Fig. 2.4(b) where $\delta = 8$, compared to those in 2.4(a), where $\delta = 64$. The increased boundary layer thickness, decreases the thermal gradient into the liquid at the liquid-solid interface, which in turn retards the growth rate as a direct consequence of the Stefan condition. Due to the zero flux boundary condition on the plane $z = \delta$, further reduction in δ makes heat transfer in the vertical direction almost completely ineffective. Tip curvature in the $x-z$ plane vanishes and the dendrite switches morphology from 3-D to 2-D. We note that once the dendrite goes 2-D, $\rho_{tip} = \rho_{xy}$.

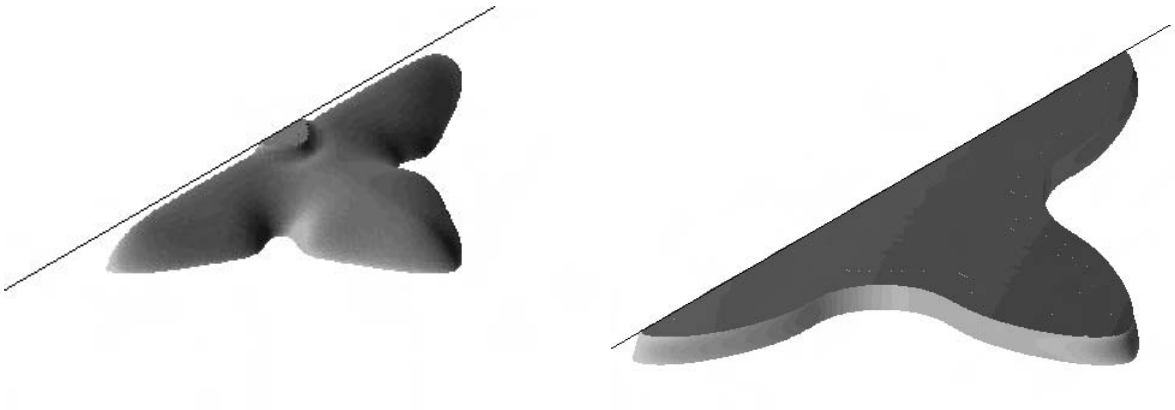

(a) $\delta = 16$, 3-D dendrite

(b) $\delta = 4$, 2-D dendrite

Figure 2.5: 3-D to 2-D dendritic transition at small δ. The shaded surface is the dendrite ($\phi = 0$). For these runs $\Delta = 0.55$ and $U_\infty = 0$.

An interesting result here is the 3-D to 2-D transition. We have performed tests with finer meshes (more elements in the vertical direction) to ensure that it is not simply an artifact of poor grid resolution. We believe this phenomenon to be a consequence of the $\nabla\phi \cdot \mathbf{n} = 0$ boundary condition on the upper boundary. The only way for the solid-liquid interface to match this boundary condition at small δ is for the curvature in the x-z plane to vanish. This is illustrated in Fig. 2.5.

It is also interesting to observe the effect that melt flow has on the interaction between the tip and the boundary. We find that melt convection reduces the value of δ where the tip velocity deviates from its nominal value. A straightforward explanation for this

effect is that advection increases the rate of heat transport from the upstream dendrite arm. This increases the growth rate (hence V_{tip}), while compressing the boundary layer, whose thickness scales as D/V_{tip}. Thus the dendrite remains three dimensional for a smaller value of δ than was previously possible, with convection absent. A more negative value of the undercooling also has qualitatively the same effect on the strength of the tip-boundary interaction, since V_{tip} again increases in this case. Fig. 2.6 summarizes these observations succinctly. Both melt convection and larger undercooling, cause points on respective curves whereupon interaction effects become important, to shift to the left.

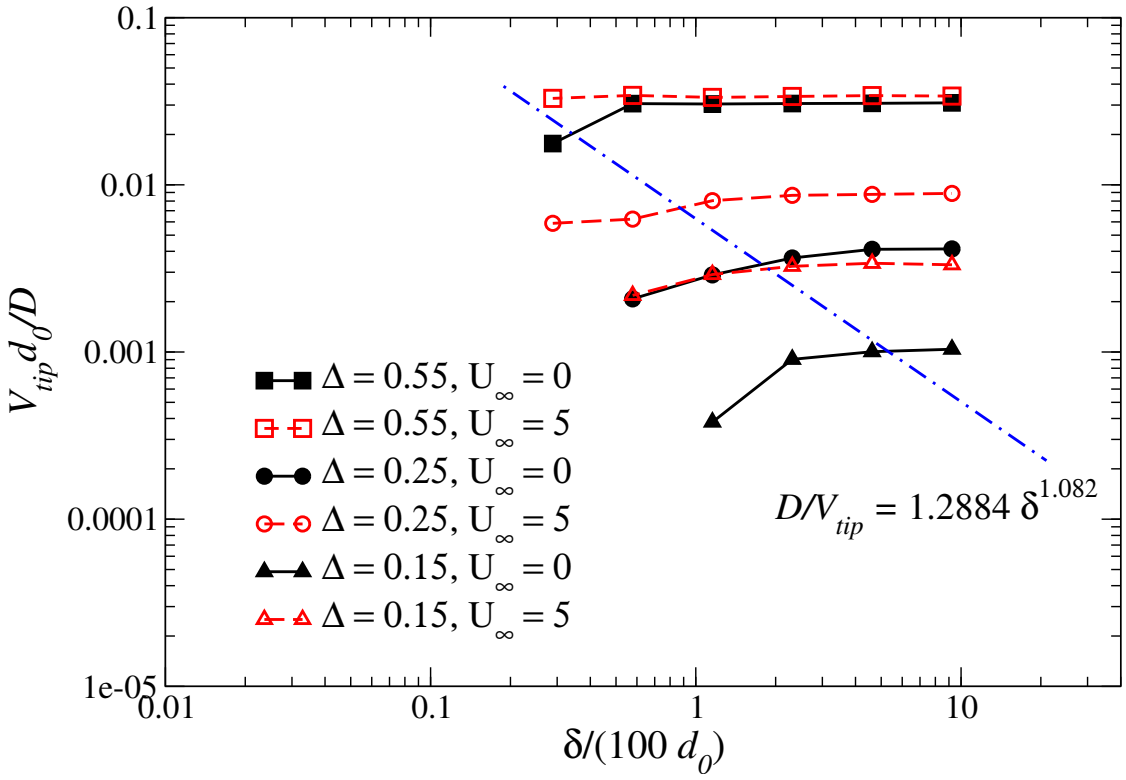

Figure 2.6: Tip velocity as a function of δ for different undercooling and flow conditions. A weak power law relationship emerges between the δ below which interaction effects are strong, and diffusion length D/V_{tip}.

Using a graph such as Fig. 2.6, one can derive a semi-quantitative estimate as to when the operating state becomes affected by the finite height of the container. If one assumes that the tip velocity at $\delta = 128$ for each case is approximately the tip velocity of a dendrite growing under identical conditions in an infinite domain, it is possible to

quantify the influence on the operating state in terms of a percentage deviation in the true tip velocity from this nominal value. If, for example, we consider deviations of the order of 3% to constitute a change in the operating state, a least squares fit to these cut-off points on the respective curves in Fig. 2.6 yields the criterion

$$\delta \geq 0.7912 \left(\frac{D}{V_{tip}}\right)^{0.9242}. \tag{2.3}$$

If this condition is not satisfied, then it is likely that the operating state is being influenced by the boundary. A simple condition such as the one in Eqn. (2.3) may be used as a rule of thumb in determining if experimental studies on free dendrite growth, in geometries similar to ours, are free from contamination. In fact, one may have intuitively guessed a condition of the type $\delta \geq \alpha\ (D/V_{tip})$ (where α is some constant) to apply based on physical arguments alone, and Eqn. (2.3) supports this conjecture.

2.3.2 Non-wetting boundary conditions

To underscore the importance of phase-field boundary conditions in selecting a particular growth state, we present results from another simulation with $\Delta = 0.55$, $U_\infty = 0$ and $\delta = 4$. This time we impose $\phi = -1$ on the upper boundary, which corresponds to a physical situation where the solidifying material is not allowed to wet the surface. A three dimensional surface plot of a steadily growing dendrite is shown for this case in Fig. 2.7.

As expected, the dendrite does not adhere to the top surface at all. We conclude that this will be the case for any δ if Dirichlet conditions of this nature are imposed. It is evident then, that the 3D-2D transition that we saw previously is a strong function of the boundary conditions imposed on the phase-field. It would be interesting to conduct a detailed investigation of the effect of different boundary conditions on the tip in 3-D. The interested reader is referred to the article by Sémoroz *et al.* [70], which discusses the influence of different contact angles on a dendrite's tip velocity, in two-dimensional thin film solidification.

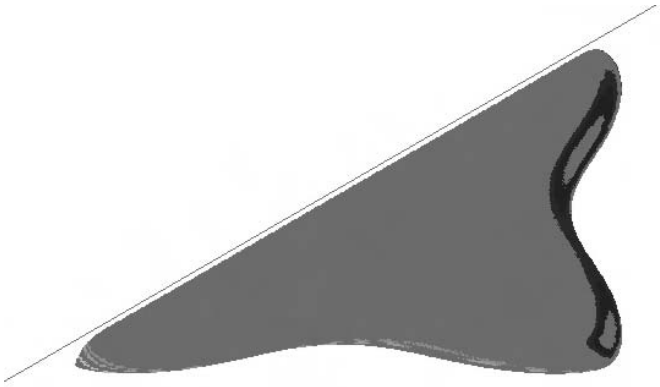

Figure 2.7: Three dimensional dendritic growth for $\Delta = 0.55$, $U_\infty = 0$ and $\delta = 4$, with $\phi = -1$ on the upper boundary. Note that the dendrite does not wet this surface.

2.4 Effect of small δ in a directionally solidified alloy

In this section, we describe results from our simulations on a directionally solidified alloy, and make comparisons with the experimental data of Liu *et al.* [66]. These simulations were conducted for the range of pulling speeds and channel depths shown in 2.2. The depth δ was varied from 64 to 4, and in each case, the simulation was continued until the interface became stationary in the moving frame. From the stable array of cells formed, a few were chosen as representative of the array, their tip radii were extracted in the two principal planes using a least squares quadratic polynomial fit, and the mean tip radius of each cell was computed using Eqn. (2.2). An average over these values was taken to be the mean tip radius of the interface. We note that this process required some approximation, especially in cases where we found steadily growing cells of disparate sizes that would have made such averaging inappropriate. In such cases, our usual approach was to choose cells farthest from the boundaries, and where even this failed to provide clear-cut choices, smaller cells were chosen because of their lesser likelihood to split. In a majority of our runs however, the choices were unambiguous. For certain values of δ we found interface evolution to occur in a way that cells would creep on either the top or bottom surfaces. In those cases, the phase-field boundary conditions on the respective

surfaces allowed us to treat them as symmetry planes for the purpose of calculating tip curvature.

Table 2.2: Alloy simulations.

Case	V_p	δ
1	0.8	64,32,16,8,4
2	1.0	64,32,16,8,4
3	1.5	64,32,16,8,4
4	2.0	64,32,16,8,4

2.4.1 Selection of simulation parameters

The following values for the lateral dimensions were seen to yield satisfactory results. $L_x = L_y = 256$ when $\delta \leq 16$, and $L_x = 256$, $L_y = 128$, otherwise. We chose our simulation parameters to keep computations tractable. It took about 90 hours of CPU time on a 3.1 GHz processor to simulate a typical directional solidification experiment for a chosen set of phase-field parameters on a mesh with about 170 000 elements ($\delta = 64$). The interface required about 250 dimensionless time units to reach steady state in this case. As noted earlier, the use of a moving reference frame allowed us to cut substantial costs associated with the need for larger domains to prevent the diffusion field from running out of the domain.

We did not attempt to model a real material in this study as this caused our simulations to become considerably more expensive. To illustrate this, consider a SCN-Salol system having the properties listed in Table 2.3. The conditions in a directional solidification experiment are completely described by the following two dimensionless control parameters, $M = d_0/l_T = 6.66\times10^{-5}$ and $S = V_p d_0/D = 2.04\times10^{-4}$, where d_0 is the capillary length, l_T is the thermal length and D is the solute diffusivity in the liquid phase; for a pulling velocity of $V_p = 5\mu$m/s. To get converged results with the phase-field model we require that the solution become independent of the parameter $\epsilon = W_0/d_0$. After

ensuring vanishing interface kinetics, the following relationships involving the phase-field parameters are realized: $D\tau_0/W_0^2 = a_1 a_2 \epsilon$, $V_p \tau_0/W_0 = S a_1 a_2 \epsilon^2$, and $l_T/W_0 = 1/(\epsilon M)$. Here, $a_1 = 0.8839$ and $a_2 = 0.6267$, are constants that arise in the phase-field formulation. [68]

Table 2.3: Physical properties of a SCN-Salol alloy system.

$\|m\|$ (Liquidus slope)	0.7 K/wt. %
D (Diffusion coefficient)	8×10^{-10} m^2/s
Γ (Gibbs-Thomson coefficient)	0.64×10^{-7} K m
k (Partition coefficient)	0.2
G (Thermal gradient)	4 K/mm
d_0 (Capillary length)	3.265×10^{-8} m
l_T (Thermal length)	4.9×10^{-4} m

Echebarria *et al.* [68] have shown that mesh converged results can be obtained with ϵ as large as 50. Setting $\epsilon = 50$, gives us an under-determined system of three equations with the five unknowns D, V_p, l_T, τ_0 and W_0. Making arbitrary choices for two of these parameters by setting $W_0 = \tau_0 = 1$, we obtain $D = 27.7$, $V_p = 0.2825$, and $l_T = 300$. A large value of l_T implies L_x needs to be very large at steady state, even in a moving reference frame, to contain the diffusion field. To avoid this, if we choose a more tractable value for l_T (say 100), and fix $\tau_0 = 1$, we now get $W_0 = 0.3333$, $D = 3.077$ and $V_p = 0.094$. Thus, the smallest element in our mesh needs to be at the very least $\Delta x = 0.3333$. Stability considerations now place a severe restriction on the size of the time step (Δt) needed for solving the phase-field equations by the Forward-Euler method, as $\Delta t \sim \Delta x^2$. Since it is clearly impossible to choose both l_T and W_0 independently, calculations involving real materials are typically more expensive.

We choose instead a more computationally favorable set of dimensionless parameters M and S for our study. To achieve our primary objective, which is to study the effect of δ on interface morphology, we anticipate, and in the following paragraphs demonstrate, that this hypothetical treatment will not obscure any physics. The parameters used in

our study are: $\tau_0 = W_0 = 1$, $D = 20$, $k = 0.8$, $\epsilon_4 = 0.05$, and $l_T = |m|(1-k)C_\infty/kG = 50$; where m is the liquidus slope, G is the imposed thermal gradient, and C_∞ is the far field solute concentration. The condition for negligible interface kinetics gives $d_0 = 0.0277$ and therefore $\epsilon = 36.1$, which should is sufficiently small to ensure convergence. The size of the smallest element in our adaptive mesh is $\Delta x = 1$, when $\delta \geq 8$, and $\Delta x = 0.5$, when $\delta = 4$, while $\Delta t = 0.005$ is the size of the time-step. For these parameter choices, the dimensionless control parameters work out to be $M = 5.54 \times 10^{-4}$ and $S \sim 1.385 \times 10^{-3}$.

2.4.2 Interface morphology and comparison with experiments

In order to test the model, we initially performed a set of runs to verify the Mullins and Sekerka stability limit of a planar interface [71], perturbed by small sinusoidal perturbations. We found that the model captures the stability spectrum correctly. Having convinced ourselves that this fundamental requirement was met, we proceeded with our study. Comparisons with the experimental data in this section offer a better validation of the model.

Fig. 2.8 shows the computed interface morphology at different values of δ. For small values of pulling speed ($V_p \leq 2$), the steady state consists of a stationary array of cells as in Fig. 2.8. However, unlike the cells observed in experiments, that are usually characterized by blunt tips, these appear to have sharper and better defined tips, giving the impression of dendrites. It is conceivable that ignoring thermal noise in our calculations is responsible for the absence of side-branches on these structures, that are typical of dendrites. At large values of δ, we find that the tip radii of these cells, measured on the two principal planes, are almost identical. However, as δ decreases, the in plane radii diverge from one another. In particular, the radius in the x-z plane becomes significantly smaller, and cross sections of the cells look elliptic. At $\delta = 4$, for small pulling speeds ($V_p \leq 1$), we get a two-dimensional interface (Fig. 2.8(c)). The inter-cellular spacing also increases as δ is decreased.

As pulling velocity is increased, the morphology becomes finer, with sharper and more tightly packed cells. This behavior is consistent with that seen of both cellular and

dendritic arrays in directional solidification experiments [65, 66, 72], where the primary spacing decreases with V_p.

For the set of phase-field parameters we have chosen, if $V_p \geq 2.5$, the interface does not reach steady state in a reasonable amount of CPU time, due to repeated tip-splitting of the cells. Splitting is initiated by oscillations that appear at the tip and propagate downward along the trunk of the cell. Cell spacing and shapes change very rapidly in this regime. We did not continue these runs any further to check if steady state is reached eventually. Instead, we set $V_p = 2.0$ as an upper bound on the pulling velocity, below which a stationary state was always the outcome. Fortunately, this still left us with sufficient sample space to conduct our study and make effective comparisons.

To enable plotting of our results on the same graph with the experimental data of Liu *et al.*, which corresponds to a SCN - 0.7 % wt. Salol system (properties in Table 2.3), we non-dimensionalized the axes as follows. The abscissa is the pulling speed (i.e. the tip velocity at steady state) V_{tip}, scaled by a characteristic velocity D/d_0k, while the ordinate is the tip radius ρ_{tip}, scaled by the diffusion length D/V_{tip}. One may appreciate the fact that the abscissa is in fact the dimensionless parameter that we had earlier denoted by S, multiplied by k. Fig. 2.9 shows a comparison of the data. The open symbols correspond to the experimental data of Liu *et al.*, while the solid symbols correspond to our calculations. A comparison between our data and theirs holds up surprisingly well. Of special significance are the following two observations: 1) Although we conducted our simulations at values of S and M that were each about an order of magnitude off theirs, the two sets of data correlate very well, i.e. appear to collapse on parallel curves that are not significantly different by way of intercept. This tells us that our choices of parameters for scaling the axes are appropriate. 2) Since their experimental data correspond to dendritic arrays, the cell-like structures we have computed are likely branchless dendrites.

In their experiments, Liu *et al.* note that tip radius data for dendritic arrays agree quite nicely with a relationship of the form $\rho_{tip}^2 V_{tip} = C$, where C is a constant dependent on d_0, k and D, as postulated by theoretical models of constrained growth [63, 64].

(a) $\delta = 64$, $V_p = 1.5$, three-dimensional cells

(b) $\delta = 16$, $V_p = 1.5$, three-dimensional cells

(c) $\delta = 4$, $V_p = 0.8$, two-dimensional cells

Figure 2.8: Interface morphology in a directionally solidified alloy. At steady state, stable arrays of three-dimensional cells appear. Note that at $\delta = 4$, the array comprises of two-dimensional cells.

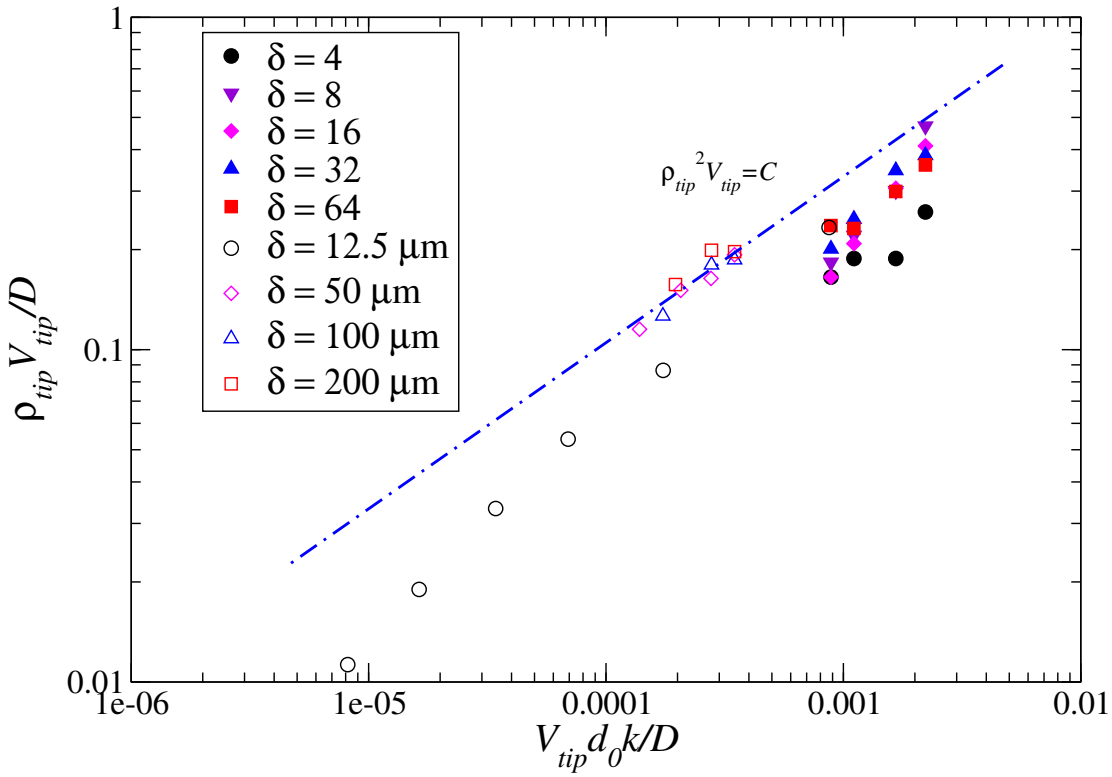

Figure 2.9: Comparison of binary alloy simulations with the phase-field model, and experimental data of Liu *et al.* [66]. Solid symbols correspond to the phase-field model and the open symbols are experimental data. The line denotes a relationship of the form $\rho_{tip}^2 V_{tip} = C$ between tip radius and velocity, where C can be expressed in terms of process parameters.

However, when δ is of the order of inter-dendritic spacing λ_1, this agreement deteriorates. This is evident in Fig. 2.9, where the $\rho_{tip}^2 V_{tip} = C$ line is shown as a guide to the eye. The open circles, which are data for $\delta = 12.5$ μm deviate in both slope and intercept from this line, which passes through the rest of their data, indicating a breakdown in the relationship. We observe similar trends in our data, viz., the line $\rho_{tip}^2 V_{tip} = C$ fits our data at $\delta = 32$ and 64 reasonably well, but as δ decreases from 16 to 4, this agreement deteriorates.

As in the numerical experiments with the pure material, we find that decreasing δ has a pronounced effect on interface morphology. Dendritic arrays seen in experiments have a certain structure/periodicity to them, that arises from underlying crystalline symmetries. For example, in our simulations we observe that the cells constitute a hexagonal array. When δ is large, away from the boundaries the diffusion field surrounding each cell tip obeys this symmetry, and the optimal λ_1 is selected. As δ decreases however, the diffusion field becomes increasingly asymmetric due to interaction with the boundaries at $x = 0$ and $x = \delta$. In particular, solute rejection decreases in the vertical plane x-z, while increasing in the horizontal plane x-y. Increased solute accumulation between cells in x-y, contributes to an increase in λ_1. However, since V_{tip} is fixed by the pulling speed, and a certain rate of solute rejection needs to be maintained, the tips tend to grow sharper as λ_1 increases. It is precisely this effect that causes the operating state to deviate from theoretical predictions.

To check for what value of δ our results deviate from theory, let us assume the steadily growing array at $\delta = 64$, $V_p = 1.5$ (Fig. 2.8(a)) to be one in which cells close to the plane $z = 32$ are "free" from boundary effects. We estimate the cell spacing in that plane to be $\lambda_1^f \approx 18$, where the superscript 'f' denotes "free". When $\delta = 16$ and $V_p = 1.5$ (Fig. 2.8(b)), we notice that our data points start departing from the theoretical prediction, viz. we see a relationship of the type $\rho_{tip}^a V_{tip} = C$, where $a > 2$. This suggests that agreement with theory deteriorates as $\delta \sim \lambda_1^f$, which is what Liu *et al.* concluded from their experiments. A more precise form of the above criterion can be obtained my making a careful study of λ_1 as a function of δ, for different V_p, and obtaining a criterion

based on a least squares fit to the deviation points (as we did with the pure material). Increasing pulling velocity suppresses tip-boundary interaction by reducing the thickness of the diffusion boundary layer D/V_{tip}, similar to the effect of melt convection in pure materials, and should induce a leftward shift in the curves.

2.5 Concluding remarks

We have investigated the role of confinement on solidification in both pure materials and binary alloys. Our simulations show that, for equi-axed growth in a pure material, the dendrite's operating state is affected when the container dimension δ, approaches the scale of the diffusion field D/V_{tip} near the tip. For directionally solidified binary alloys, confinement effects become important when δ is of the order of the primary dendrite spacing λ_1. Where applicable, one needs to consider the influence of these interactions when comparing experimental data with theoretical models that do not account for confinement effects.

It is notable that we were able to make meaningful comparisons with real experimental results using the phase-field model for the alloy. In particular, the agreement obtained in the trends shown by the dendrite tips for different δ and V_p is very encouraging, and is a testament to the power of phase-field modeling. Some ambiguity remains in classifying the computed microstructure as cells or dendrites. Since our results correlated well with dendrite data, we would like to think of them as dendrites. Perhaps, incorporating random fluctuations in the phase-field model will resolve this issue. We also found tip-splitting inducing oscillations above certain values of the pulling speed. We are unsure as to whether this instability has a physical meaning. In experiments, it is seen that increasing V_p causes a decrease in λ_1 and ρ_{tip} for a steadily growing interface, and our simulations capture this effect, viz. as V_p increases the cells split in a manner that produces a more stable configuration with a smaller λ_1 and ρ_{tip}. However, when $V_p \geq 2.5$, it appears that an optimal configuration is not possible in our system, given the constraints on its size and boundary conditions. We speculate that larger domains should

allow for more stable cell configurations at higher pulling speeds. This issue too needs further investigation.

We observed a change in dimensionality of the liquid-solid interface for certain values of δ and V_{tip}, when zero flux boundary conditions were imposed on the phase-field variable. There is some experimental evidence of this phenomenon in the literature. Liu and Kirkaldy [72] reported a 2-D to 3-D transition in their experiments on a SCN-Salol mixture. In their directional solidification experiments in a cell of fixed height ($\delta = 28\mu$m), they found this transition to occur at a driving velocity of 10.8 μm/sec. At a lower driving velocity of 7.6 μm/sec, the dendrites looked two dimensional. In our analysis of directional solidification, we found at $\delta = 4$, the cells underwent a 2-D to 3-D transition as the pulling velocity was changed from 1 to 1.5. The significance of this result is that through an appropriate selection of δ and V_p in experiments, it should be possible to obtain almost two dimensional dendritic arrays in materials that favor wetting. Such experiments will permit more favorable comparisons with 2-D dendrite growth theories, since finite boundary effects along the z axis cease to impact the growth.

Chapter 3

Modeling Polycrystals with Phase-Fields

3.1 Limitations of present day phase-field models

It is well established that phase-field modeling can be used to provide an accurate continuum description of processing phenomena involving multiple material phases, and along with adaptive mesh refinement, constitutes a key component of the materials modeling toolbox. The approach has been successfully extended beyond solidification to study a host of other phenomena, including crack propagation and fracture mechanics in single crystals [26, 73, 74], wave propagation in biological membranes [75], and single crystal dislocation dynamics [76, 77]. The reader is referred to the topical review by Chen [78] for a more comprehensive list of the applications of phase-field modeling.

There is a clear limitation, however. Realistic scenarios in metals processing—such as equi-axed dendrites with different orientations evolving and interacting with one another via their thermal and solute diffusion fields during a casting process, or a sheet of aluminum undergoing plastic deformation during hot rolling, typically involve polycrystalline systems, which are considerably more difficult to model. There are three principal concerns. (a) How does one handle multiple grain orientations? (b) What happens at

an inter-granular interface? (c) How can elastic and plastic effects be incorporated when modeling deformation processing?

Even in the relatively simple case of solidification, where elastic/plastic interactions are usually neglected, modeling of polycrystalline systems has met with limited success. The first serious attempt was made by Gandin and Rappaz [79], who developed a cellular automaton model for polycrystalline dendritic growth. In their method, the orientation and evolution of the shape of the growing grains was tracked numerically, allowing for a prediction of the final grain structure in the solid. However, the dendrite growth velocities were calculated based on some local average of the supercooling, without actually resolving the thermal/concentration field at the solid/liquid interface. Consequently, the cellular automaton model did not permit a detailed study of grain interactions.

Steinbach *et al.* [80] later proposed a model for multi-dendritic equiaxed growth based on the phase-field method, in which dendrites were approximated by envelopes evolved according to a Hamilton-Jacobi equation. The growth velocity of the envelope was computed by combining the analytical solution obtained by Cantor and Vogel [81] based on a stagnant thermal boundary layer approximation around paraboloid tips, and a selection criterion [64]. In this manner, they were able to model the evolution of up to 14 interacting dendrite grains in 3-D. This approach is far from general however, in that it depends on the availability of an analytical solution, and that its accuracy is sensitively bound to *ad hoc* model parameters, such as, the thickness of the thermal boundary layer. Further, it requires one to keep track of individual crystal orientations and coordinates, which to an extent limits the number of dendrites that can be simulated. In particular, neither of these approaches satisfactorily address issues (b) and (c).

Only recently have satisfactory phase-field models of polycrystalline solidification [16, 20, 21] emerged. In these models, for example the 2-D model proposed by Warren *et al.* [16], the free energy is a function of two spatially varying fields, one describing the state of crystalline order (the usual phase-field), and the other describing the orientation of a crystal with respect to a laboratory reference frame. Thus evolution equations for each of these fields can be obtained, by requiring that the free energy of the system

decrease in time. This model can correctly predict equi-axed dendritic growth, subsequent impingement and coalescence of dendrites, the formation of grain boundaries, and coarsening behavior. In fact, the results are very much reminiscent of microstructures observed in real materials. Notwithstanding some of the numerical subtleties in the implementation of this model, and complications in its extension to three dimensions, one can claim that this is by far the most complete model of solidification. Unfortunately, it still does not naturally incorporate elastic and plastic effects. For example, one cannot envision subjecting a polycrystalline system of grains evolved by this model to any kind of external loading, as there is no concept of *stiffness*.

Clearly, the answer is to inject elastic behavior into the phase-fields. Some groups have attempted to do this explicitly [22–26], by augmenting the free energy with a term for the elastic strain energy, and coupling displacement fields with phase-fields. While the latter models are more appealing for mesoscopic environments because of the uniformity of the phase-fields, and the explicit access provided to the stresses and strains, they lead to very complicated continuum models [24, 82]. Yet, a coupling between these kinds of models, and a model for polycrystalline materials, such as the one by Warren [16], could be the only answer if we insist on uniform phase-fields!

One realizes however, that if the goal is to develop a universal model that can capture everything from polycrystal evolution to dislocation dynamics, present day phase-field models are much too coarse-grained to be useful. The preservation of length scales and structures, even *smaller* than those captured by these models is essential! We will now present detailed description of a continuum model, recently proposed by Elder *et al.* [27, 28], which can describe elastic and plastic deformation of polycrystalline systems, as well as the formation of such systems by non-equilibrium processes such as solidification, using a single phase-field.

3.2 The phase-field crystal (PFC) model

The phase-field crystal (PFC) model [27,28] is founded on the critical observation that a free energy functional that is minimized by a periodic field natively includes elastic energy, anisotropy and symmetry properties of that field. We will provide adequate support for this claim in the following paragraphs. Thus the model incorporates all properties of a crystal that are determined by symmetry, for example, the relationship between elastic constants, location and number of dislocations, etc. Hence, it is quite different from other models based on uniform phase fields [22–26], where such periodic features need to be introduced explicitly. Further, unlike these other models, the PFC model yields (at least structurally) a relatively simple and well-behaved PDE for the evolution of the time-averaged[1] density of the system, giving it access to phenomena occurring on an atomic length scale, thereby enabling it to capture formation and interaction of a large number of topological defects, events which are typically obscured in classical continuum mechanics based models; but on diffusive time scales, an unimaginable situation even with state-of-the-art molecular dynamics simulations.

For pure materials, a simple free energy functional $\mathcal{G}\{\rho(\vec{X})\}$ that yields a triangular lattice in equilibrium, in two dimensions, is:

$$\mathcal{G}\{\rho(\vec{X})\} = \int_{\Omega} d\vec{X} \left[\left\{ \lambda \frac{\rho}{2} \left(q_o^2 + \nabla^2 \right)^2 \rho \right\} + \left\{ \alpha \Delta T \frac{\rho^2}{2} + u \frac{\rho^4}{4} \right\} \right], \tag{3.1}$$

where $\rho(\vec{X})$ is the time-averaged density of atoms, ΔT (< 0) denotes the temperature difference from some reference temperature (say the melting point), the subscript Ω denotes an area integral, and α, λ, q_o and u can be related to material properties [27,28]. The operator $\lambda\left(q_o^2 + \nabla^2\right)$ is obtained by fitting an algebraic equation to the first peak in the (inverse) structure factor $\mathcal{S}(q)^{-1}$ for liquid Argon. The free energy in Eq. (3.1) is the sum of a double-well potential term (in second curly brackets), which guarantees two

[1] By time-averaged, we mean an average of the field variable over a time scale that is much larger than the vibrational period of atoms, typically of the order of 10^{-15}s, but much smaller compared to the time scale for diffusive processes in the system, such as the viscous glide of dislocations, which occurs over a time scale of the order of 10^{-6}s.

phases (liquid and solid), and a gradient terms (in first curly brackets), which penalizes deviations from periodicity.

To demonstrate how elasticity is a natural consequence of a free energy of the form $\mathcal{G}$, let us suppose a 1-D case where $\rho(x) \approx A\sin(qx) + \rho_0$. Here A is the amplitude of the periodic density variations, $q = 2\pi/a$ is the wave-number, a is the wave-length, and ρ_0 is some constant. Substituting in Eq. (3.1) and integrating over one wave-length, we obtain the free energy density as

$$\begin{aligned}\mathcal{F}(A,q) = \frac{\mathcal{G}\{\rho(x)\}}{2\pi/q} &= \frac{3uA^4}{32} + \frac{1}{4}\rho_0^2\left(u\rho_0^2 + 2\alpha\Delta T + 2\lambda q_0^4\right) \\ &\quad + \frac{1}{4}A^2\left(3u\rho_0^2 + \alpha\Delta T + \lambda(q^2 - q_0^2)^2\right). \end{aligned} \tag{3.2}$$

The equilibrium values of A and q, which minimize the above free energy density are

$$\begin{aligned} q_{eq} &= q_0 \\ A_{eq} &= \pm 2\sqrt{-\rho_0^2 - \frac{\alpha\Delta T + \lambda\left(q^2 - q_0^2\right)^2}{3u}} \\ &= \pm 2\sqrt{-\rho_0^2 - \frac{\alpha\Delta T}{3u}}. \end{aligned} \tag{3.3}$$

Expanding Eq. (3.2) in a Taylor's series about A_{eq} and q_{eq} (q_0) we get

$$\begin{aligned}\mathcal{F}(A,q) &= \mathcal{F}(A_{eq},q_0) + \lambda(A_{eq}q_0)^2(q-q_0)^2 + \ldots \\ &= \mathcal{F}(A_{eq},q_0) + \lambda(A_{eq}q_0q)^2\left(\frac{a-a_0}{a_0}\right)^2 + \ldots \end{aligned} \tag{3.4}$$

which for small values of the strain, $\epsilon = (a - a_0)/a_0$, reduces to the energy density of a stretched spring

$$\Delta\mathcal{F} \approx \frac{1}{2}\mathcal{K}(\epsilon)\epsilon^2 + \mathcal{O}(\epsilon^3), \tag{3.5}$$

where the non-linear spring constant $\mathcal{K}(\epsilon) = 2\lambda\left(4\pi^2 A_{eq}/a_0^2(1+\epsilon)\right)^2$, also shows a temperature dependence via A_{eq}. Linearizing $\mathcal{K}$ about $\epsilon = 0$, we recover the linear elastic

stress response for small strains

$$\sigma = \frac{\partial \Delta \mathcal{F}}{\partial \epsilon} = \mathcal{K}_0 \epsilon, \tag{3.6}$$

where $\mathcal{K}_0 = 2\lambda \left(4\pi^2 A_{eq}/a_0^2\right)^2$. The same result can be demonstrated in 2-D for a triangular lattice that minimizes the free energy in Eq. (3.1). For details of this calculation, we refer the reader to the original paper by Elder and Grant [28], who have also worked out the elastic constants for this 2-D model in terms of material parameters.

Scaling the variables in Eq. (3.1) as $\vec{x} \equiv \vec{X} q_o$, $\psi \equiv \rho\sqrt{u/\lambda q_o^4}$, $r \equiv a\Delta T/\lambda q_o^4$, $t \equiv \Gamma \lambda q_o^6 \tau$ and $\mathcal{F} \equiv Fu/\lambda^2 q_o^6$, the dimensionless free energy becomes

$$\mathcal{F}\{\psi(\vec{x})\} \;=\; \int_\Omega \left[\frac{\psi}{2}\left\{r + (1+\nabla^2)^2\right\}\psi + \frac{\psi^4}{4}\right] dS. \tag{3.7}$$

Under the constraint of constant area, the dynamics of the density field (phase-field) ψ [83] are described by the following sixth order equation of motion, derived by observing continuity.

$$\frac{\partial \psi}{\partial t} \;=\; \nabla^2 \frac{\delta \mathcal{F}}{\delta \psi} \tag{3.8}$$

$$\Rightarrow \frac{\partial \psi}{\partial t} \;=\; \nabla^2 \left[\left\{r + (1+\nabla^2)^2\right\}\psi + \psi^3\right]. \tag{3.9}$$

Eq. (3.9) is the PFC equation. Additionally, if the effect of thermal fluctuations needs to be modeled, a conserved Langevin noise term ζ having a Gaussian distribution with zero mean and required by the fluctuation-dissipation theorem [84] to have a variance $\langle \zeta(\vec{r_1}, \tau_1)\zeta(\vec{r_2}, \tau_2)\rangle = -\mathcal{D}\vec{\nabla}^2 \delta\left(\vec{r_1} - \vec{r_2}\right)\delta\left(\tau_1 - \tau_2\right)$, with $\mathcal{D} = uk_BTq_0^{-2}/\lambda^2$, can be added to the right hand side of Eq. (3.9).

We will now show that the dynamics of Eq. (3.8) work to diminish $\mathcal{F}$ in time. Because the mass of the system needs to be conserved, we must have

$$\int_\Omega \psi \, dS = \text{constant}. \tag{3.10}$$

Differentiating both sides of the above equation with respect to time, we have

$$\int_{\Omega} \frac{\partial \psi}{\partial t}\, dS = 0. \tag{3.11}$$

Using Eq. (3.8) we then get,

$$\int_{\Omega} \nabla^2 \frac{\delta \mathcal{F}}{\delta \psi}\, dS = 0, \tag{3.12}$$

which upon applying the divergence theorem yields the following line integral,

$$\int_{\partial\Omega} \nabla \frac{\delta \mathcal{F}}{\delta \psi} \cdot \mathbf{n}\, dl = 0. \tag{3.13}$$

Eq. (3.13) needs to be satisfied by suitably constraining ψ along the boundary $\partial\Omega$, for example via the Neumann condition

$$\nabla \frac{\delta \mathcal{F}}{\delta \psi} \cdot \mathbf{n}\bigg|_{\partial\Omega} = 0. \tag{3.14}$$

Let us now differentiate both sides of Eq. (3.7) with respect to t. Then,

$$\begin{aligned} \frac{d\mathcal{F}}{dt} &= \int_{\Omega} \frac{\delta \mathcal{F}}{\delta \psi} \frac{\partial \psi}{\partial t}\, dS \\ \Rightarrow \frac{d\mathcal{F}}{dt} &= \int_{\Omega} \frac{\delta \mathcal{F}}{\delta \psi} \nabla^2 \frac{\delta \mathcal{F}}{\delta \psi}\, dS \end{aligned} \tag{3.15}$$

where we have again made use of Eq. (3.8). Integrating Eq. (3.15) by parts, we get

$$\frac{d\mathcal{F}}{dt} = \int_{\partial\Omega} \frac{\delta \mathcal{F}}{\delta \psi} \nabla \frac{\delta \mathcal{F}}{\delta \psi} \cdot \mathbf{n}\, dl - \int_{\Omega} \left| \nabla \frac{\delta \mathcal{F}}{\delta \psi} \right|^2 dS. \tag{3.16}$$

Using Eq. (3.14) we then have

$$\frac{d\mathcal{F}}{dt} = -\int_{\Omega} \left| \nabla \frac{\delta \mathcal{F}}{\delta \psi} \right|^2 dS < 0. \tag{3.17}$$

Therefore $\mathcal{F}$ must decrease in time, and Eq. (3.9) is purely dissipative.

An interesting feature of Eq. (3.9) is that it also permits constant solutions. In fact, in 2-D the free energy in Eq. (3.7) is minimized by three distinct solutions in a phase space which is parameterized by a mean field density $\bar{\psi}$, and the dimensionless undercooling r.
(a) A constant liquid phase

$$\psi_c = \bar{\psi}, \tag{3.18}$$

(b) a striped solid phase, approximated by

$$\psi_s = Ae^{i\mathbf{k}\cdot\mathbf{x}} + A^* e^{-i\mathbf{k}\cdot\mathbf{x}} + \bar{\psi}, \tag{3.19}$$

where A and A^* are the complex amplitude of the stripe and its conjugate respectively, $\mathbf{k} = k_1\vec{\mathrm{i}} + k_2\vec{\mathrm{j}}$ is a wave-vector with magnitude $k_0 = \sqrt{k_1^2 + k_2^2} = 1$, $\mathbf{x} = x\vec{\mathrm{i}} + y\vec{\mathrm{j}}$ is the position vector, and $\vec{\mathrm{i}}$, $\vec{\mathrm{j}}$ are unit vectors along the x and y axes, and
(c) a triangular solid phase, approximated by

$$\psi_t = \sum_{j=1}^{3} A_j e^{i\mathbf{k}_j\cdot\mathbf{x}} + \sum_{j=1}^{3} A_j^* e^{-i\mathbf{k}_j\cdot\mathbf{x}} + \bar{\psi}, \tag{3.20}$$

where

$$\begin{aligned} \mathbf{k}_1 &= k_0(-\vec{\mathrm{i}}\sqrt{3}/2 - \vec{\mathrm{j}}/2) \\ \mathbf{k}_2 &= k_0\vec{\mathrm{j}} \\ \mathbf{k}_3 &= k_0(\vec{\mathrm{i}}\sqrt{3}/2 - \vec{\mathrm{j}}/2) \end{aligned} \tag{3.21}$$

are the reciprocal lattice vectors, and $k_0 = 1$.

Based on these solutions, which assume only one dominant frequency mode (as opposed to a full Fourier series), and the corresponding value of the free energy, a phase diagram in $r - \bar{\psi}$ space can be approximated analytically, using the Maxwell construction theorem [28, 85] to identify regions with coexisting phases. This phase diagram is shown in Fig. 3.1. A part of it is also mapped to the equilibrium phase diagram of pure Argon (see inset), which shows that the model features can make contact with a real material.

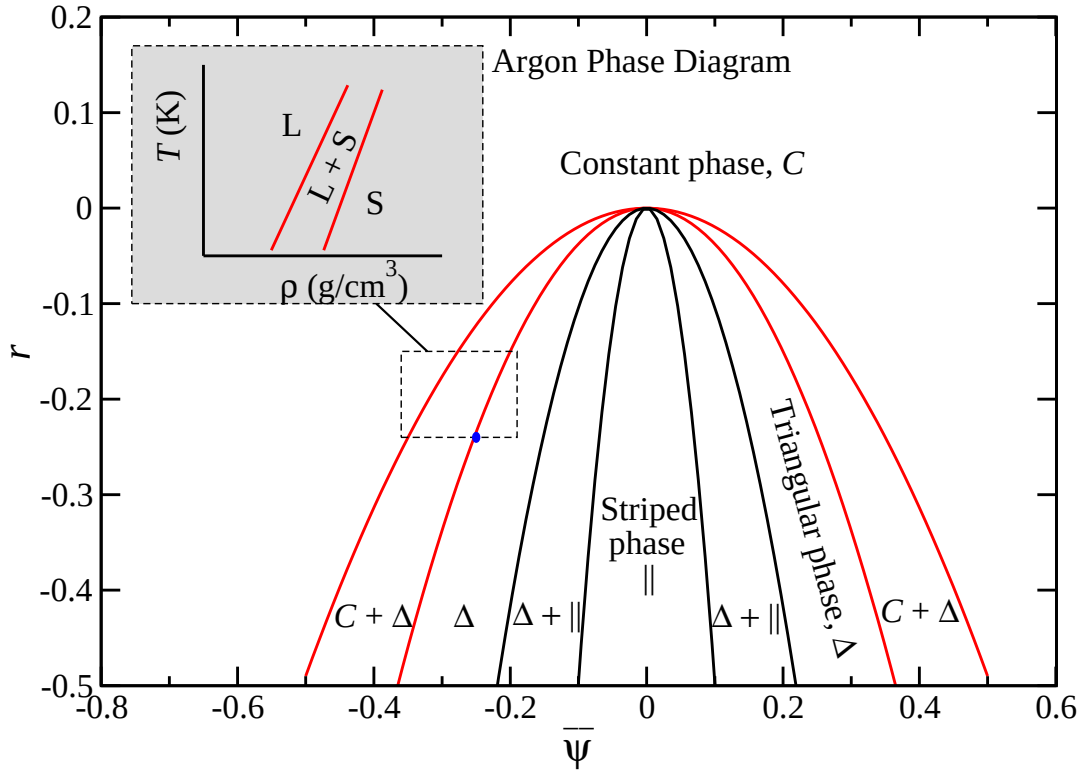

Figure 3.1: Phase diagram for the PFC model.

In this thesis, we will be primarily concerned with problems involving the emergence of the triangular phase from the constant phase.

Before concluding this section, it is appropriate to reiterate that Eq. (3.9) states that the density field ψ relaxes by diffusion alone, and while this is sufficient to study a variety of interesting phenomena such as solidification, grain growth, liquid phase epitaxial growth, and reconstructive phase transitions [28], and also viscous dynamics of dislocations under uniform stress distributions [86], it precludes the study of phase transformation phenomena in the presence of complex mechanical deformations, which require a suitable separation of time scales between phase transformation kinetics and the much more rapid (instantaneous) elastic relaxation. Stefanovic *et al.* [87] have recently proposed a modified phase-field crystal (MPFC) model that possesses such a separation of scales,

$$\frac{\partial^2 \psi}{\partial t^2} + \beta \frac{\partial \psi}{\partial t} = \gamma \nabla^2 \frac{\delta \mathcal{F}}{\delta \psi}, \tag{3.22}$$

where β and γ are phenomenological constants. The first term in this damped wave equation is responsible for the fast dynamics[2] that follow the application of a load, say, but which are still much slower than the time scale in molecular dynamics. Therefore the MPFC model is still sufficiently coarse-grained in time. At longer times from the point of load application however, Eq. (3.22) reduces to Eq. (3.9), and the dynamics are mainly diffusive.

All the methods and simulations presented in the subsequent chapters of this thesis are built only on the PFC model in Eq. (3.9), but can be readily extended to the MPFC model.

3.3 Applications and limitations

In this section we will present a gallery of results obtained from the PFC model, and also address its main limitation.

[2]This term captures sound wave propagation, i.e. phonon modes, essential for modeling brittle fracture in materials.

A variety of interesting materials processing phenomena can be simulated by evolving Eq. (3.9) for different values of the control parameters r and $\bar{\psi}$. For example, Fig. 3.2 shows heterogeneous nucleation, crystal growth, impingement, and the formation of grain boundaries, in a 2-D film evolved from three randomly nucleated seeds (finite amplitude random noise) with model parameters $r = -0.25$ and $\bar{\psi} = 0.285$. The centers of the black "dots" are the time averaged positions of atoms, and each "dot" can be loosely regarded as an atom[3]. The imperfections characterizing the grain boundaries are dislocations.

Fig. 3.3, taken from [28], shows grain growth in a 2-D polycrystalline film evolved over a very long time with model parameters identical to those in the previous simulation. The field plotted is the local free energy. The simulation starts with 50 initial seeds. Figs. 3.3b and 3.3c show a wide distribution of large and small angle grain boundaries, each with a different density of dislocations, appearing as black dots in the figure. Comparison of Fig. 3.3c with later configurations appears to suggest that small angle grain boundaries eventually disappear by dislocation annihilation and grain rotation.

Fig. 3.4, taken from [28], shows crack propagation by ductile fracture in a single crystal. The model parameters were, $r = -1$ and $\bar{\psi} = 0.49$. The initial condition was a defect-free crystal in equilibrium, with no strain in the x direction, but a 10% strain in the y direction. A small piece of material was cut out of this configuration and replaced with coexisting liquid, $\bar{\psi} = 0.79$. This region serves as the nucleus for a crack, which under the applied strain, propagates through the crystal.

Finally, Fig. 3.5, also taken from [28], shows liquid phase epitaxial growth. This is a technologically important process that is used to grow thin films on substrates. The lattice mismatch between the material of the film and the substrate on which it grows induces a stress, which the film relieves by emitting misfit dislocations at a certain height above the substrate. These dislocations then climb downwards to the film/substrate interface causing delamination. All these dynamics are nicely captured by the PFC model, and can be seen in Fig. 3.5. We will re-visit this problem in a later chapter.

[3]Because of the time-averaging, these dots are not instantaneous atomic positions. Instead, they represent an extremely high probability of finding an atom at that location.

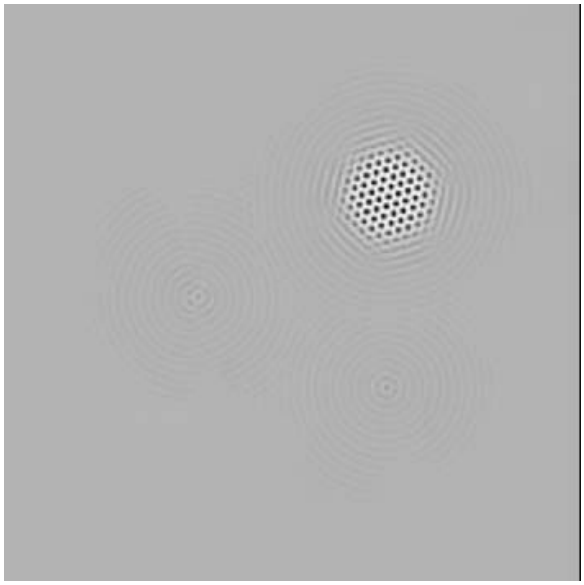

(a) $t = 300$

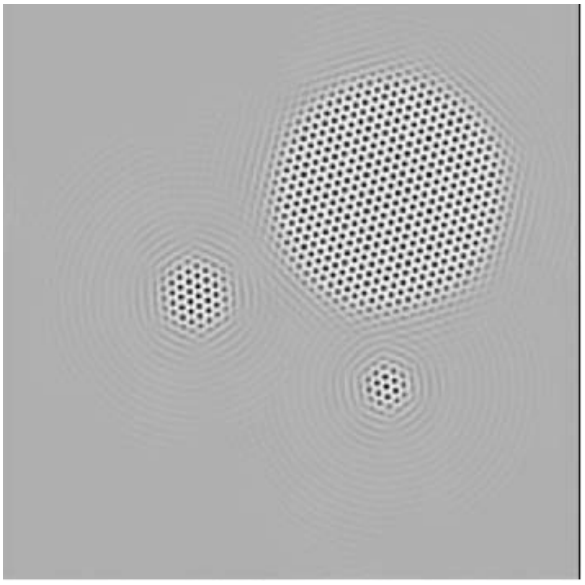

(b) $t = 450$

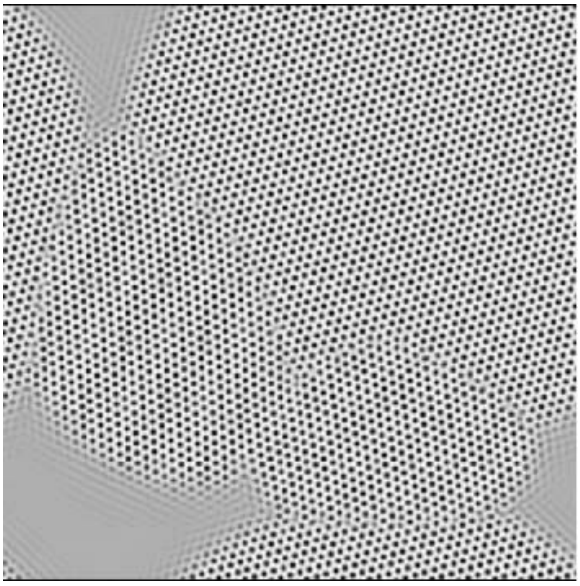

(c) $t = 750$

Figure 3.2: Heterogeneous nucleation, crystal growth, and formation of grain boundaries in a 2-D film from three randomly oriented seeds, as simulated by the PFC model. The field plotted is the density variable $\psi(\mathbf{x}, t)$, and t indicates the time into the simulation. Note that the pattern is periodic inside each grain, with each of the black dots representing an "atom".

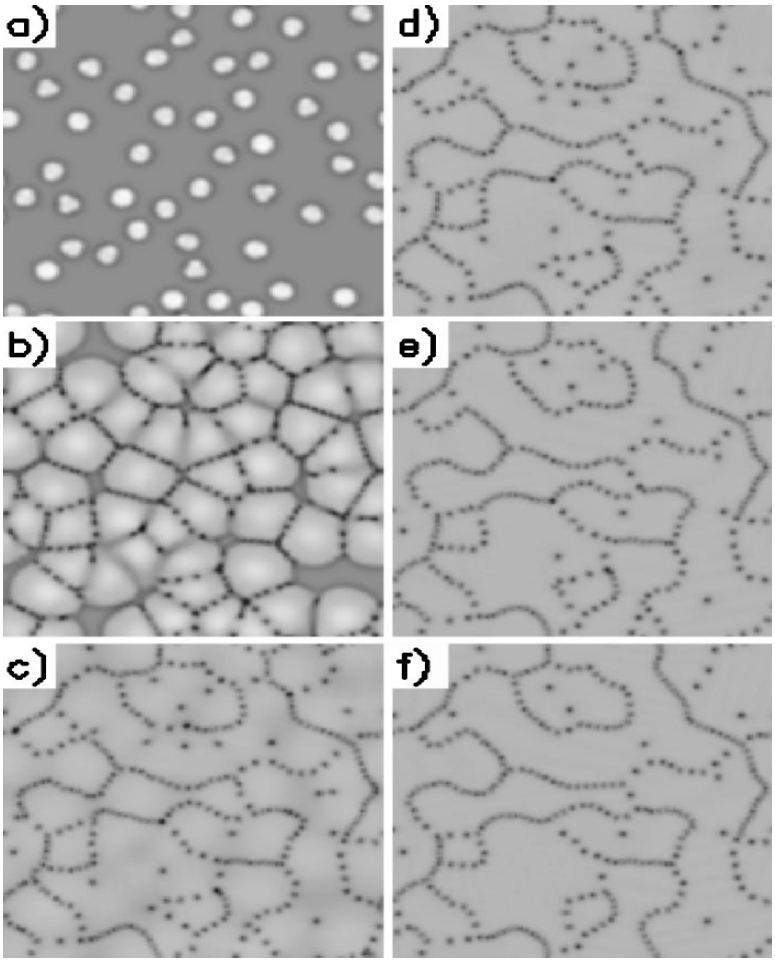

Figure 3.3: Grain growth with the PFC model [28]. The field plotted is the local free energy of the system. (a), (b), (c), (d), (e), and (f) correspond to times 50, 200, 1000, 3000, 15 000, and 50 000, respectively.

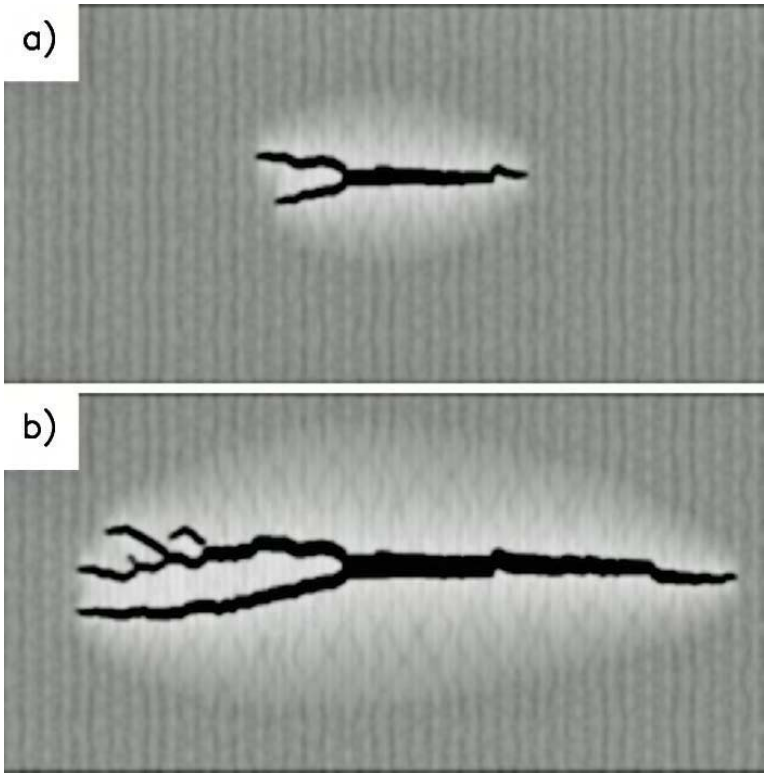

Figure 3.4: Ductile fracture with the PFC model [28]. The notch is a coexisting liquid phase in a perfect crystal which has reached equilibrium, while subjected to a uniaxial 10% strain in the y direction. The field plotted is the local free energy of the system.

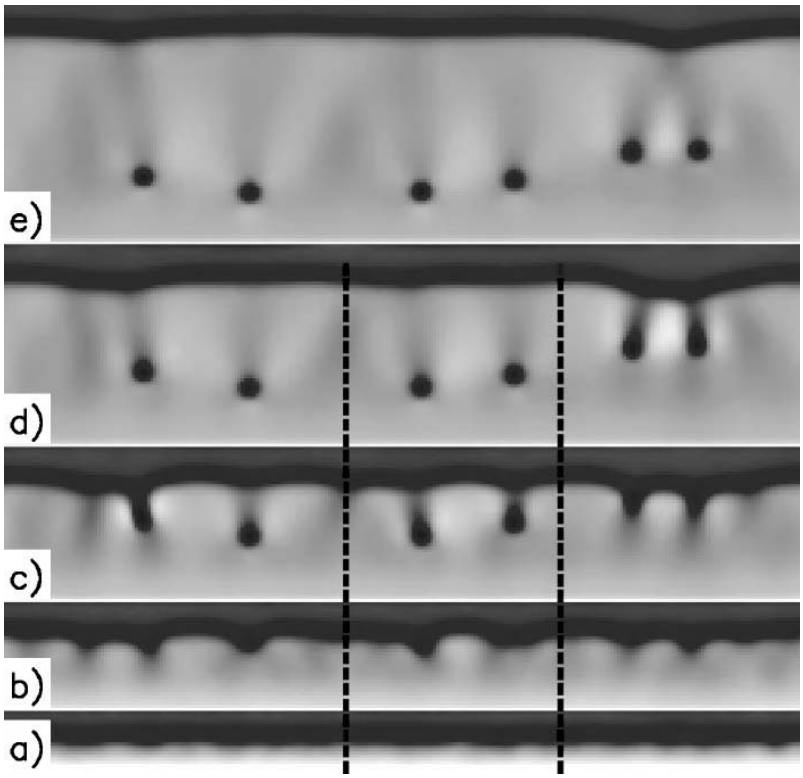

Figure 3.5: Epitaxial thin film growth with the PFC model [28]. The field plotted is the local free energy of the system. The black dots are misfit dislocations.

All these examples clearly illustrate the capabilities of the PFC model. However, there is one obvious limitation that prevents it from having true multiscale capability. The PFC equation is basically a nanoscopic order parameter equation (OPE) that describes phenomena at atomic length scales, and hence cannot be expected to adequately bridge the disparate nano- and micro- or meso- length scales, without parallel processing. For example, for the choice of simulation parameters that produced Fig. 3.2, the lattice spacing of the periodic triangular phase is $a_t \approx 7.3$. This implies that the grid spacing Δx required for numerical solution of Eq.(3.9) has to satisfy $\Delta x < a_t$. The particular choice of $\Delta x = a_t/8$ provides adequate resolution, ensuring a minimum of 9×9 grid points per "atom". In a physical system, the periodicity (interatomic distance) is of the order of angstroms. If one were to simulate a system a few 100 microns in size, such as the problem of interaction between a few equiaxed dendrites, it would require about a million degrees of freedom per dimension on a uniform computational mesh! Thus, despite being able to resolve phenomena over diffusive time scales the PFC model loses some of its effectiveness due to the super fine resolution that is required, making practical length scales in 2-D intractable without parallel computing. More importantly, even microscopic systems in 3-D are impossible to simulate. The stymying factor is that the periodic lattice precludes the use of effective adaptive mesh refinement algorithms, at least in real space. Some groups are presently investigating the possibility of implementing such algorithms in Fourier space, given the periodic nature of the solution.

In any case, there is the need for a computationally efficient formulation that will allow us to simulate larger systems, without compromising the fundamental properties that make the PFC model so powerful, viz. its ability to handle multiply oriented grains, its ability to predict correctly the formation and interaction of defects, and the elasticity that is naturally embedded in the model. We propose an idea for such a formulation in the following section.

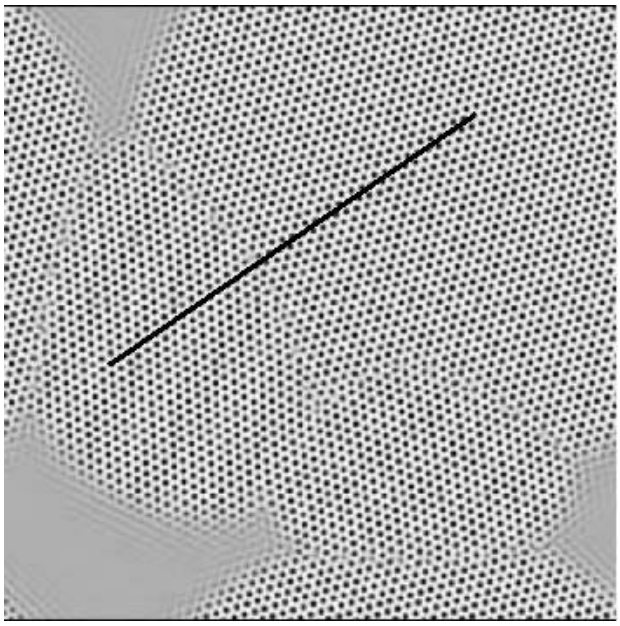

(a) ψ contours in a polycrystal

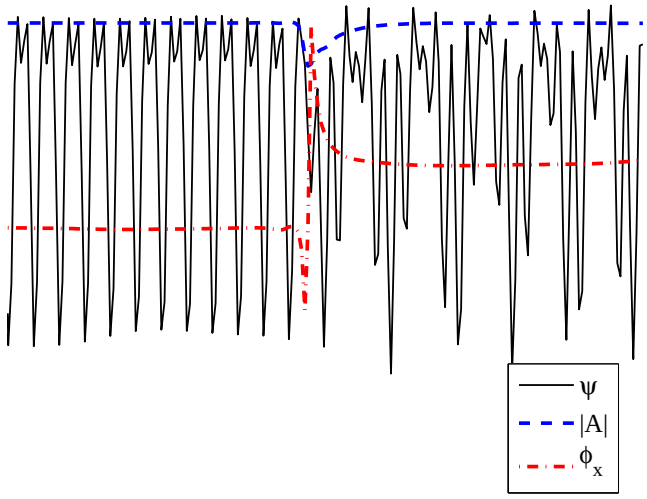

(b) Defect structure

Figure 3.6: The typical structure of ψ near a defect. (b) is representative of the 1-D variation in the fields along the black line in (a), which cuts across a grain boundary.

3.4 Spatial coarse-graining of the PFC model

The nature of the spatial patterns generated by the PFC equation suggests a natural approach towards developing a more computationally efficient formulation. Upon inspecting a typical polycrystalline system obtained from the PFC equation, such as Fig. 3.2, we immediately realize that the structure of the solution remains more or less periodic inside each grain, changing only in the vicinity of a solid/liquid interface, or a defect, or a grain boundary, which is essentially a collection of defects. Is there some way in which this feature of the solution can be exploited to save on computational cost?

Fig. 3.6(b) shows what the solution ψ typically looks like near a defect. Also plotted in the figure are, the amplitude modulus $|A|$, and the gradient of the phase of the pattern, ϕ_x. ψ is essentially a periodic function with a uniform amplitude, but different frequency or phase ϕ, inside each grain, as a result of the difference in grain orientations. The amplitude and phase (and phase gradient), while relatively uniform inside each grain, show steep gradients at the defect. This suggests that if the complex amplitude $A = |A|e^{i\phi}$ can be made the dynamic variable instead of ψ, adaptive mesh refinement should be possible, with the mesh in the interior of the grains, where $|A|$ and ϕ are slowly varying, comprising of coarse elements, but adequately refined near defects and grain boundaries.

Making A the dynamic variable entails two things. Since we only have an evolution equation for ψ, we must find a way to reliably derive an evolution equations for A. In order to do this however, we also need to define a suitable relationship between ψ and $|A|$, which on the one hand will allow us to derive these evolution equations, and on the other hand will permit us to reconstruct ψ from solutions for the amplitude. We will assume a simple one-mode Fourier series approximation for ψ, Eq. (3.20). The frequency mode we will choose ($k_0 = 1$) will be the fastest growing mode predicted by a linear stability analysis. Combining this approximation with a *renormalization group* analysis [32, 88], we will derive evolution equations for A. As we will show in subsequent chapters via quantitative comparisons, this approach works surprisingly well, and the amplitude equation we derive faithfully mimics the PFC equation while providing much

needed *coarse-graining* that improves computational efficiency even on uniform grids. Further, we will also show how amplitude/phase equations can be used to give the PFC model access to larger length scales, by effectively coupling them with an adaptive mesh refinement module.

3.5 An example: Coarse-graining the Swift-Hohenberg equation

Before moving on to the renormalization group analysis, we will provide some qualitative evidence to support our idea that amplitude equations when derived correctly, can indeed correctly reproduce the dynamics of the underlying OPE using the well studied example of the Swift-Hohenberg (S-H) equation [89]. The S-H model, which has been used in the past as a theoretical tool for studying periodic Rayleigh-Bénard convection patterns in 2-D systems (see Fig. 3.7) is given by:

$$\frac{\partial \chi}{\partial t} = \left[\epsilon - \left(1 + \nabla^2\right)^2\right] \chi - \chi^3, \tag{3.23}$$

where χ can be related to the depth averaged velocity field, and ϵ is the control parameter (reduced Rayleigh number) that produces bifurcation from the static conducting state for values greater than a critical value ${\epsilon_c}^4$. The big advantage of this model is that it has the same stability spectrum as the Bousinessq approximation to the Navier-Stokes equations that describes the natural convection problem, but is far easier to implement numerically, being a 2-D model of 3-D convection. Also note that if we replace ϵ by $-r$ in Eq. (3.23), and operate on the right hand side by $-\nabla^2$, we get the PFC equation. Thus the PFC equation is a conserved form of the S-H equation, a feature that produces interesting results when we attempt the renormalization group analysis in the next chapter.

[4]Note that for an infinite domain $\epsilon_c = 0$. For finite domains, the presence of domain walls exerts a damping influence on instabilities [90] which grow when $\epsilon \geq \epsilon_c > 0$.

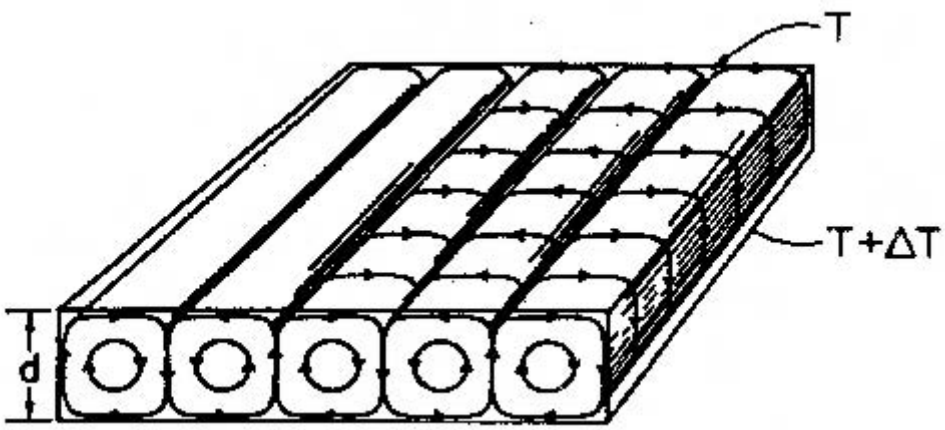

Figure 3.7: Schematic diagram of Rayleigh-Bénard convection rolls (stripes) between rectangular plates separated by a distance d, showing fluid streamlines in an ideal roll state (taken from [40]). The temperature gradient is $\Delta T/d$.

Gunaratne, Ouyang and Swinney [91] have derived a rotationally covariant amplitude equation from Eq. (3.23). They assumed the one-mode approximation

$$\begin{aligned} \chi(\mathbf{x},t) &= A(\mathbf{x},t)e^{i\mathbf{k}\cdot\mathbf{x}} + A(\mathbf{x},t)^* e^{-i\mathbf{k}\cdot\mathbf{x}} \\ &= 2\,|A(\mathbf{x},t)|\cos\left(\mathbf{k}\cdot\mathbf{x} + \phi(\mathbf{x},t)\right) \end{aligned} \tag{3.24}$$

and obtained the amplitude equation as

$$\frac{\partial A}{\partial t} = 4\left(\mathbf{k}\cdot\nabla - \frac{i}{2}\nabla^2\right)^2 A + (\epsilon - 3|A|^2)A, \tag{3.25}$$

where $\mathbf{k} = k_1\vec{\mathrm{i}} + k_2\vec{\mathrm{j}}$ is a wave-vector with magnitude $k_0 = \sqrt{k_1^2 + k_2^2} = 1$ (fastest growing wave-number), $\mathbf{x} = x\vec{\mathrm{i}} + y\vec{\mathrm{j}}$ is the position vector, and $\vec{\mathrm{i}}$, $\vec{\mathrm{j}}$ are unit vectors along the x and y axes. This equation is valid only for small values of ϵ, an assumption that features in its derivation from Eq. (3.23).

We discretize Eqs. (3.24) and (3.25) with a second order finite-difference scheme, and evolve them using a forward Euler time discretization from the same *random* initial

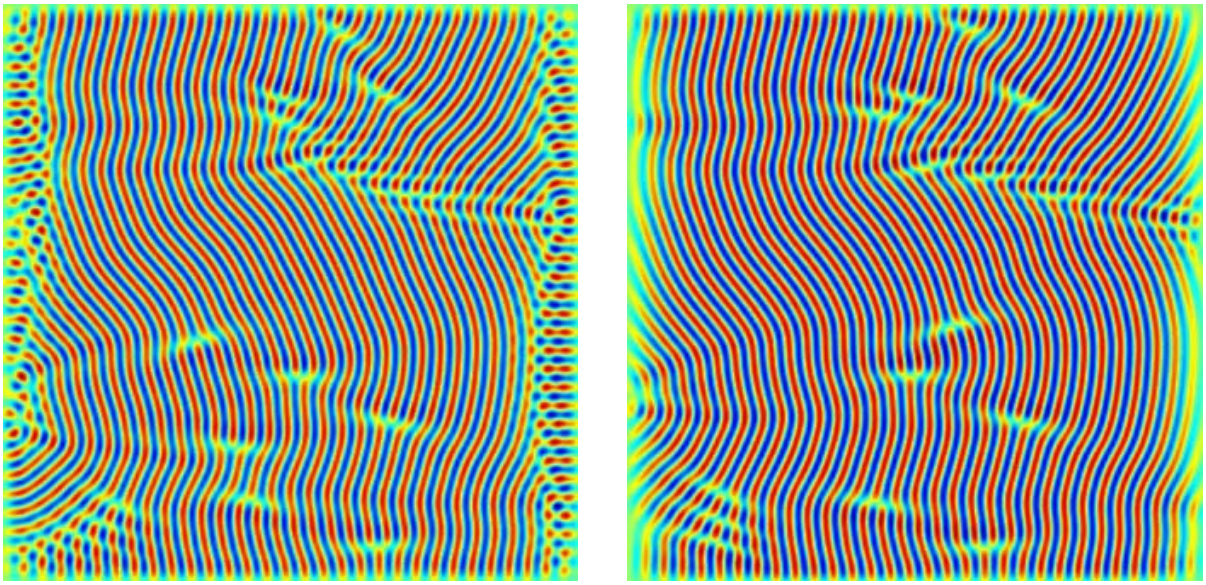

(a) χ, computed from Eq. (3.23).

(b) χ, reconstructed from Eq. (3.24) after solving Eq. (3.25).

Figure 3.8: Comparison of solutions obtained by solving the S-H equation (3.23) and the amplitude equation (3.25). The overall structure of the solution, including all bends and curves of the rolls, and defects, appear to be correctly captured by Eq. (3.25). The agreement deteriorates near the boundaries because of the presence of an additional length scale in the form of a boundary layer, over which rolls re-align.

condition. The boundary conditions on ϕ are,

$$\phi|_{\partial\Omega} = \partial_n \phi|_{\partial\Omega} = 0, \tag{3.26}$$

where ∂_n refers to the normal derivative, which, upon using Eq. (3.24) translate to the following equivalent boundary conditions on A,

$$A|_{\partial\Omega} = \partial_n A + iA|_{\partial\Omega} = \partial_n A|_{\partial\Omega} = 0. \tag{3.27}$$

Solving Eqs. (3.24) and (3.25), subject to Eqs. (3.26) and (3.27), yields long time solutions for χ, which are plotted in Fig. 3.8. Fig. 3.8(b) was generated by solving for the complex amplitude $A(\mathbf{x}, t)$ and recovering χ using Eq. (3.24).

The comparison holds up remarkably well in the bulk. Except for a few defects that are annihilated by the amplitude equation, the positions of all other defects are captured quite accurately, and the general structure and curvature of the rolls are faithfully reproduced. The amplitude solution does deteriorate somewhat near the boundaries. As postulated by Cross [92], and demonstrated through numerical simulations by Greenside and Coughran [90], in addition to the basic length scale $2\pi/k_0 = 2\pi$ of the pattern in the bulk, there is a second competing length scale of order $(\epsilon - \epsilon_c)^{-1/2}$, known as the healing length, over which the amplitude gradually decays to the boundary value. Over this boundary layer, straight rolls transition to align perpendicular to the walls by mediating defects. It is clear that a one-mode approximation cannot capture this behavior accurately[5].

[5]We have also implemented these equations with periodic boundary conditions on both χ and A where the respective solutions are practically indistinguishable from one another. However, periodic conditions in the S-H model lead to defect free systems of straight parallel rolls which do not make for very interesting comparisons. This is not the case in the PFC equation however, where periodic conditions do not have a dissipative effect on defects.

Chapter 4

Amplitude Equations and the Renormalization Group

In this chapter, we derive rotationally covariant amplitude equations from the two dimensional PFC model by a variety of renormalization group (RG) methods. We show that the presence of a conservation law introduces an ambiguity in operator ordering in the RG procedure, which we show how to resolve. We also compare our analysis with standard multiple scales techniques, where identical results can be obtained with greater labor, by going to sixth order in perturbation theory, and by assuming the correct scaling of space and time.

4.1 Amplitude equations in pattern formation

4.1.1 A brief history

It is now relatively standard in non-linear pattern formation problems to use amplitude equations to uncover universal features of periodic pattern forming systems. The formalism, first introduced by Newell, Whitehead, and Segel (NWS) [93,94] to describe periodic patterns in Rayleigh-Bénard convection, offers a way to extract the spatio-temporal envelope of these patterns, which then allows one to predict the dynamics qualitatively with very little information about microscopic details.

Unfortunately however, the NWS equation, as originally constructed, can only describe the dynamics of patterns oriented along the same fixed direction, everywhere in space, whereas physical systems often produce complex mosaics of patterns with no particular orientational preference. Such mosaics arise in real systems which are invariant under rotations, and hence any equation which is used to study them must also have the crucial property of rotational covariance, something that is lacking in the NWS equation. Equations with an orientational bias can be very difficult to implement numerically, especially on systems with arbitrarily oriented patterns. Nevertheless, the NWS equation embodies the important notion of coarse-graining, which has played a significant role in shaping the modern day theory of pattern formation [40], and also forms the basis of our approach to multiscale modeling with the PFC equation.

Gunaratne *et al.* [91] first derived a rotationally covariant form of the NWS equation using the method of multiple scales [95–98], where they assumed isotropic scaling of the spatial variables. They showed that the spatial operator in the NWS equation could be *symmetrized*, by systematically extending the calculation to higher orders in the perturbation parameter ϵ, the reduced Rayleigh number. They explained that the finite truncation of the perturbation series destroyed the rotational symmetry of the operator, which could however be recovered at a higher order. Another important conclusion of their work was that the qualitative behavior of pattern formation remained unchanged if one ignored higher order corrections, provided the equation itself was rotationally covariant. A drawback of their calculation, however, was (as with any application of the method of multiple scales), the need to guess *a priori*, the correct scaling of space-time variables. In addition, their calculation required gradual accumulation of operators and terms up to $\mathcal{O}(\epsilon^4)$, before a rotationally covariant equation emerged.

A more systematic approach emerged shortly after: Chen *et al.* showed how to perform reductive perturbation theory using RG methods [32], and obtained the NWS equation for the Swift-Hohenberg equation [89] by renormalizing the leading secular divergences at each order. Graham [33] subsequently showed that, in fact, this method gave the fully rotational covariant equations, if all secular terms are renormalized and

a careful choice of operator splitting is used. Calculations involving the RG typically produce elegant and accurate uniformly valid approximations for ordinary differential equations (ODEs), starting from simple perturbation series where no knowledge of the scaling present in the system is exercised [32]. For partial differential equations (PDEs), the same approach is successful, but generates a tedious number of perturbation terms at higher orders. This difficulty arises from the need to explicitly construct secular solutions of the highest possible order, at every order in ϵ, and from a practical standpoint equals (if not outweighs) the advantage of requiring no prior insight into the problem. For this reason, calculations employing this method for PDEs have rarely gone beyond $\mathcal{O}(\epsilon)$. The key advantage of the RG method, however, is that when carefully performed, the calculation yields a rotationally covariant amplitude equation at a much lower order in ϵ compared to the method of multiple scales, as was shown by Graham [33].

Nozaki *et al.* [34, 88], have developed a more abstract version of the perturbative RG for weakly non-linear PDEs, called the "proto-RG" scheme. They argue that if one is willing to sacrifice some of the purely mechanical aspects of the conventional RG by taking cognizance of the system's properties, such as those exhibited by the governing differential equation, one can obtain a rotationally covariant amplitude equation to $\mathcal{O}(\epsilon)$ without having to construct any secular solutions. By computing minimal particular solutions, usually obtained by a straight-forward inspection, one can even obtain $\mathcal{O}(\epsilon^2)$ corrections with only a little more algebra. They illustrated the relative simplicity of this method by deriving the rotationally covariant form of the NWS equation to $\mathcal{O}(\epsilon^2)$, as previously derived by Gunaratne *et al.* [91]. Shiwa [36] further demonstrated the efficacy of this scheme by obtaining the well-known Cross-Newell phase equation [37, 38], which describes phase dynamics of patterns generated by the Swift-Hohenberg equation. A drawback of this approach is in the selection of the so called "proto-RG" operator, which turns out to be non-unique in general. Nozaki *et al.* show, however, that the operator *is* uniquely specified, provided we insist on the lowest order differential operator possible.

4.1.2 Our findings

As the reader will have no doubt realized from this synopsis, several methods and variants exist for deriving envelope equations from order parameter equations (OPEs) that produce predominantly periodic patterns. Although one may argue that some of these methods are essentially variants of perturbative RG theory for PDEs, they are structurally very different. It is thus a very instructive exercise to compare the defining properties of each of these methods in the context of a single microscopic OPE, such as the PFC equation, and to this we devote the rest of this chapter.

A rather surprising finding of our work was that when we followed naively the "cookbook recipe" for each method, our results were not identical, with the RG methods yielding a form of the amplitude equation, slightly different from that derived by the classical method of multiple scales. The PFC equation obeys a local conservation law, and while this by itself can lead to a variety of interesting features [99, 100], it also brings to the fore an ambiguity with the usual implementation of the renormalization procedure, something that is not unique to conservation laws. This ambiguity is essentially an operator ordering one, and can be remedied in a straightforward way. Once done, all methods yield the same amplitude equation, even though the technical details are quite distinct in the different methods. As a pedagogical exercise, we present the analysis for the Van der Pol oscillator in the Appendix, once again obtaining consistent results from all methods when using the approach described herein. Our main conclusion is that the renormalization group method is still considerably easier to implement than competing approaches, and in particular requires no knowledge of the scaling relationship between space and time while achieving full rotational covariance at lowest order in perturbation theory.

The chapter is organized as follows. In section 4.2.1 we present a detailed derivation of an amplitude equation from the PFC model using a heuristic approach. In section 4.2.2, we use the proto-RG method to derive the amplitude equation more systematically. We attempt to verify these calculations independently in section 4.2.3 using the method of multiple scales. A 1-D derivation via the conventional RG method is presented for

completeness in section 4.2.4. We find that while the proto-RG and RG results are consistent, they do not agree with the other calculations, due to an operator ordering ambiguity not previously noticed. We remedy this in section 4.3, and conclude the chapter with some remarks in section 4.4.

4.2 Amplitude equations from the PFC equation

4.2.1 Heuristic RG calculation

We now present a derivation of the amplitude equation from Eq. (3.9) using linear stability analysis and a shortcut motivated by experience. An idea along these lines was previously implemented by Bestehorn and Haken [101] to derive an OPE (similar to the Swift-Hohenberg equation) for modeling traveling waves and pulses in two-dimensional systems, but not for deriving amplitude equations.

4.2.1.1 Verification with the S-H model

As a test of our method, we first derive the rotationally co-variant form of the Newell-Whitehead-Segel (NWS) equation [91] (Eq. (3.25)) starting with S-H equation (Eq. (3.23)). We first conduct a linear stability analysis by considering a perturbation $\widetilde{\chi}$ about the static conducting state $\chi_0 = 0$. Linearizing Eq. (3.23) about χ_0 we obtain

$$\frac{\partial \widetilde{\chi}}{\partial t} = \left[\epsilon - \left(1 + \nabla^2\right)^2\right] \widetilde{\chi}. \tag{4.1}$$

Substituting harmonics of the type $\widetilde{\chi} = A(t)e^{i\mathbf{k}\cdot\mathbf{x}}$ in Eq. (4.1); where $A(t) = A^0 e^{\omega t}$, A^0 is some constant, $\mathbf{k} = k_1\vec{i} + k_2\vec{j}$, and ω is the constant determining growth (or decay) rate of the perturbation, we get the discrete dispersion relation

$$\omega = \epsilon - \left(1 - |\mathbf{k}|^2\right)^2. \tag{4.2}$$

The fastest growing mode has the locus $|\mathbf{k}| = 1$.

If we want to study the effect of applying small spatial modulations to the amplitude about this mode, i.e. $A(t) \longmapsto A(x,y,t) = A^0 e^{\omega(\mathbf{Q})t + i\mathbf{Q}\cdot\mathbf{x}}$, where $\mathbf{Q} = Q_1\ \vec{i} + Q_2\ \vec{j}$ is the perturbation vector, Eq. (4.2) gets modified to

$$\omega(\mathbf{Q}) = \epsilon - \left(1 - |\mathbf{Q} + \mathbf{k}|^2\right)^2. \tag{4.3}$$

Replacing Fourier space variables by their real space equivalents we get

$$|\mathbf{Q} + \mathbf{k}|^2 \equiv -\nabla^2 - 2i\mathbf{k}\cdot\nabla + 1. \tag{4.4}$$

From Eqns. (4.3) and (4.4) we conclude that space-time amplitude variations are governed by

$$\frac{\partial A}{\partial t} = \left[\epsilon - \left(\nabla^2 + 2i\mathbf{k}\cdot\nabla\right)^2\right] A = \left[\epsilon + 4\left(\mathbf{k}\cdot\nabla - \frac{i}{2}\nabla^2\right)^2\right] A. \tag{4.5}$$

The non-linear terms are obtained perturbatively as follows, by treating ϵ as a small parameter. Scaling χ in Eq. (3.23) by $\sqrt{\epsilon}$, and calling the new variable $\hat{\chi}$ we get the S-H equation in the form

$$\frac{\partial \hat{\chi}}{\partial t} = -\left(1 + \nabla^2\right)^2 \hat{\chi} - \epsilon\left(\hat{\chi} - \hat{\chi}^3\right). \tag{4.6}$$

Now putting $\hat{\chi} = \hat{\chi}_0 + \epsilon\hat{\chi}_1 + \epsilon^2\hat{\chi}_2 + \mathcal{O}(\epsilon^3)$ in Eq. (4.6), where $\hat{\chi}_0$ is given by Eq. (3.24) which has also been scaled by $\sqrt{\epsilon}$, we obtain the equation for $\hat{\chi}_1$, by matching like powers of ϵ, as

$$\frac{\partial \hat{\chi}_1}{\partial t} = -\left(1 + \nabla^2\right)^2 \hat{\chi}_1 + \hat{A}(1 - 3|\hat{A}|^2)e^{i\mathbf{k}\cdot\mathbf{x}} - \hat{A}^3 e^{3i\mathbf{k}\cdot\mathbf{x}} + \text{c.c.} \tag{4.7}$$

Here c.c. denotes the complex conjugate. The term $\hat{A}(1-3|\hat{A}|^2)$ is responsible for secular divergences in space and time, and therefore needs to be renormalized. It is also hence, the non-linear component at $\mathcal{O}(\epsilon)$ in the amplitude equation (alternatively recovered by considering the normal form equations [102], as shown by Gunaratne, Ouyang and Swinney [91]). Scaling back to original variables (χ, A) and combining the non-linear term with Eq. (4.5), the well known, rotationally co-variant form of the NWS equation

[33–36, 91]

$$\frac{\partial A}{\partial t} = 4\left(\mathbf{k}\cdot\nabla - \frac{i}{2}\nabla^2\right)^2 A + (\epsilon - 3|A|^2)A \tag{4.8}$$

is obtained to $\mathcal{O}(\epsilon)$, which is identical to Eq. (3.25).

4.2.1.2 Derivation from the PFC equation

Moving over to the PFC equation, we now pose Eq. (3.9) in a more convenient form by scaling ψ by $\sqrt{\epsilon}$, and calling this new variable ψ. To remain consistent with the previous derivation we have replaced r by $-\epsilon$. In this manner, Eq. (3.9) becomes

$$\partial_t\psi = \nabla^2(1+\nabla^2)^2\psi + \epsilon\nabla^2(\psi^3 - \psi). \tag{4.9}$$

Let us now consider the stability of the uniform phase solution $\bar{\psi}$ to the formation of the hexagonal pattern by adding to it a small perturbation $\widetilde{\psi}$, so that $\psi = \bar{\psi}+\widetilde{\psi}$. Substituting in Eq. (4.9) and linearizing about $\bar{\psi}$ we obtain

$$\partial_t\widetilde{\psi} = \nabla^2\left[\epsilon(3\bar{\psi}^2 - 1) + (1+\nabla^2)^2\right]\widetilde{\psi} \tag{4.10}$$

If $\widetilde{\psi}$ is a hexagonal instability in the form given by the spatially dependent part of Eq. (3.20), then using $A_j(t) = A_{0j}\exp(\omega_j t)$, where A_{0j} are complex constants, and substituting in Eq. (4.10), we obtain the discrete dispersion relation

$$\omega_j = -|\mathbf{k}_j|^2\left[\epsilon(3\bar{\psi}^2 - 1) + \left(1 - |\mathbf{k}_j|^2\right)^2\right], \tag{4.11}$$

after applying orthogonality conditions. Here ω_j predicts the growth or decay rate of a hexagonal instability in the spatially uniform system. Note that for real values of $\bar{\psi}$, ω_j is always real. Thus, a necessary condition for the instability to grow, i. e. for ω_j to take on positive values, is $3\bar{\psi}^2 - 1 < 0$, or equivalently $3\bar{\psi}^2 - \epsilon < 0$ in original variables. The most dangerous wave-number is the locus $|\mathbf{k}_j| = k_0 = 1$.

We now consider spatial modulations in the amplitude about this preferred wavenumber, i. e.

$$A_j(t) \longmapsto A_{Rj}(\mathbf{x},t) = A_{0j} e^{\omega_j(\mathbf{Q})t} e^{i\mathbf{Q}\cdot\mathbf{x}}, \tag{4.12}$$

where $\mathbf{Q} = Q_x\,\vec{\mathrm{i}} + Q_y\,\vec{\mathrm{j}}$ is a perturbation vector, and A_{Rj} is the renormalized amplitude, whose implication will be clarified in a following paragraph. Consistent with Eq. (4.11), we can now write the exponent controlling growth rate along each lattice vector as

$$\omega_j(\mathbf{Q}) = |\mathbf{Q}+\mathbf{k}_j|^2 \left[\epsilon(1-3\bar{\psi}^2) - \left(1-|\mathbf{Q}+\mathbf{k}_j|^2\right)^2\right]. \tag{4.13}$$

We now replace the Fourier space variables in the above equation by their real space counterparts so that,

$$\omega_j \equiv \partial_t \;\;,\;\; Q_x \equiv -i\partial_x \;\;,\;\; Q_y \equiv -i\partial_y \;\;, \tag{4.14}$$

thus obtaining,

$$|\mathbf{Q}+\mathbf{k}_j|^2 \equiv 1 - \nabla^2 - 2i\mathbf{k}_j\cdot\nabla = 1 - \mathcal{L}_{\mathbf{k}_j}. \tag{4.15}$$

Combining Eqs. (4.13) and (4.15), the space-time amplitude variations along each lattice vector is given by the sixth order linear partial differential equation

$$\partial_t A_{Rj} + (1-\mathcal{L}_{\mathbf{k}_j})\mathcal{L}_{\mathbf{k}_j}^2 A_{Rj} + \epsilon(1-3\bar{\psi}^2)\mathcal{L}_{\mathbf{k}_j} A_{Rj} = \epsilon(1-3\bar{\psi}^2)A_{Rj}. \tag{4.16}$$

We also need nonlinear terms, which play a vital role in pattern dynamics near onset of the instability, to complement the above set of equations. There are a couple of different ways to obtain these terms. One can directly look for the nonlinear part in the normal form equations [103] for the dynamics of A_j in a hexagonal basis [91, 104, 105]. These equations have been widely used to study the dynamics and stability of *exactly* periodic rolls and hexagonal patterns originating from the static conducting state in Rayleigh-Bénard convection. Alternatively, one can derive these terms to a particular order in ϵ through a renormalization group (or multiple scales) analysis of the governing

differential equation, as was done previously for the S-H equation. Here, we choose the latter approach once again, starting from Eq. (4.9), but only going far enough in the RG analysis to identify the correct form of the terms.

We start with a perturbation series in ϵ

$$\psi = \psi_0 + \epsilon\psi_1 + \epsilon^2\psi_2 + \epsilon^3\psi_3 + \dots \tag{4.17}$$

where ψ_0 is a steady state solution and $\psi_{j(\neq 0)}$ are the higher order corrections. As we are interested in amplitude variations in the hexagonal pattern, we pick ψ_0 to be the steady *hexagonal* solution, i. e. Eq. (3.20). Substituting in Eq. (4.9), we obtain the following equation at $\mathcal{O}(\epsilon)$:

$$\left[\partial_t - \nabla^2(1+\nabla^2)^2\right]\psi_1 = \left(\partial_t - \mathcal{L}_{\mathcal{P}}\right)\psi_1 = \nabla^2(\psi_0^3 - \psi_0), \tag{4.18}$$

where

$$\begin{aligned}
\nabla^2(\psi_0^3 - \psi_0) \;=\; & (1 - 3\bar{\psi}^2)\sum_{j=1}^{3} A_j e^{i\mathbf{k}_j\cdot\mathbf{x}} \\
& -3A_1\left(|A_1|^2 + 2|A_2|^2 + 2|A_3|^2\right)e^{i\mathbf{k}_1\cdot\mathbf{x}} - 6A_2^*A_3^*\bar{\psi}e^{i\mathbf{k}_1\cdot\mathbf{x}} \\
& -3A_2\left(2|A_1|^2 + |A_2|^2 + 2|A_3|^2\right)e^{i\mathbf{k}_2\cdot\mathbf{x}} - 6A_1^*A_3^*\bar{\psi}e^{i\mathbf{k}_2\cdot\mathbf{x}} \\
& -3A_3\left(2|A_1|^2 + 2|A_2|^2 + |A_3|^2\right)e^{i\mathbf{k}_3\cdot\mathbf{x}} - 6A_1^*A_2^*\bar{\psi}e^{i\mathbf{k}_3\cdot\mathbf{x}} \\
& +\text{other terms} + \text{c.c.}
\end{aligned} \tag{4.19}$$

The superscript '*' denotes complex conjugation. To this order, the "other terms" are functions of complex exponentials that do not lie in the null space of the linear differential operator in Eq. (4.18), i. e. they are non-resonant terms. Therefore, they do not contribute to unbounded growth in ψ_1. The terms listed in Eq. (4.19) are, however, resonant with the operator, and their coefficients need to be renormalized in order to bound the solution obtained by truncating the perturbation series at $\mathcal{O}(\epsilon)$. The renormalization procedure allows the amplitude A_j, previously constant, to now have space-time

variations that absorb secular divergences. We assert that the nonlinear terms in the amplitude equation to $\mathcal{O}(\epsilon)$ must be the *renormalized* coefficients of the exponential terms in resonance with the differential operator. For example, the terms complementing the space-time operator along basis vector $\mathbf{k}_1$ must be

$$\epsilon(1-3\bar{\psi}^2)A_{R1} - 3\epsilon A_{R1}\left(|A_{R1}|^2 + 2|A_{R2}|^2 + 2|A_{R3}|^2\right) - 6\epsilon A^*_{R2}A^*_{R3}\bar{\psi}, \tag{4.20}$$

where the A_{Rj} are the renormalized amplitude functions (no longer constants). Note that these terms are completely identical to those predicted by normal form theory for a hexagonal basis [91, 105]. Combining Eqs. (4.16) and (4.20) we write the amplitude equation as

$$\begin{aligned}\partial_t A_1 &= -(1-\mathcal{L}_{\mathbf{k}_1})\mathcal{L}^2_{\mathbf{k}_1}A_1 - \epsilon(1-3\bar{\psi}^2)\mathcal{L}_{\mathbf{k}_1}A_1 + \epsilon(1-3\bar{\psi}^2)A_1 \\ &\quad -3\epsilon A_1(|A_1|^2 + 2|A_2|^2 + 2|A_3|^2) - 6\epsilon A^*_2A^*_3\bar{\psi},\end{aligned} \tag{4.21}$$

for lattice vector $\mathbf{k}_1$, and permutations thereof for $\mathbf{k}_2$ and $\mathbf{k}_3$, where we have replaced the variables A_{Rj} by A_j.

We observe that the leading term in Eq. (4.20) is consistent with the right hand side of Eq. (4.16), thereby providing a natural overlapping link about which to match the linear stability and perturbation results. In a more abstract sense, we draw a parallel between this method and the technique of matched asymptotic expansions in singular perturbation theory, where inner and outer asymptotic solutions are matched over a common region of validity in the solution space, to obtain a globally valid solution. This completes our derivation of the amplitude equation via a heuristic or "quick and dirty" approach. For future reference, we will call Eq. (4.21), the QDRG (quick and dirty RG) equation, and the method used to obtain it as the QDRG (or heuristic) method.

To summarize the procedure, we first conducted a linear stability analysis of the scaled PFC equation about the uniform state to obtain a linear differential operator controlling the space-time evolution of the complex amplitude A_j of the hexagonal pattern. We superimposed on this dispersion relation periodic modulations of the amplitude, and

from the dispersion relation in terms of these latter modulations, identified the gradient terms in the amplitude equation. We then carried out the first step in a conventional RG analysis to obtain the form of the nonlinear terms that should accompany this differential operator, and combining the two results, we wrote down the amplitude equation for the hexagonal pattern. In this respect, our approach lacks the full mathematical rigor of a conventional RG reduction or a multiple scales derivation, which gives it a somewhat "dirty" appearance. However, we made no assumptions about the scaling of the space-time variables in the system, nor did we have to construct any secular solutions so far. We will comment on extending this method systematically to higher orders in ϵ in the following section.

4.2.2 Proto-Renormalization group derivation

With the proto-RG method, our starting point is Eq. (4.9) with the perturbation series Eq. (4.17). Thus, to $\mathcal{O}(\epsilon)$ we obtain Eq. (4.18), whereas to $\mathcal{O}(\epsilon^2)$ we get

$$(\partial_t - \mathcal{L}_\mathcal{P})\,\psi_2 = \nabla^2(3\psi_0^2\psi_1 - \psi_1). \tag{4.22}$$

The structure of Eq. (4.18) allows us to infer that its simplest particular solution will take the form

$$\begin{aligned}\psi_1 \;=\; & \sum_{j=1}^{3} P_{1j}(\mathbf{x},t)e^{i\mathbf{k}_j\cdot\mathbf{x}} + \sum_{j=1}^{3} Q_{1j}e^{2i\mathbf{k}_j\cdot\mathbf{x}} + \sum_{j=1}^{3} R_{1j}e^{3i\mathbf{k}_j\cdot\mathbf{x}} + \sum_{j=1}^{3} S_{1j}e^{i\mathbf{s}_j\cdot\mathbf{x}} \\ & + \sum_{j=1}^{2} T_{1j}e^{i\mathbf{t}_j\cdot\mathbf{x}} + \sum_{j=1}^{2} U_{1j}e^{i\mathbf{u}_j\cdot\mathbf{x}} + \sum_{j=1}^{2} V_{1j}e^{i\mathbf{v}_j\cdot\mathbf{x}} + \text{c. c.},\end{aligned} \tag{4.23}$$

where

$$\mathbf{s}_1 = -\vec{\mathrm{i}}\,\frac{\sqrt{3}}{2} - \vec{\mathrm{j}}\,\frac{3}{2}, \mathbf{s}_2 = \vec{\mathrm{i}}\,\frac{\sqrt{3}}{2} - \vec{\mathrm{j}}\,\frac{3}{2}, \mathbf{s}_3 = \mathbf{s}_2 - \mathbf{s}_1$$

$$\mathbf{t}_1 = -\vec{\mathrm{i}}\,\frac{3\sqrt{3}}{2} - \vec{\mathrm{j}}\,\frac{1}{2}, \mathbf{t}_2 = \vec{\mathrm{i}}\,\frac{3\sqrt{3}}{2} - \vec{\mathrm{j}}\,\frac{1}{2}$$

$$\mathbf{u}_1 = -\vec{\mathrm{i}}\,\frac{\sqrt{3}}{2} - \vec{\mathrm{j}}\,\frac{5}{2}, \mathbf{u}_2 = \vec{\mathrm{i}}\,\frac{\sqrt{3}}{2} - \vec{\mathrm{j}}\,\frac{5}{2}$$

$$\mathbf{v}_1 = -\vec{\mathrm{i}}\,\sqrt{3} - \vec{\mathrm{j}}\,2, \mathbf{v}_2 = \vec{\mathrm{i}}\,\sqrt{3} - \vec{\mathrm{j}}\,2, \tag{4.24}$$

are non-resonant modes generated by the cubic term. Note that we have explicitly denoted the space-time dependence of the secular coefficients $P_{1j}(\mathbf{x}, t)$, which are polynomials in x, y and t, whereas by inspection, the other coefficients Q_{1j}, R_{1j}, S_{1j}, T_{1j}, U_{1j} and V_{1j} *can* be complex constants. Specifically, P_{11} satisfies

$$\left(\partial_t - \mathcal{L}_{\mathcal{P}}\right) P_{11} e^{i\mathbf{k}_1\cdot\mathbf{x}} = (1-3\bar{\psi}^2)A_1 e^{i\mathbf{k}_1\cdot\mathbf{x}} - 3A_1\left(|A_1|^2 + 2|A_2|^2 + 2|A_3|^2\right) e^{i\mathbf{k}_1\cdot\mathbf{x}} - 6A_2^* A_3^* \bar{\psi} e^{i\mathbf{k}_1\cdot\mathbf{x}} \tag{4.25}$$

$$\begin{aligned} \Rightarrow \left(\partial_t + (1-\mathcal{L}_{\mathbf{k}_1})\mathcal{L}_{\mathbf{k}_1}^2\right) P_{11} &= (1-3\bar{\psi}^2)A_1 - 3A_1\left(|A_1|^2 + 2|A_2|^2 + 2|A_3|^2\right) - 6A_2^* A_3^* \bar{\psi} \\ &\equiv L_{\mathbf{k}_1} P_{11}, \end{aligned} \tag{4.26}$$

where $L_{\mathbf{k}_j}$ is the "proto-RG" operator for lattice vector $\mathbf{k}_j$. From the above equation it is quite obvious that P_{11} cannot be constant for any non-trivial solutions, and likewise for P_{12} and P_{13}.

As P_{1j} are secular, we now renormalize [32] ψ about arbitrary regularization points $\mathbf{X}$ and T, as in the conventional RG method, to get

$$\psi = \bar{\psi} + \sum_{j=1}^{3} A_{Rj}(\mathbf{X}, T) e^{i\mathbf{k}_j\cdot\mathbf{x}} + \epsilon \sum_{j=1}^{3} \left(P_{1j}(\mathbf{x}, t) - P_{1j}(\mathbf{X}, T)\right) e^{i\mathbf{k}_j\cdot\mathbf{x}} + \ldots + \text{c.c.} \tag{4.27}$$

where A_{Rj} is now the renormalized amplitude that absorbs secular divergences. Since ψ must be independent of these regularization points, we have

$$\begin{aligned} L_{\mathbf{k}_1}^{\mathbf{X},T}\psi &= 0 \\ \Rightarrow L_{\mathbf{k}_1}^{\mathbf{X},T} A_{R1}(\mathbf{X}, T) &= \epsilon L_{\mathbf{k}_1}^{\mathbf{X},T} P_{11}(\mathbf{X}, T) + \epsilon^2 L_{\mathbf{k}_1}^{\mathbf{X},T} P_{21}(\mathbf{X}, T) + \epsilon^3 L_{\mathbf{k}_1}^{\mathbf{X},T} P_{31}(\mathbf{X}, T) \\ &\quad + \ldots \end{aligned} \tag{4.28}$$

after applying orthogonality conditions. This is the general form of the proto-RG equation for weakly nonlinear oscillators [88]. $L_{\mathbf{k}_1}^{\mathbf{X},T}$ is the proto-RG operator $L_{\mathbf{k}_1}$ in Eq. (4.26),

with variables $\mathbf{x}$ and t replaced by $\mathbf{X}$ and T respectively. Changing back from $(\mathbf{X}, T) \to (\mathbf{x}, t)$ and $A_{Rj} \to A_j$, and using Eqs. (4.26) and (4.28), we can write the amplitude equation along lattice vector $\mathbf{k}_1$ to $\mathcal{O}(\epsilon)$ explicitly as

$$\partial_t A_1 = -(1-\mathcal{L}_{\mathbf{k}_1})\mathcal{L}_{\mathbf{k}_1}^2 A_1 + \epsilon(1-3\bar{\psi}^2)A_1 - 3\epsilon A_1(|A_1|^2+2|A_2|^2+2|A_3|^2) - 6\epsilon A_2^* A_3^* \bar{\psi}, \quad (4.29)$$

with appropriate permutations for A_2 and A_3. Note that in using Eq. (4.26), we have replaced A_j by their renormalized counterparts A_{Rj} as is consistent with the proto-RG procedure, before reverting to the former notation for amplitude. Upon comparing the two amplitude equations obtained so far, Eqs. (4.21) and (4.29), we note that the QDRG derived equation carries the extra term $\epsilon(1-3\bar{\psi}^2)\mathcal{L}_{\mathbf{k}_1} A_1$. Evidently, the QDRG and the proto-RG methods produce different amplitude equations when applied to the PFC equation, the extent of this difference controlled by the parameter $\epsilon(1-3\bar{\psi}^2)$. It is interesting to note that for the Swift-Hohenberg equation, both the QDRG method and the proto-RG method yield identical amplitude equations. The extra term in the QDRG equation for the PFC model is clearly a consequence of the conservation law, with its attendant extra Laplacian.

As mentioned earlier, the principal advantage of using the proto-RG method is the relative ease with which one can progress to higher order calculations. Let us now extend this calculation to $\mathcal{O}(\epsilon^2)$. We need ψ_1 in order to evaluate the right hand side of Eq. (4.22), which means that we additionally need to evaluate Q_{1j}, R_{1j}, S_{1j}, T_{1j}, U_{1j} and V_{1j}. The constant values of these terms can be determined by inspection. For example, by analogy with P_{11}, we see that Q_{11} must satisfy

$$\begin{aligned} (\partial_t - \mathcal{L}_{\mathcal{P}})\, Q_{11} e^{2i\mathbf{k}_1\cdot\mathbf{x}} &= -12\left(A_1^2\bar{\psi} + 2A_1 A_2^* A_3^*\right) e^{2i\mathbf{k}_1\cdot\mathbf{x}} \\ \Rightarrow \left(\partial_t + (4-\mathcal{L}_{2\mathbf{k}_1})(\mathcal{L}_{2\mathbf{k}_1}-3)^2\right) Q_{11} &= -12\left(A_1^2\bar{\psi} + 2A_1 A_2^* A_3^*\right). \end{aligned} \quad (4.30)$$

Unlike Eq. (4.26) however, we see that Eq. (4.30) permits a constant solution for Q_{11}, which in turn is determined to be

$$Q_{11} = -\frac{1}{3}\left(A_1^2\bar{\psi} + 2A_1A_2^*A_3^*\right). \tag{4.31}$$

Similarly, constant solutions for the other coefficients are

$$\begin{aligned} Q_{12} &= -\frac{1}{3}\left(A_2^2\bar{\psi} + 2A_1^*A_2A_3^*\right) \\ Q_{13} &= -\frac{1}{3}\left(A_3^2\bar{\psi} + 2A_1^*A_2^*A_3\right) \end{aligned}$$

$$\begin{aligned} R_{1j} &= -\frac{A_j^3}{64} \\ S_{11} &= -\frac{3}{4}\left(A_1^2A_3 + 2A_1\bar{\psi}A_2^* + A_2^{*2}A_3^*\right) \\ S_{12} &= -\frac{3}{4}\left(A_1A_3^2 + 2A_2^*\bar{\psi}A_3 + A_2^{*2}A_1^*\right) \\ S_{13} &= -\frac{3}{4}\left(A_2A_3^2 + 2A_1^*\bar{\psi}A_3 + A_1^{*2}A_2^*\right) \\ T_{11} &= -\frac{A_1^2A_3^*}{12} \\ T_{12} &= -\frac{A_3^2A_1^*}{12} \\ U_{11} &= -\frac{A_1A_2^{*2}}{12} \\ U_{12} &= -\frac{A_3A_2^{*2}}{12} \\ V_{11} &= -\frac{A_1^2A_2^*}{12} \\ V_{12} &= -\frac{A_3^2A_2^*}{12}. \end{aligned} \tag{4.32}$$

We know that the particular solution to Eq. (4.22) has the form

$$\psi_2 = \sum_{j=1}^{3} P_{2j}(\mathbf{x},t)e^{i\mathbf{k}_j\cdot\mathbf{x}} + \ldots + \text{c. c.} \tag{4.33}$$

where we have shown only the resonant part of the solution. The terms on the right hand side of Eq. (4.22), resonant with lattice vector $\mathbf{k}_1$, evaluate to

$$\begin{aligned}
\Phi &= [\left(1-3\bar{\psi}^2-6(|A_1|^2+|A_2|^2+|A_3|^2)\right)(1-\mathcal{L}_{\mathbf{k}_1})P_{11}-3A_1^2(1-\mathcal{L}_{\mathbf{k}_1})P_{11}^* \\
&\quad -6A_1A_2(1-\mathcal{L}_{\mathbf{k}_1})P_{12}^*-6A_1A_3(1-\mathcal{L}_{\mathbf{k}_1})P_{13}^*-6\bar{\psi}A_3^*(1-\mathcal{L}_{\mathbf{k}_1})P_{12}^* \\
&\quad -6\bar{\psi}A_2^*(1-\mathcal{L}_{\mathbf{k}_1})P_{13}^*-6A_1A_2^*(1-\mathcal{L}_{\mathbf{k}_1})P_{12}-6A_1A_3^*(1-\mathcal{L}_{\mathbf{k}_1})P_{13} \\
&\quad -6A_2\bar{\psi}S_{11}-3A_2^2U_{11}-6A_3A_1^*T_{11}-6A_2A_1^*V_{11}-6A_1^*A_3^*S_{11}-3A_3^{*2}S_{12}-3A_2^{*2}S_{12}^* \\
&\quad -6A_3\bar{\psi}S_{13}^*-6A_1^*A_2^*S_{13}^*-3A_3^2T_{12}^*-6A_2A_3^*Q_{12}^*-6A_3A_2^*Q_{13}^*-3A_1^{*2}R_{11} \\
&\quad -6A_2A_3Q_{11}-6\bar{\psi}A_1^*Q_{11}]e^{i\mathbf{k}_1\cdot\mathbf{x}}. \qquad (4.34)
\end{aligned}$$

Thus P_{21} satisfies

$$L_{\mathbf{k}_1}P_{21}=\Phi. \qquad (4.35)$$

The non-constant terms in Φ (terms containing P_{1j}) are now ignored [34, 88] while the remaining terms are determined from their constant solutions, Eqs. (4.31) and (4.32). Thus, using Eq. (4.28) we can write the amplitude equation along lattice vector $\mathbf{k}_1$ to $\mathcal{O}(\epsilon^2)$ as

$$\begin{aligned}
\partial_t A_1 &= -(1-\mathcal{L}_{\mathbf{k}_1})\mathcal{L}_{\mathbf{k}_1}^2A_1+\epsilon[(1-3\bar{\psi}^2)A_1-3A_1(|A_1|^2+2|A_2|^2+2|A_3|^2)-6A_2^*A_3^*\bar{\psi}] \\
&\quad +\epsilon^2[\bar{\psi}^2A_1(2|A_1|^2+9|A_2|^2+9|A_3|^2)+11\bar{\psi}(2|A_1|^2+|A_2|^2+|A_3|^2)A_2^*A_3^* \\
&\quad +11\bar{\psi}A_1^2A_2A_3+\frac{27}{2}A_1^*A_2^{*2}A_3^{*2}+5A_1|A_1|^2\left(|A_2|^2+|A_3|^2\right)+12A_1|A_2|^2|A_3|^2 \\
&\quad +\frac{3}{64}A_1|A_1|^4+\frac{5}{2}A_1|A_2|^4+\frac{5}{2}A_1|A_3|^4], \qquad (4.36)
\end{aligned}$$

with cyclic permutations for lattice vectors $\mathbf{k}_2$ and $\mathbf{k}_3$.

We can in principle extend the QDRG method also to higher orders by performing the same steps above, until the point where we identify the resonant terms on the right hand side of Eq. (4.22), i.e. Φ. Combining this result with Eqs. (4.16) and (4.20) we can then obtain the amplitude equation Eq.(4.36), but with an extra term $\epsilon(1-3\bar{\psi}^2)\mathcal{L}_{\mathbf{k}_1}A_1$.

In summary, both the proto-RG and the QDRG can be calculated including terms of $O(\epsilon^2)$, and the results differ by a small but non-zero term. Which, if any, of these calculations is correct? And what is the origin of the discrepancy between the two methods? Is the QDRG result not to be trusted, being derived heuristically? Faced with two seemingly incompatible, although very similar results, it is natural to attempt an independent test of the analysis, which we did using the standard method of multiple scales. This calculation is presented below, but owing to technical complications arising from the interference of modes and the need to go to sixth order of perturbation theory, we found it only feasible to perform the calculation for the case of one dimension. Nevertheless, we will see that, in fact, the QDRG result, Eq. (4.21), is *more* correct. The small discrepancy between this result and the proto-RG result is finally resolved in Section 4.3.

4.2.3 Multiple scales derivation

We now re-derive the amplitude equation using the traditional method of multiple scales. As the primary purpose of this derivation is to verify the previous calculations via an independent method, we stick to a one dimensional analysis here that considerably simplifies the algebra. For convenience we use $\delta^2 = \epsilon$, and write Eq. (4.9) in 1-D as

$$\left[\partial_t - \partial_x^2 \left(1 + \partial_x^2\right)^2\right] \psi = \delta^2 \partial_x^2 (\psi^3 - \psi). \tag{4.37}$$

The basic premise of the multiple scales analysis is that while the pattern itself varies on the scale of its wavelength ($2\pi/k_0$), its amplitude varies on much larger length and time scales. It is then appropriate to introduce *slowly* varying arguments

$$X = \delta x \quad , \quad T = \delta^2 t \tag{4.38}$$

for the envelope function $A(X, T)$. This scaling was previously applied by Gunaratne *et al.* [91] to the Swift-Hohenberg equation with success (based on the form of the discrete dispersion relation), and as the PFC equation is essentially a conserved analog of the Swift-Hohenberg equation we anticipate that the same scaling holds here.

Derivatives scale as follows

$$\begin{aligned}
\partial_x &\rightarrow \partial_x + \delta\partial_X \\
\partial_x^2 &\rightarrow \partial_x^2 + 2\delta\partial_X\partial_x + \delta^2\partial_X^2 \\
\partial_t &\rightarrow \delta^2\partial_T,
\end{aligned} \tag{4.39}$$

whereas the operator

$$\partial_x^2\left(1+\partial_x^2\right)^2 \rightarrow \sum_{j=0}^{6}\delta^j\mathcal{L}_j \tag{4.40}$$

such that

$$\begin{aligned}
\mathcal{L}_0 &= \partial_x^2\left(1+\partial_x^2\right)^2 \\
\mathcal{L}_1 &= 4\partial_X\partial_x^3\left(1+\partial_x^2\right) + 2\partial_X\partial_x\left(1+\partial_x^2\right)^2 \\
\mathcal{L}_2 &= 4\partial_X^2\partial_x^4 + 10\partial_X^2\partial_x^2\left(1+\partial_x^2\right) + \partial_X^2\left(1+\partial_x^2\right)^2 \\
\mathcal{L}_3 &= 12\partial_X^3\partial_x^3 + 8\partial_X^3\partial_x\left(1+\partial_x^2\right) \\
\mathcal{L}_4 &= 13\partial_X^4\partial_x^2 + 2\partial_X^4\left(1+\partial_x^2\right) \\
\mathcal{L}_5 &= 6\partial_X^5\partial_x \\
\mathcal{L}_6 &= \partial_X^6.
\end{aligned} \tag{4.41}$$

We now expand ψ in a perturbation series in δ to get

$$\psi = \psi_0 + \delta\psi_1 + \delta^2\psi_2 + \delta^3\psi_3 + \ldots. \tag{4.42}$$

Using Eq. (4.39) and the above series, the δ expansion of the nonlinear term in Eq. (4.37) can be written as

$$\begin{aligned}
\partial_x^2(\psi^3-\psi) &= \partial_x^2(\psi_0^3-\psi_0) \\
&+\delta[\partial_x^2(3\psi_0^2\psi_1-\psi_1)+2\partial_X\partial_x(\psi_0^3-\psi_0)] \\
&+\delta^2[\partial_x^2(3\psi_0\psi_1^2+3\psi_0^2\psi_2-\psi_2)+2\partial_X\partial_x(3\psi_0^2\psi_1-\psi_1)+\partial_X^2(\psi_0^3-\psi_0)] \\
&+\delta^3[\partial_x^2(\psi_1^2+6\psi_0\psi_1\psi_2+3\psi_0^2\psi_3-\psi_3)+2\partial_X\partial_x(3\psi_0\psi_1^2+3\psi_0^2\psi_2-\psi_2) \\
&+\partial_X^2(3\psi_0^2\psi_1-\psi_1)] \\
&+\delta^4[\partial_x^2(3\psi_1^2\psi_2+3\psi_0\psi_2^2+6\psi_0\psi_1\psi_3+3\psi_0^2\psi_4-\psi_4) \\
&+2\partial_X\partial_x(\psi_1^2+6\psi_0\psi_1\psi_2+3\psi_0^2\psi_3-\psi_3)+\partial_X^2(3\psi_0\psi_1^2+3\psi_0^2\psi_2-\psi_2)] \\
&+\mathcal{O}(\delta^5). \qquad (4.43)
\end{aligned}$$

Substituting Eq. (4.42) in Eq. (4.37), and using the scaled operators in Eqs. (4.39-4.41), we can write equations satisfied by the ψ_m at each $\mathcal{O}(\delta^m)$. At $\mathcal{O}(1)$ we obtain,

$$\begin{aligned}
\mathcal{L}_0\psi_0 &= 0 \\
\Rightarrow \psi_0 &= \bar{\psi}+A_{01}(X,T)e^{ix}+\text{c.c.} \qquad (4.44)
\end{aligned}$$

where A_{mn} is the complex amplitude of mode n at $\mathcal{O}(\delta^m)$. At $\mathcal{O}(\delta)$ we get

$$\begin{aligned}
\mathcal{L}_0\psi_1+\mathcal{L}_1\psi_0 &= 0 \\
\Rightarrow \psi_1 &= A_{11}(X,T)e^{ix}+\text{c.c.} \qquad (4.45)
\end{aligned}$$

where (and henceforth) we neglect the constant term in view of its inclusion in Eq. (4.44). At the next order we have

$$\mathcal{L}_0\psi_2=\partial_T\psi_0-\mathcal{L}_1\psi_1-\mathcal{L}_2\psi_0-\partial_x^2(\psi_0^3-\psi_0). \qquad (4.46)$$

For $\psi_2(x,t)$ to remain bounded we have to guarantee that the right hand side of Eq. (4.46) does not have a projection in the null space of $\mathcal{L}_0$, which yields a solvability condition [97, 98] (also known as the Fredholm alternative). Applying the alternative imposes the following condition on the amplitude at $\mathcal{O}(\delta^2)$:

$$\partial_T A_{01} = 4\partial_X^2 A_{01} + (1 - 3\bar{\psi}^2)A_{01} - 3A_{01}|A_{01}|^2. \tag{4.47}$$

Thus,

$$\psi_2 = A_{21}e^{ix} + A_{22}e^{2ix} + A_{23}e^{3ix} + \text{c.c.} \tag{4.48}$$

where $A_{22} = A_{01}^2\bar{\psi}/3$, and $A_{23} = A_{01}^3/64$.

At subsequent orders, the following equations are obtained for ψ_m:

$$\begin{aligned}
\mathcal{O}(\delta^3) : \mathcal{L}_0\psi_3 &= \partial_T\psi_1 - \mathcal{L}_1\psi_2 - \mathcal{L}_2\psi_1 - \mathcal{L}_3\psi_0 \\
&\quad -[\partial_x^2(3\psi_0^2\psi_1 - \psi_1) + 2\partial_X\partial_x(\psi_0^3 - \psi_0)] \\
\mathcal{O}(\delta^4) : \mathcal{L}_0\psi_4 &= \partial_T\psi_2 - \mathcal{L}_1\psi_3 - \mathcal{L}_2\psi_2 - \mathcal{L}_3\psi_1 - \mathcal{L}_4\psi_0 \\
&\quad -[\partial_x^2(3\psi_0\psi_1^2 + 3\psi_0^2\psi_2 - \psi_2) \\
&\quad +2\partial_X\partial_x(3\psi_0^2\psi_1 - \psi_1) + \partial_X^2(\psi_0^3 - \psi_0)] \\
\mathcal{O}(\delta^5) : \mathcal{L}_0\psi_5 &= \partial_T\psi_3 - \mathcal{L}_1\psi_4 - \mathcal{L}_2\psi_3 - \mathcal{L}_3\psi_2 - \mathcal{L}_4\psi_1 \\
&\quad -\mathcal{L}_5\psi_0 - [\partial_x^2(\psi_1^2 + 6\psi_0\psi_1\psi_2 + 3\psi_0^2\psi_3 \\
&\quad -\psi_3) + 2\partial_X\partial_x(3\psi_0\psi_1^2 + 3\psi_0^2\psi_2 - \psi_2) \\
&\quad +\partial_X^2(3\psi_0^2\psi_1 - \psi_1)] \\
\mathcal{O}(\delta^6) : \mathcal{L}_0\psi_6 &= \partial_T\psi_4 - \mathcal{L}_1\psi_5 - \mathcal{L}_2\psi_4 - \mathcal{L}_3\psi_3 - \mathcal{L}_4\psi_2 \\
&\quad -\mathcal{L}_5\psi_1 - \mathcal{L}_6\psi_0 - [\partial_x^2(3\psi_1^2\psi_2 + 3\psi_0\psi_2^2 \\
&\quad +6\psi_0\psi_1\psi_3 + 3\psi_0^2\psi_4 - \psi_4) + 2\partial_X\partial_x(\psi_1^2 \\
&\quad +6\psi_0\psi_1\psi_2 + 3\psi_0^2\psi_3 - \psi_3) + \partial_X^2(3\psi_0\psi_1^2 \\
&\quad +3\psi_0^2\psi_2 - \psi_2)],
\end{aligned} \tag{4.49}$$

and successive applications of the Fredholm alternative yield the following amplitude equations at those respective orders,

$$
\begin{aligned}
\partial_T A_{11} &= -12i\partial_X^3 A_{01} + 4\partial_X^2 A_{11} - (1-3\bar{\psi}^2)2i\partial_X A_{01} + (1-3\bar{\psi}^2)A_{11} \\
&\quad -6A_{11}|A_{01}|^2 - 3A_{01}^2 A_{11}^* + 6i\partial_X(A_{01}^2 A_{01}^*) \\
\partial_T A_{21} &= -13\partial_X^4 A_{01} - 12i\partial_X^3 A_{11} + 4\partial_X^2 A_{21} - (1-3\bar{\psi}^2)(2i\partial_X A_{11} + \partial_X^2 A_{01}) \\
&\quad +(1-3\bar{\psi}^2)A_{21} - 3A_{11}^2 A_{01}^* - 6|A_{01}|^2 A_{21} - 6\bar{\psi}A_{22}A_{01}^* - 3A_{23}{A_{01}^*}^2 \\
&\quad -6A_{01}|A_{11}|^2 - 3A_{01}^2 A_{21}^* + 6i\partial_X(A_{01}^2 A_{11}^* + 2|A_{01}|^2 A_{11}) + 3\partial_X^2(A_{01}^2 A_{01}^*) \\
\partial_T A_{31} &= 6i\partial_X^5 A_{01} - 13\partial_X^4 A_{11} - 12i\partial_X^3 A_{21} + 4\partial_X^2 A_{31} - (1-3\bar{\psi}^2)(2i\partial_X A_{21} + \partial_X^2 A_{11}) \\
&\quad +(1-3\bar{\psi}^2)A_{31} - 6A_{11}A_{21}A_{01}^* - 6|A_{01}|^2 A_{31} - 6A_{01}A_{21}A_{11}^* - 6A_{23}A_{01}^* A_{11}^* \\
&\quad -6A_{01}A_{11}A_{21}^* - 3A_{01}^2 A_{31}^* - 6\bar{\psi}A_{32}A_{01}^* - 3A_{33}{A_{01}^*}^2 - 6\bar{\psi}A_{22}A_{11}^* \\
&\quad +6i\partial_X(2A_{01}|A_{11}|^2 + 2|A_{01}|^2 A_{21} + A_{01}^* A_{11}^2 + A_{01}^2 A_{21}^*) \\
&\quad +3\partial_X^2(A_{01}^2 A_{11}^* + 2|A_{01}|^2 A_{21}^*) + \text{h.o.t.} \\
\partial_T A_{41} &= \partial_X^6 A_{01} + 6i\partial_X^5 A_{11} - 13\partial_X^4 A_{21} - 12i\partial_X^3 A_{31} + 4\partial_X^2 A_{41} \\
&\quad -(1-3\bar{\psi}^2)(2i\partial_X A_{31} + \partial_X^2 A_{21}) + (1-3\bar{\psi}^2)A_{41} - 3A_{21}^2 A_{01}^* - 6A_{11}A_{31}A_{01}^* \\
&\quad -6A_{01}A_{41}A_{01}^* - 6A_{11}A_{21}A_{11}^* - 6A_{01}A_{31}A_{11}^* - 3A_{11}^2 A_{21}^* - 6A_{01}|A_{21}|^2 \\
&\quad -6A_{01}A_{11}A_{31}^* - 3A_{01}^2 A_{41}^* - 6\bar{\psi}A_{42}A_{01}^* - 3A_{43}{A_{01}^*}^2 - 6\bar{\psi}A_{32}A_{11}^* \\
&\quad -6A_{33}A_{01}^* A_{11}^* - 3A_{23}{A_{11}^*}^2 - 6\bar{\psi}A_{33}A_{22}^* - 6A_{01}|A_{23}|^2 + 6i\partial_X(2A_{11}A_{21}A_{01}^* \\
&\quad +2|A_{01}|^2 A_{31} + A_{11}|A_{11}|^2 + 2A_{01}A_{21}A_{11}^* + 2A_{01}A_{11}A_{21}^* + A_{01}^2 A_{31}^*) \\
&\quad +3\partial_X^2(2A_{01}|A_{11}|^2 + A_{01}^* A_{11}^2 + 2|A_{01}|^2 A_{21} + A_{01}^2 A_{21}^*) + \text{h.o.t.}
\end{aligned}
\tag{4.50}
$$

Here, "h.o.t." refers to higher order terms that are functions of A_{01} and its derivatives. The amplitude function for the pattern (e^{ix}) can be written as

$$
A(X,T) = A_{01}(X,T) + \delta A_{11}(X,T) + \delta^2 A_{21}(X,T) + \ldots. \tag{4.51}
$$

Using Eqs. (4.47), (4.50), and (4.51), and scaling back to original variables, i.e. $X \to \delta^{-1}x$ and $T \to \delta^{-2}t$, the amplitude equation to $\mathcal{O}(\delta^4)$ can be written as

$$\begin{aligned}\partial_t A &= 4\partial_x^2 A - 12i\partial_x^3 A - 13\partial_x^4 A + 6i\partial_x^5 A + \partial_x^6 A - \delta^2(1-3\bar{\psi}^2)\left(2i\partial_x + \partial_x^2\right)A \\ &\quad +\delta^2\left[(1-3\bar{\psi}^2)A - 3A|A|^2 + 3\left(2i\partial_x + \partial_x^2\right)\left(A|A|^2\right)\right] \\ &\quad -\delta^4\left(\frac{3}{64}A|A|^4 + 2\bar{\psi}^2 A|A|^2\right) + \mathcal{O}(\delta^6) \qquad (4.52)\end{aligned}$$

or more compactly, after replacing $\delta^2 \to \epsilon$, to $\mathcal{O}(\epsilon^2)$

$$\begin{aligned}\partial_t A &= -\left(1-\mathcal{L}_{1D}\right)\mathcal{L}_{1D}{}^2 A - \epsilon\left[(1-3\bar{\psi}^2)\mathcal{L}_{1D}A + (1-3\bar{\psi}^2)A - 3A|A|^2 + 3\mathcal{L}_{1D}(A|A|^2)\right] \\ &\quad -\epsilon^2\left(\frac{3}{64}A|A|^4 + 2\bar{\psi}^2 A|A|^2\right) + \mathcal{O}(\epsilon^3), \qquad (4.53)\end{aligned}$$

where $\mathcal{L}_{1D} \equiv (2i\partial_x + \partial_x^2)$.

Let us now compare Eq. (4.53) with the one dimensional equivalents of the $\mathcal{O}(\epsilon)$ amplitude equations that we have previously derived for hexagonal patterns, i.e. Eqs. (4.21) and (4.29). Without re-deriving, the one dimensional equivalents are readily obtained by setting

$$A_2 = A_3 = 0 \quad \text{and} \quad \mathcal{L}_{\mathbf{k}_2} = \mathcal{L}_{1D} \qquad (4.54)$$

in those equations. We observe that Eq. (4.53) (also truncated to $\mathcal{O}(\epsilon)$) contains at least one term which is not present in either of the equations previously derived.

We note that the QDRG result of Eq. (4.21) is closer to the multiple scales result compared to the proto-RG result (and the RG result in section 4.2.4), in that it fails to capture only the nonlinear derivative term at $O(\epsilon)$, which is actually a higher order correction to $3A|A|^2$. This is clearly because the spatial operator in the QDRG method is an outcome of a *linear* stability analysis, whereas one would have to perform a nonlinear stability analysis to obtain nonlinear spatial derivative terms. The clear advantage of the QDRG calculation however is that it was done with significantly less effort, and in a rotationally-covariant manner; perturbation theory to $O(\epsilon)$ was all that was required. The multiple scales analysis, on the other hand, required a sixth order perturbation

theory treatment, and in order to simplify the algebra, we only worked in one dimension. In higher dimensions, the interference between the modes would have created a huge increase in the complexity at each successively higher order in perturbation theory. The QDRG calculation is only heuristic, but as we will show below, can be justified from a full calculation, albeit with a slight technical modification of the previously-published recipe, to take into account the special feature of the conservation law.

We conclude therefore that although the QDRG result of Eq. (4.21) and the multiple scales method to $O(\epsilon)$ still do not yield consistent results, the QDRG method is still an improvement over the proto-RG method. In order to track down the source of the discrepancy, we next attempted a full RG calculation without any shortcuts, i.e. systematically calculating explicitly and renormalizing all the divergent terms to $O(\epsilon)$.

4.2.4 Renormalization group derivation

In this section, we present a derivation of the amplitude equation using the conventional RG method, in one dimension for pedagogical simplicity (just as done for the method of multiple scales). The calculation is complicated because of the need to obtain explicit formulae for the secular divergences [32,33], but this is possible at the order to which we worked.

Starting from Eq. (4.37) (with δ^2 replaced by ϵ) and a naive perturbation series in ϵ as in Eq. (4.17) the zeroth and first order solutions can be written as

$$\begin{aligned} \psi_0 &= \bar{\psi} + Ae^{ix} + \text{c.c.} \\ \psi_1 &= P_1(x,t)e^{ix} + Q_1 e^{2ix} + R_1 e^{3ix} + \text{c.c.} \end{aligned} \tag{4.55}$$

The difficulty in the conventional RG method comes from the need to explicitly determine the form of the secular coefficient P_1. While this is a routine task for ODEs, it is far from trivial for PDEs. A further complication is that the solution for P_1 must be the highest order polynomial that satisfies the PDE, to be able to eliminate *all* secular divergences. It turns out that this is critical to obtaining the rotationally covariant operator at a lower

order in ϵ. Using the method of undetermined coefficients we find such a solution to be

$$P_1(x,t) = \epsilon(1 - 3\bar{\psi}^2 - 3|A|^2)A \sum_{j=1}^{6} C_j P_{1j}(x,t), \tag{4.56}$$

where

$$\begin{aligned}
P_{11} &= t \\
P_{12} &= -\frac{1}{720}(-89280t^2 + 7680t^3 + 4320ixt - 34560ixt^2 \\
&\quad -4680x^2t + 2880x^2t^2 - 1440ix^3t + 120x^4t + x^6) \\
P_{13} &= \frac{i}{720}(-5760it^2 - 1560xt + 960xt^2 - 720ix^2t \\
&\quad +80x^3t + x^5) \\
P_{14} &= \frac{1}{312}(192t^2 - 288ixt + 48xt^2 + x^4) \\
P_{15} &= -\frac{i}{72}(24xt + x^3) \\
P_{16} &= -\frac{x^2}{8},
\end{aligned} \tag{4.57}$$

and the constants C_j satisfy $\sum_{j=1}^{6} C_j = 1$.

The RG method proceeds as follows: (1) dummy variables X and T are introduced, (2) the divergent terms in P_{1j} of the form $x^m t^n$ are split to read $x^m t^n = (x^m t^n - X^m T^n) + X^m T^n$, (3) the constant amplitude A is redefined using an ϵ expansion $A = A_R(X,T)(1 + \sum_{j=1} \epsilon^j Z_j)$, where A_R is now the renormalized amplitude, and Z_j are the renormalization constants which are chosen order by order in ϵ to absorb the $X^m T^n$ terms, and (4) since the solution ψ is independent of X and T, all derivatives of ψ with respect X, T, or a combination thereof must be zero. This last condition yields the following RG equations

$$\begin{aligned}
\frac{\partial A_R}{\partial T} &= C_1\epsilon(1 - 3\bar{\psi}^2 - 3|A|^2)A \\
-\frac{\partial^6 A_R}{\partial X^6} &= C_2\epsilon(1 - 3\bar{\psi}^2 - 3|A|^2)A \\
-6i\frac{\partial^5 A_R}{\partial X^5} &= C_3\epsilon(1 - 3\bar{\psi}^2 - 3|A|^2)A
\end{aligned}$$

$$
\begin{aligned}
13\frac{\partial^4 A_R}{\partial X^4} &= C_4\epsilon(1-3\bar{\psi}^2-3|A|^2)A \\
12i\frac{\partial^3 A_R}{\partial X^3} &= C_5\epsilon(1-3\bar{\psi}^2-3|A|^2)A \\
-4\frac{\partial^2 A_R}{\partial X^2} &= C_6\epsilon(1-3\bar{\psi}^2-3|A|^2)A, \qquad (4.58)
\end{aligned}
$$

at $\mathcal{O}(\epsilon)$. Further, using $\sum_{j=1}^{6} C_j = 1$ and replacing $A_R \to A$, $X \to x$, and $T \to t$, the above equations can be combined to read

$$
\partial_t A + (1-\mathcal{L}_{1D})\,{\mathcal{L}_{1D}}^2 A = \epsilon(1-3\bar{\psi}^2)A - 3\epsilon A|A|^2, \qquad (4.59)
$$

which is also the 1-D proto-RG equation.

We close this section with some interesting observations. (i) The equations in (4.58) do not form a unique set of solvability conditions. Other equations are possible, e.g.

$$
\begin{aligned}
-\frac{1}{16}\frac{\partial^4 A_R}{\partial X^2 \partial T^2} &= C_2\epsilon(1-3\bar{\psi}^2-3|A|^2)A \\
-\frac{3i}{8}\frac{\partial^3 A_R}{\partial X \partial T^2} &= C_3\epsilon(1-3\bar{\psi}^2-3|A|^2)A \\
&\vdots \qquad (4.60)
\end{aligned}
$$

The choice of Eqn. (4.58) is motivated by the observation that it yields a rotationally covariant amplitude equation, and other physical considerations such as the microscopic equation being only first order in time. (ii) The list of possible terms P_{1j} does not include the leading polynomial term Bx, where B is an arbitrary constant, as this term is annihilated by the kernel of the PDE. Thus no constraint is available to fix B. It turns out that unless this term is also renormalized, all secular divergences are not removed. This may explain the absence of certain terms in Eq. (4.59) that however show up in the multiple scales analysis. To be certain, the calculation needs to be carried out to higher orders; but we do not attempt this here.

4.3 Operator ordering ambiguity and its resolution in the RG method

In this section, we resolve the discrepancy between the answers generated by the QDRG method, the RG methods, and the method of multiple scales. Curiously, no such discrepancy was observed in the treatment of the Swift-Hohenberg equation, a non-conservative OPE, by RG methods [32, 33, 88] and multiple scales techniques [91]. The reader may recall that it was ascertained in Section 4.2.1.1 that the QDRG method too produces the same result as the other methods for this equation. Why then does a discrepancy arise in the PFC equation? Clearly, the role played by the extra Laplacian, a consequence of the conservation law in this case, must be non-trivial!

Note that this Laplacian operator carries over to the right hand side of both Eq. (4.18), the $\mathcal{O}(\epsilon)$ equation for the RG methods, and Eq. (4.46), the $\mathcal{O}(\epsilon)$ equation for multiple scales. However also note that, in the method of multiple scales, in addition to the non-linear terms, this operator is also subjected to an ϵ expansion. There is no provision in *any* of the RG methods to allow the same to happen to the Laplacian. In other words, the operator may very well have not existed on the right hand side at $\mathcal{O}(\epsilon)$, and we would have obtained exactly the same result as before!

A clue to the subtlety is to look at the way in which the secular terms are renormalized. The naive way, as followed here, would be to evaluate the right hand side first, look for secular terms later, and then renormalize these divergent coefficients. However, this will not eliminate secular terms generated by the differential operator. In order to eliminate *all* secular terms, the amplitude must be renormalized *before* differentiation, for the simple reason that renormalization and differentiation are non-commutable operations. In other words, there is an operator ordering ambiguity in the implementation of the renormalization group method, exposed in this problem by the conservation law. Performing the calculation with the operations of renormalization and differentiation reversed is equivalent to performing an ϵ expansion in the differential operator.

We find that by following this procedure, additional terms in the coefficients of the resonant modes are automatically generated. Specifically, when we evaluate the right hand side of Eq. (4.18) after assuming the amplitudes of ψ_0 to have a space-time dependence, the renormalized coefficients of the resonant $\exp(i\mathbf{k}_1 \cdot \mathbf{x})$ forcing term work out to be

$$\begin{aligned}
&\epsilon[(1-3\bar{\psi}^2)A_1 - 3A_1\left(|A_1|^2+2|A_2|^2+2|A_3|^2\right) - 6A_2^*A_3^*\bar{\psi} - (1-3\bar{\psi}^2)\mathcal{L}_{\mathbf{k}_1}A_1 \\
&+6\left(|A_1|^2+|A_2|^2+|A_3|^2\right)\mathcal{L}_{\mathbf{k}_1}A_1 + 6A_1^*|\nabla A_1|^2 + 3A_1^2\mathcal{L}_{\mathbf{k}_1}A_1^* + 6A_1A_2^*\mathcal{L}_{\mathbf{k}_1}A_2 \\
&+6A_1A_2\mathcal{L}_{\mathbf{k}_1}A_2^* + 6A_1A_3^*\mathcal{L}_{\mathbf{k}_1}A_3 + 6A_1A_3\mathcal{L}_{\mathbf{k}_1}A_3^* + 6\bar{\psi}A_3^*\mathcal{L}_{\mathbf{k}_1}A_2^* + 6\bar{\psi}A_2^*\mathcal{L}_{\mathbf{k}_1}A_3^* \\
&+12\bar{\psi}\nabla A_2^*\cdot\nabla A_3^* + 12A_1\left(\nabla A_1\cdot\nabla A_1^* + \nabla A_2\cdot\nabla A_2^* + \nabla A_3\cdot\nabla A_3^*\right) + 12A_2\nabla A_1\cdot\nabla A_2^* \\
&+12A_2^*\nabla A_1\cdot\nabla A_2 + 12A_3\nabla A_1\cdot\nabla A_3^* + 12A_3^*\nabla A_1\cdot\nabla A_3], \qquad (4.61)
\end{aligned}$$

which when specialized for the 1-D case becomes

$$\begin{aligned}
&\epsilon[(1-3\bar{\psi}^2)A - 3A|A|^2 - (1-3\bar{\psi}^2)\mathcal{L}_{1D}A + 6|A|^2\mathcal{L}_{1D}A \\
&+3A^2\mathcal{L}_{1D}A^* + 6A^*\left(\frac{\partial A}{\partial x}\right)^2 + 12A\frac{\partial A}{\partial x}\frac{\partial A^*}{\partial x}] \\
= \;&\epsilon[(1-3\bar{\psi}^2)A - 3A|A|^2 - (1-3\bar{\psi}^2)\mathcal{L}_{1D}A + 3\mathcal{L}_{1D}(A|A|^2)]. \qquad (4.62)
\end{aligned}$$

We note that the above terms are identical to the $\mathcal{O}(\epsilon)$ terms on the right hand side of Eq. (4.53). Therefore the correct amplitude equation to $\mathcal{O}(\epsilon)$ should contain all the terms in Eq. (4.61). In order to illustrate the generality of this approach, we apply this idea again in the appendix to the Van der Pol oscillator, another equation for which the previously reported implementation of the RG method, and the method of multiple scales produce different answers.

We wish to point out that the assumption of a constant amplitude in the ψ_0 solution makes it possible for the coefficients of the non-resonant terms in ψ_1 to assume constant values, a fact that is favorably used in extending the proto-RG calculation to the next order. However, with our modification to the proto-RG procedure, it is clear that for the PFC equation at least, non-resonant coefficients cannot have constant val-

ues. Thus computing higher order corrections to the amplitude equations, will require explicit construction of particular solutions, which may limit progress beyond $\mathcal{O}(\epsilon)$ by purely analytical methods.

4.4 Concluding remarks

In this chapter, we have presented a detailed illustration of various perturbative techniques to derive amplitude equations from order parameter equations that produce periodic patterns. Amplitude equations serve as powerful analytical tools with which to investigate pattern stability and defect interactions, as well as accurate coarse-grained descriptions of pattern forming systems, and this calls for practical and reliable mathematical methods for deriving them.

Although our benchmark for accuracy is the widely-accepted method of multiple scales, it is critical to note that this method is not failsafe, because it requires *a priori* identification of the way in which space and time scale with the small parameter ϵ. There are many instances where surprising scales emerge that would not easily be identified *a priori* (e.g. see the analysis of the Mathieu equation in [32]).

The method of multiple scales typically involves a very lengthy calculation before a rotationally covariant operator ensues, and involves computation of various higher order terms which ultimately do not improve the overall result significantly. In the example presented here, a sixth order calculation was required to get the lowest order amplitude equation. The reader should bear in mind that the fairly involved calculation shown in this chapter was only one dimensional.

On the other hand, the practicality of RG based methods, where the amplitude equation was obtained very quickly at $\mathcal{O}(\epsilon)$ itself, is self-evident. No guesswork was required to determine the scaling of the variables and all calculations started with naive perturbation expansions in ϵ. In particular, our so called "quick and dirty" (QDRG) method and the proto-RG method are attractive techniques, because there is virtually no need to construct explicit solutions. Both methods use only information available from the

differential equation and in that sense, are very general ways of building a controlled coarse-grained approximation to the order parameter equation being studied. Furthermore, the QDRG method gives the correct result quickly, apart from a small non-linear rotationally covariant gradient term which is not captured by the linear stability argument.

For the same order in ϵ, we have shown that the QDRG method produces a more accurate amplitude equation compared to the proto-RG method, by capturing certain extra terms that are revealed in the multiple scales analysis. However, with our modification (commuting differentiation and renormalization) to the way in which the RG is implemented, we find that all methods converge identically.

Chapter 5

Numerical Solution of Amplitude Equations on Fixed Grids

In this chapter we compare numerical solutions of the complex amplitude equations with solutions of the PFC equation, Eq. (3.9), using the problem of two-dimensional grain nucleation and growth as an example, and also establish the computational advantage of this approach versus direct numerical simulation of the nanoscopic OPE.

The evolution equation for the amplitude A_1 in Eq. (4.21) and the cyclic permutations for A_2 and A_3, when rescaled to original variables read

$$\begin{aligned}
\frac{\partial A_1}{\partial t} &= \widetilde{\mathcal{L}}_1 A_1 - 3A_1\left(|A_1|^2 + 2|A_2|^2 + 2|A_3|^2\right) - 6\bar{\psi}A_2^* A_3^* \\
\frac{\partial A_2}{\partial t} &= \widetilde{\mathcal{L}}_2 A_2 - 3A_2\left(2|A_1|^2 + |A_2|^2 + 2|A_3|^2\right) - 6\bar{\psi}A_1^* A_3^* \\
\frac{\partial A_3}{\partial t} &= \widetilde{\mathcal{L}}_3 A_3 - 3A_3\left(2|A_1|^2 + 2|A_2|^2 + |A_3|^2\right) - 6\bar{\psi}A_1^* A_2^*,
\end{aligned} \tag{5.1}$$

where,

$$\widetilde{\mathcal{L}}_j = \left[1 - \nabla^2 - 2i\mathbf{k}_j \cdot \nabla\right]\left[-r - 3\bar{\psi}^2 - \left\{\nabla^2 + 2i\mathbf{k}_j \cdot \nabla\right\}^2\right] \tag{5.2}$$

is the rotationally covariant operator, and ϵ in Eq. (4.21) has been replaced by $-r$ in Eq. (5.1) to stay consistent with the notation of Eq. (3.9).

5.1 Numerical methods and implementation ideas

We evolve A_j using an $\mathcal{O}(\Delta t, \Delta x^2)$ finite difference discretization of Eq. (5.1), where Δt is the time step size and Δx is the grid spacing. The spatial discretizations of the Laplacian and gradient operators are given in Eqs. (B.1) and (B.5) respectively. While the nine point discretization of the Laplacian operator is essential in order to avoid checkerboard instabilities, even a simple central difference discretization for the gradient operator as in Eq. (B.2) is enough, provided Δx is sufficiently small. We have, however, noticed significant improvement in solution quality if Eq. (B.5) is used. In certain situations, it was possible to solve Eq. (5.1) on a coarser non-uniform grid, with rectangular elements. For those simulations, the discretizations of the Laplacian and gradient operators are given by Eqs. (B.6) and (B.8) respectively. Note that these discrete forms are consistent with the discrete forms in Eqs. (B.1) and (B.2) for the special case of a uniform grid. The density field ψ is reconstructed from A_j using Eq. (3.20).

We adopt a straightforward solution strategy in this chapter. We separate the complex amplitudes A_j in Eq. (5.1) into their respective real and imaginary parts, and in this manner obtain *six* evolution equations which are then evolved using a Forward-Euler time discretization. As expected, this places a stability constraint on Δt, which assumes a power-law dependence on Δx. Upon numerically examining the stability of the discrete version of Eq. (5.1), we find that the criterion

$$\Delta t \leq 0.003 \Delta x^5 \tag{5.3}$$

guarantees linearly stable solutions for $\Delta x \in [\pi/16, \pi]$.

An important idea in the numerical implementation of Eq. (5.1) (as well as of Eq. (3.9) earlier) is the "implicit" computation of all higher order derivatives. For instance, even-though Eq. (5.1) has a sixth order derivative, we never explicitly discretize a sixth order operator. Instead, $\nabla^6 A_j$ is computed as $\nabla^2[\nabla^2(\nabla^2 A_j)]$, where each term operated upon by the Laplacian is discretized using the nine point stencil in Eq. (B.1). While this is entirely equivalent to discretizing the operator ∇^6 explicitly on a 49 point stencil, it is

much more efficient, allowing reuse of previously computed quantities (for example $\nabla^2 A_j$ and $\nabla^2(\nabla^2 A_j)$).

5.2 Multiple crystal orientations and "beats"

A fixed set of reciprocal lattice vectors $\mathbf{k}_j$, given by Eq. (3.21) with $k_0 = 1$, is used in all our computations. This poses a tricky question. How do we incorporate multiple crystal orientations using a single set of reciprocal lattice vectors?

While the density field ψ on a triangular lattice with basis $\mathbf{k}_j$ is described by Eq. (3.20), the density field on a lattice with basis $\mathbf{k}_j(\theta)$, where $|\mathbf{k}_j(\theta)| = 1$, rotated from the basis vectors $\mathbf{k}_j$ by an angle θ, is described by

$$\psi(\theta) = \sum_{j=1}^{3} A_j e^{i\mathbf{k}_j(\theta)\cdot\mathbf{x}} + \sum_{j=1}^{3} A_j^* e^{-i\mathbf{k}_j(\theta)\cdot\mathbf{x}} + \bar{\psi}. \tag{5.4}$$

Eq. (5.4) therefore describes the density field of a grain misoriented with respect to the basis vectors.

Further, $\mathbf{k}_j(\theta) = \mathbf{k}_j + \delta\mathbf{k}_j(\theta)$, where the vector $\delta\mathbf{k}_j(\theta)$ measures the rotation of each lattice vector. Therefore,

$$\psi(\theta) = \sum_{j=1}^{3} A_j e^{i\delta\mathbf{k}_j(\theta)\cdot\mathbf{x}} e^{i\mathbf{k}_j\cdot\mathbf{x}} + \sum_{j=1}^{3} A_j^* e^{-i\delta\mathbf{k}_j(\theta)\cdot\mathbf{x}} e^{-i\mathbf{k}_j\cdot\mathbf{x}} + \bar{\psi}, \tag{5.5}$$

or

$$\psi(\theta) = \sum_{j=1}^{3} A_j^\theta e^{i\mathbf{k}_j\cdot\mathbf{x}} + \sum_{j=1}^{3} A_j^{\theta *} e^{-i\mathbf{k}_j\cdot\mathbf{x}} + \bar{\psi}, \tag{5.6}$$

where

$$A_j^\theta = A_j e^{i\delta\mathbf{k}_j(\theta)\cdot\mathbf{x}}. \tag{5.7}$$

Thus grains arbitrarily misoriented from the global basis $\mathbf{k}_j$ can still be described in terms of $\mathbf{k}_j$ by suitably modifying the amplitude A_j according to Eq. (5.7). Therefore, a straightforward way to include differently oriented grains in the system is to specify an

initial condition via Eq. (5.6). By making the amplitude a non-uniform complex function with a periodic structure, multiple grain orientations are automatically included. Fig. 5.1 illustrates this idea. Fig. 5.1(a) shows the real component of one of the three complex amplitude functions A_j, specified by Eq. (5.7), and Fig. 5.1(b) shows the corresponding density field constructed using Eq. (5.6).

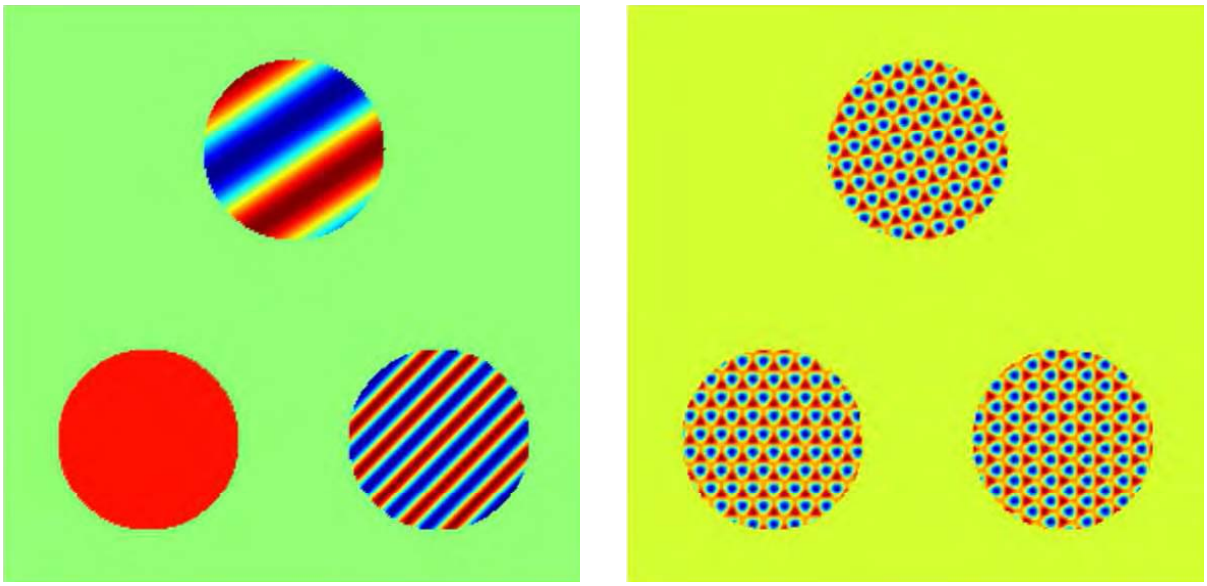

(a) $\Re(A_1)$ (b) ψ

Figure 5.1: (a) Real component of the complex amplitude A_1. As the grain in the bottom-left corner is aligned with the basis $\mathbf{k}_j$ in Eq. (3.21) its amplitude is constant, while amplitudes of the remaining misoriented grains have "beats". (b) Density field ψ reconstructed using Eq. (5.6). Clockwise from the lower left corner, $\theta = 0$, $\pi/24$ and $\pi/6$.

Eq. (5.1), being rotationally covariant, has the property of preserving these "beat" like structures in the amplitudes (and therefore the corresponding orientation of the grain), and hence any misoriented grain, remains so misoriented as the system evolves[1]. An exception to this situation is when similarly oriented grains collide to form "small angle" grain boundaries. Under such circumstances, the interactions can cause the frequency of the "beats" to shift, implying grain rotation, a phenomenon that has been documented in experiments.

[1]This property is critical to evolving polycrystalline systems.

5.3 Model verification

Fig. (5.2) compares the time evolution for the heterogeneous nucleation and growth of a two-dimensional film, calculated using the PFC equation, Eq. (3.9) and its RG-generated counterpart, Eq. (5.1), for $\bar{\psi} = 0.285$ and $r = -0.25$. Note from Fig. 3.1 that this set of parameters should lead to the growth of a stable triangular phase from the constant phase.

The computations were performed on uniform grids, squares of side 192π, with $\Delta x = \Delta y = \pi/4$ for the PFC equation, and $\Delta x = \Delta y = \pi/2$ for the complex amplitude equations. We have verified that these choices of the grid spacing guarantee grid converged results in each case. The initial condition comprised twelve randomly oriented and located grains, each of radius 4π. As seen from Fig. (5.2), the crystalline domains grow, colliding to form a polycrystalline nanostructure. The solutions from the two different computational algorithms are essentially indistinguishable, indicating excellent qualitative agreement.

As a more rigorous demonstration of accuracy, we also compare the computed grain boundary energy as a function of misorientation angle for two grains, using the two algorithms. The initial condition for this test comprises two misaligned crystals separated by a narrow strip of liquid, on a periodic domain (see Fig. 5.3). One of the crystals is misoriented with respect to the other by θ as in Fig. 5.3(a), and the system is evolved for a very long time ($t \sim 3000$) until equilibrium conditions are reached, i.e. until the free energy of the system is relatively time invariant. The resulting structure contains a pair of grain boundaries of length $\approx L_y$, where L_y is the length of the domain in the y direction, each delineated by a regular array of dislocations as seen in Fig. 5.3(b).

The grain boundary energy γ is computed as follows. We first compute the free energy of a perfect crystal by running the same simulation with $\theta = 0$, and evaluating $\mathcal{F}(0)$ as per Eq. (3.7) (the integral is approximated as a Riemann sum). We then compute the free energy $\mathcal{F}(\theta)$ of the state with the grain boundary, i.e. Fig. 5.3(b). The excess energy per unit length of the grain boundary $[\mathcal{F}(\theta) - \mathcal{F}(0)]/(2L_y)$ equals γ. We repeat

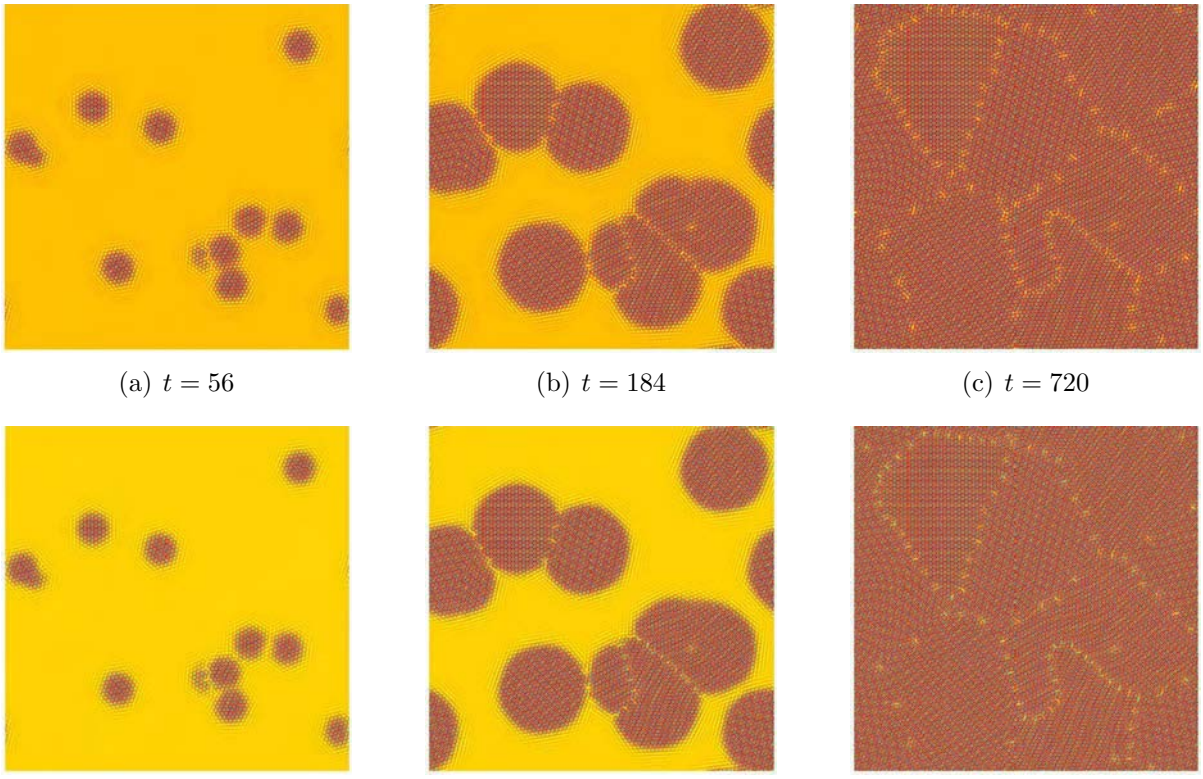

(a) $t = 56$ (b) $t = 184$ (c) $t = 720$

(d) $t = 56$ (e) $t = 184$ (f) $t = 720$

Figure 5.2: Comparison of heterogeneous nucleation and growth in the PFC equation, Eq. (3.9) (panels (a)-(c)), and its RG-generated mesoscale counterpart, Eq. (5.1) (panels (d)-(f)). The order parameter is shown at the times indicated starting from the same initial condition with $\bar{\psi} = 0.285$ and $r = -0.25$.

this procedure for different values of θ, ranging from 0 to $\pi/6$, which is the maximum possible misorientation between two crystals with hexagonal symmetry.

Fig. (5.4) compares the normalized predictions of the two models with the Read-Shockley equation [106], a well known theoretical result for small angle grain boundaries, which has been scaled to fit large misorientation data. The agreement is remarkably good for both low and high angle grain boundaries, and the values predicted by the amplitude equations closely follow the trends set by the PFC equation (data obtained from [28]) and the Read-Shockley equation. The maximum difference between the absolute values of the free energy, as computed respectively by the amplitude equations and the PFC equation over all θ, is about 1.6%.

We conclude that the coarse-grained amplitude equations can indeed be highly accurate proxies to the nanoscopic PFC equation.

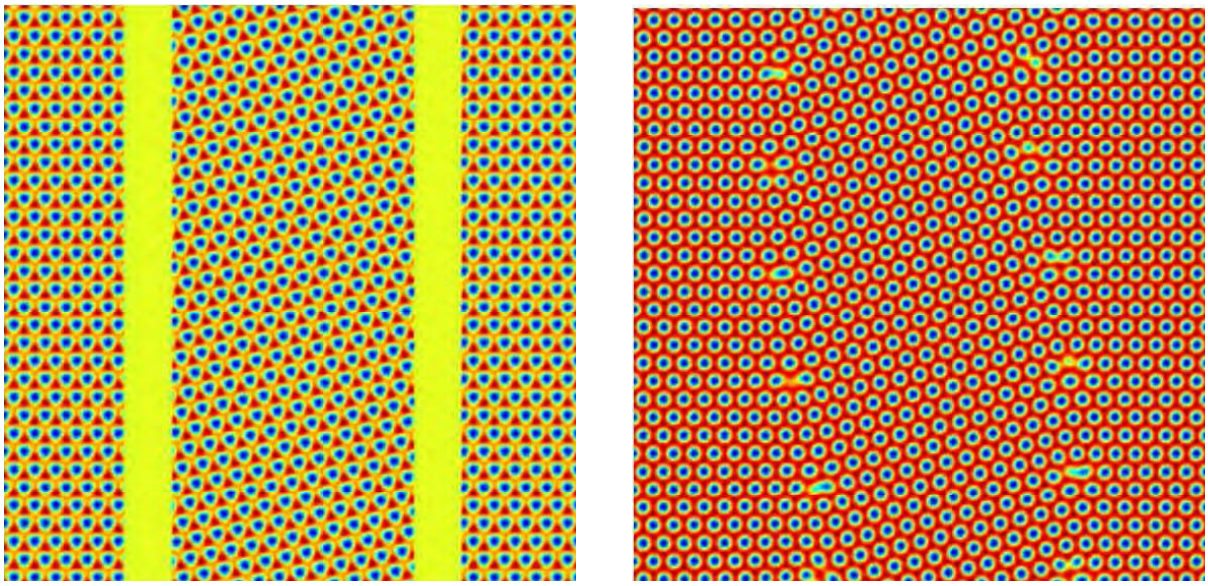

(a) Initial condition (b) After time evolution

Figure 5.3: In (a) the crystal in the center is misoriented from the one on the periodic boundary by $\theta = \pi/16$. As the crystals evolve, a pair of grain boundaries highlighted by regular array of dislocations are formed.

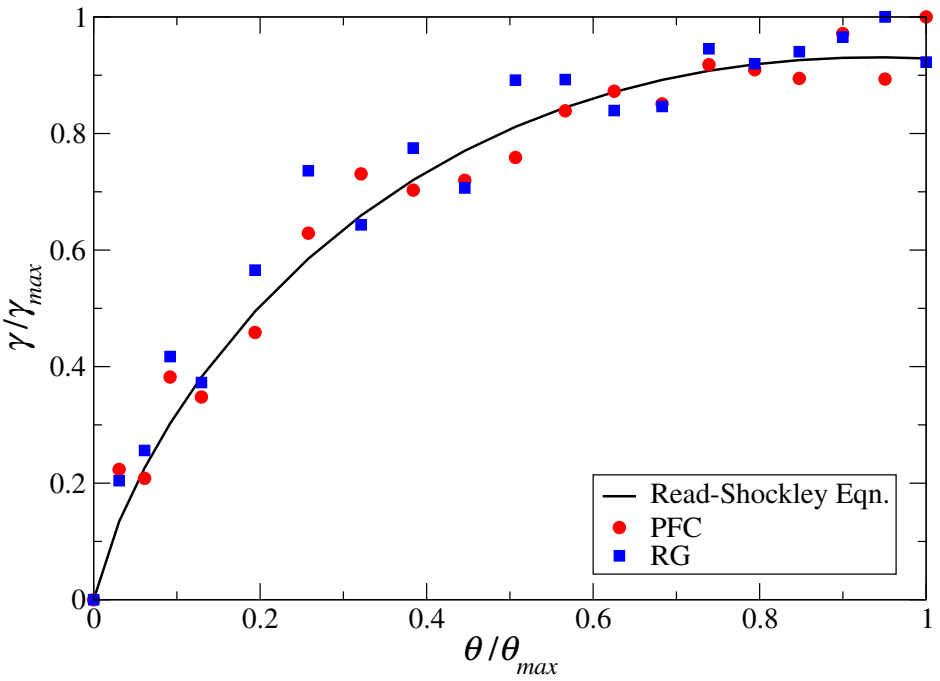

Figure 5.4: Comparison of grain boundary energy predicted by the amplitude equations and the PFC equation, with Read-Shockley theory.

5.4 Computational efficiency

An apparent problem with our approach, which the reader may have immediately spotted, is that we have traded a single sixth order scalar OPE, i.e. Eq. (3.9), for a system of six (3 amplitude fields $\times$ 2 components) sixth order partial differential equations, i.e. Eq. (5.1). It is clear then that we have increased the computational complexity of the numerical algorithm by a factor of six on the same mesh, roughly speaking. How then, is our approach computationally efficient? Note that until this point, we have not exploited the uniformity of the amplitude modulus and phase variables to speed up computations. Nonetheless, even with this rather naive implementation, we will show that it is still computationally advantageous to solve amplitude equations instead of the PFC equation.

Fig. 5.5 (inset) shows grid convergence behavior in the Read-Shockley test of the solutions to the PFC and complex amplitude equations. The crystals are misoriented by the maximum possible angle, $\pi/6$. We define the error $\varepsilon_0 = \left| \|y^{\Delta x}\|_2 - \|y^0\|_2 \right|$, where

$\|y^{\Delta x}\|_2$ is the L_2 norm of the solution for a mesh spacing of Δx, and $\|y^0\|_2$ is the L_2 norm obtained by Richardson extrapolation to $\Delta x = 0$ consistent with a second order finite difference method. For a comparable level of accuracy, we see that $\Delta x_{RG} \approx 2\Delta x_{PFC}$ is a sufficiently small mesh spacing for the RG equations. Further, with a Forward-Euler time evolution scheme and its attendant stability constraint on the time step for each equation, we find that $\Delta t_{RG} \approx 6\Delta t_{PFC}$. Clearly therefore, the amplitude/RG equations offer significant opportunities for improved computational efficiency. Fig. 5.5 compares

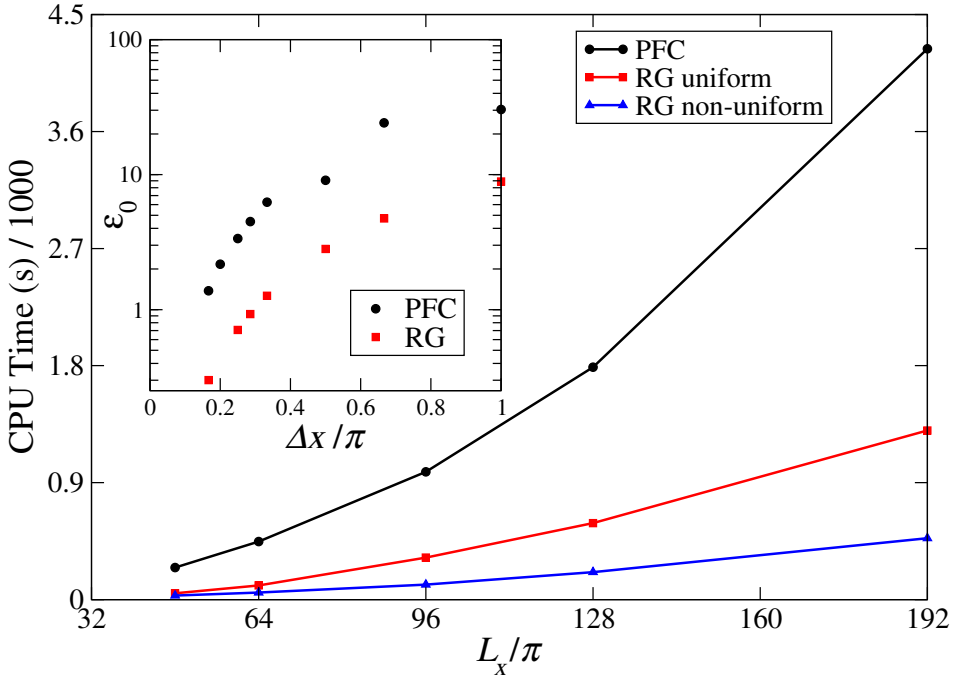

Figure 5.5: Scaling of CPU time versus domain length L_x for the PFC and RG equations. Inset shows error in the respective solutions with diminishing mesh spacing Δx.

the CPU time as a function of domain size L_x for the Read-Shockley test with $\Delta\theta = 3.88°$, $r = -0.25$ and $\bar{\psi} = 0.28$, showing that the CPU time required for the RG equations is about 4-5 times lesser than that required for the PFC equations. Consistent with the grid convergence behavior described above, we chose $\Delta x_{PFC} = \pi/4$, $\Delta t_{PFC} = 0.008$, $\Delta x_{RG} = \pi/2$ and $\Delta t_{RG} = 0.05$. The difference in the free energy predicted by the RG equations and PFC equations was $< 1\%$.

For the Read-Shockley problem in particular, since the general location of the grain boundaries can be guessed *a priori*, it is easy to construct an appropriate non-uniform mesh, which while adequately resolving the beats within the misoriented grains, has its finest elements spread over the grain boundaries. Such a mesh, spanning a square domain of side 128π is shown in Fig. 5.6, which shows a contour plot of $\Re(A_1)$ and contours of the average amplitude modulus. The latter brings out crystalline imperfections rather nicely as regions with steep amplitude gradients. For these simulations, we chose a constant

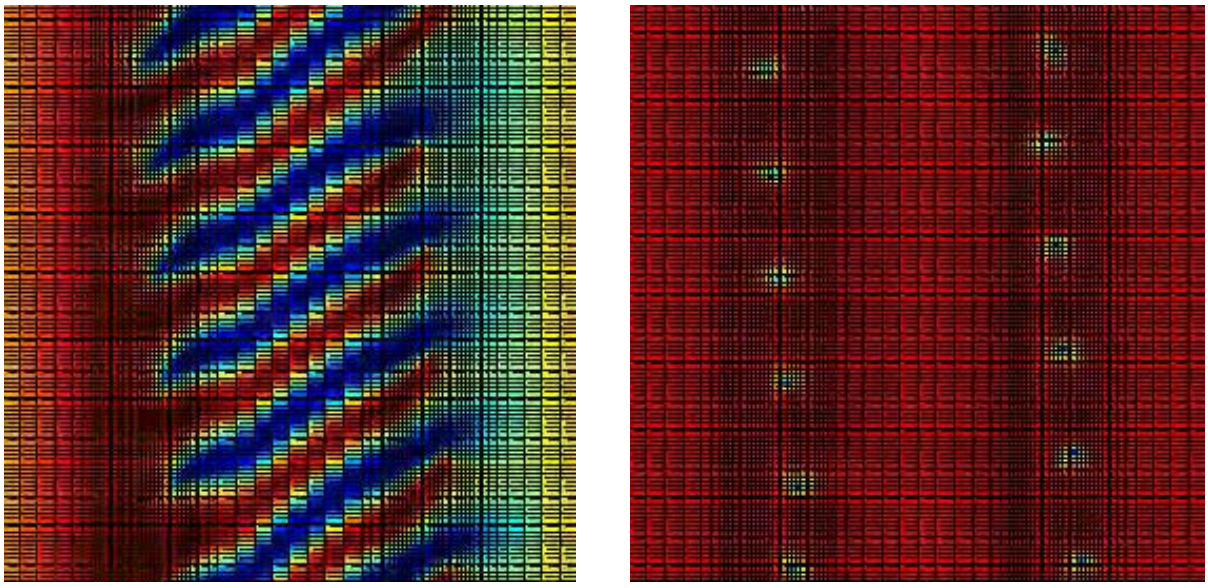

(a) $\Re(A_1)$ (b) $(|A_1| + |A_2| + |A_3|)/3$

Figure 5.6: A stationary 1-D non-uniform mesh with finer elements spread around grain boundaries, and coarse elements in the crystal bulk, illustrating the advantage of performing adaptive mesh refinement with the RG equations. The "dimples" in (b) are dislocations delineating grain boundaries. One still has to resolve the beats in misoriented grains however.

grid spacing in the y direction, $\Delta y = \pi/2$, and allowed Δx to vary from a minimum of $\pi/2$ near the grain boundaries to 2π in the interior of each crystal. This reduced the size of the computational mesh from 256×256 elements to 96×256 elements, for a domain size of 128π. We find that the speedup of the amplitude equations approach compared to the original PFC model is now close to a factor of *ten* (see Fig. 5.5), while the error in the free energy is still $< 1\%$. Although this is only a simple fixed and unidirectionally non-

uniform mesh, it shows the promise of adaptive mesh refinement (AMR) as a strategy for solving the amplitude equations, especially in view of our goal to make micro-scales accessible with the PFC model.

Fig. 5.6 also highlights an obstacle to progress with *complex* amplitude equations alone. Any mesh used to discretize these equations will also need to resolve the beats, which assume shorter and shorter wavelengths as the grains become more and more misoriented from $\mathbf{k}_j$. As suggested in section 3.4 the approach should be to evolve the amplitude modulus (which varies only near defects as shown in Fig. 5.6(b)) and phase (which varies sharply only near grain boundaries as shown in Fig. 3.6) variables instead of the real and imaginary components of the amplitude. We present an adaptive mesh algorithm based on this idea in the next chapter.

5.5 Simulations of two dimensional hetero-epitaxial growth and dislocation annihilation

Before concluding this chapter we report some interesting preliminary results from our attempts to simulate two dimensional hetero-epitaxial growth (described in section 3.3) with the complex amplitude equations.

Liquid phase epitaxial growth is simulated following Elder and Grant [28], who used a more general version of the PFC equation for this problem, viz.

$$\frac{\partial \psi}{\partial t} = \nabla^2 \left[\left\{ r + (k^2 + \nabla^2)^2 \right\} \psi + \psi^3 \right]. \tag{5.8}$$

A value of $k = k_0$ is chosen in the substrate region, a small part of the computational domain, while $k = k_1$ is used for the film. Clearly, patterns with different wavenumbers must emerge in each region. However, as the field ψ must remain continuous across the substrate/film interface, both the film and the substrate are elastically "strained" along the interface. As the substrate is typically modeled by only a few layers of atoms and is very close to its equilibrium configuration initially, it is very stiff and does not deform

very much, the wavenumber therefore remaining very close to k_0. On the other hand, the film is forced to have a wavenumber near k_0 at the interface and attempts to relax to k_1 away from the substrate by emitting misfit dislocations at regular height intervals. The magnitude of the strain is measured as $\epsilon = |a_1 - a_0|/a_0$, where a_1 and a_0 are the lattice spacings in the film and the substrate respectively. However in a 1-mode approximation to the crystal structure, $a \propto 1/k$, and therefore $\epsilon = |k_1 - k_0|/k_1$.

We simplify the above situation somewhat to suit our approach with amplitude equations. Instead of including both the substrate and film in our computational domain, we grow only the film, while imposing the mismatch strain due to the substrate, assumed to be a perfect crystal with wavenumber k_0, as a boundary condition on the complex amplitude along the bottom edge of the domain. The boundary conditions on the amplitude at the horizontal boundaries are therefore,

$$\begin{aligned} \text{Bottom Edge}: \ A_j &= \bar{A} e^{i(1-\frac{k_1}{k_0})\mathbf{k}_j \cdot \mathbf{x}} \\ \text{Top Edge}: \ A_j &= 0 \ \text{(liquid phase)}, \end{aligned} \tag{5.9}$$

while periodic boundary conditions are imposed on vertical boundaries. The basis vectors for the film are $(k_1/k_0)\mathbf{k}_j$, where $\mathbf{k}_j$ is given by Eq. (3.21), and therefore, the condition on the bottom edge guarantees continuity of the density field ψ between film and substrate. $\bar{A}$ is the equilibrium amplitude modulus of the substrate in a 1-mode approximation, determined by Elder and Grant [28] to be

$$\bar{A} = \frac{1}{5}\left(\bar{\psi} + \frac{1}{3}\sqrt{-15r - 36\bar{\psi}^2}\right). \tag{5.10}$$

Fig. 5.7 shows a time sequence in the evolution of a film with $k_1 = 1.05$, over a substrate with $k_0 = 1.0$, i.e. $\epsilon = 4.76\%$. The field plotted is the average amplitude modulus, $(|A|_1 + |A|_2 + |A|_3)/3$. Simulation parameters were $r = -0.25$, $\bar{\psi} = 0.285$, $\Delta x = 1.8138$, $\Delta t = 0.04$, $N_x = 401$, and $N_y = 201$, where N_x and N_y are respectively the number of grid points in the x and y directions on a uniform grid. As can be seen, the flat film eventually becomes unstable, nucleating misfit dislocations in waves above the

substrate. These dislocations climb towards the substrate, several of them annihilating each other, before finally leaving behind a low energy configuration.

Matthews and Blakeslee [107] have proposed a linear relationship of the form

$$\epsilon \propto \frac{\left[1 + \log_{10}\left(\frac{H_c}{a^*}\right)\right]}{\left(\frac{H_c}{a^*}\right)}, \tag{5.11}$$

where H_c is the height of the first wave of dislocations nucleated above the substrate, and a^* is the thickness of a film layer. Fig. 5.8 shows a least square fit of our numerical results with the functional form in Eq. (5.11), and the agreement is reasonably good.

Fig. 5.9 shows a zoomed-in time sequence of the dynamics of a dislocation pair that eventually annihilate one another. The field plotted is the reconstructed atomic density ψ, and the solid lines outline edge dislocations with opposite Burger's vectors. The distance between the dislocation cores $\delta(t)$ was measured as a function of the time to annihilation $t_a - t$, where t_a is the absolute time when the dislocations annihilate, and shows a power law scaling (also shown in Fig. 5.10)

$$\delta(t) = 1.22(t_a - t)^{0.49}. \tag{5.12}$$

This result appears to be consistent with a logarithmic interaction energy for a pair of isolated edge dislocations [108] in 2-D crystals, and a simple viscous glide model for dislocations. We illustrate this with a simple calculation. Let the interaction potential between the dislocation cores [108] be

$$V(\delta) = a - b\log(\frac{\delta}{a_c}), \tag{5.13}$$

where a and b are related to the elastic constants of the material and the dislocation core energy respectively. a_c is the dislocation core diameter. The tension along the line between the dislocations is therefore

$$T = \frac{dV(\delta)}{d\delta} = -\frac{ba_c}{\delta}. \tag{5.14}$$

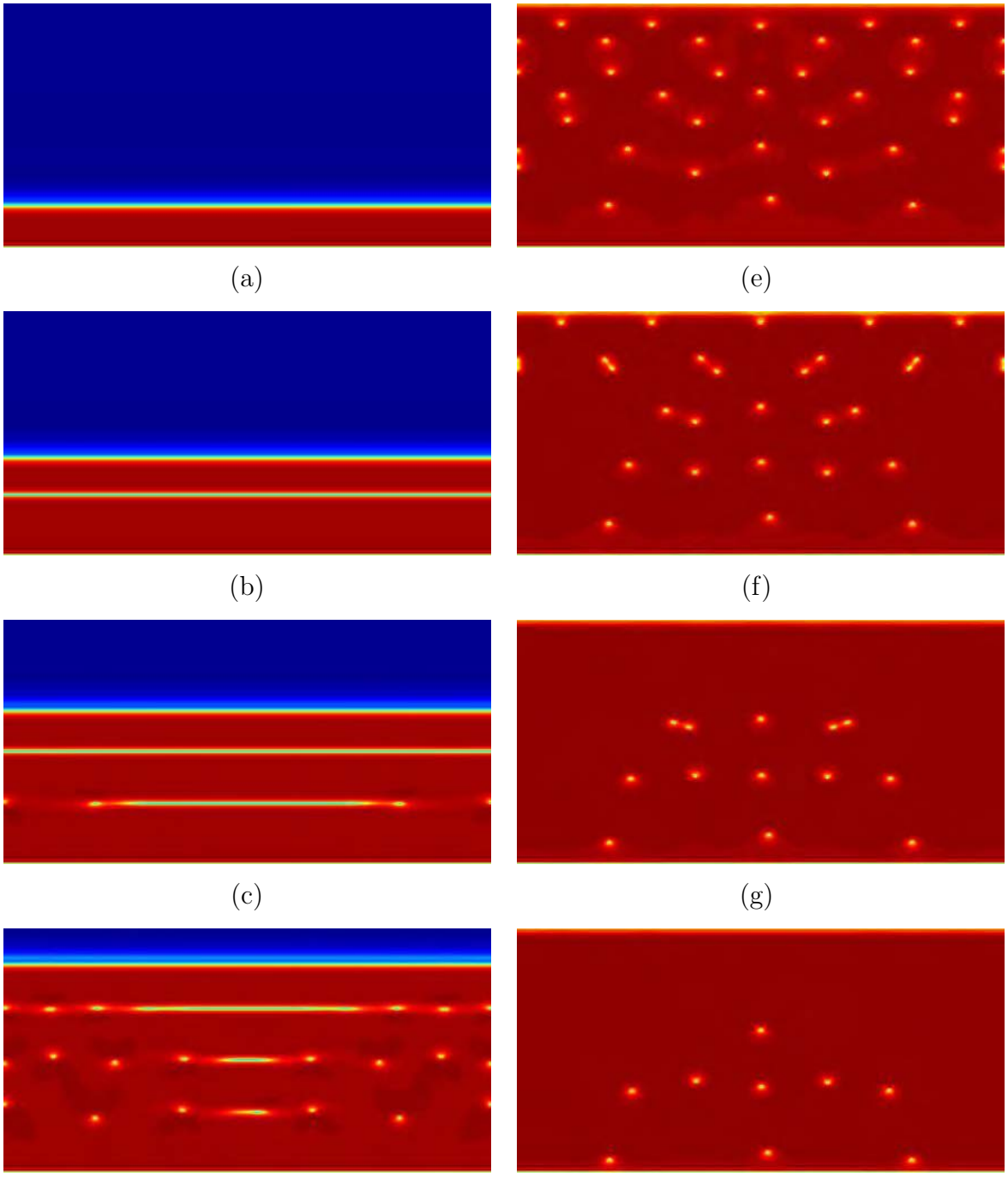

Figure 5.7: Time sequence showing liquid phase epitaxial growth of a thin film, simulated with the amplitude equations. The elastically strained film nucleates misfit dislocations at intervals above the substrate. Dislocations climb towards the substrate, several of them annihilating each other, leaving behind a relatively low energy dislocation network. The field plotted is the average amplitude modulus.

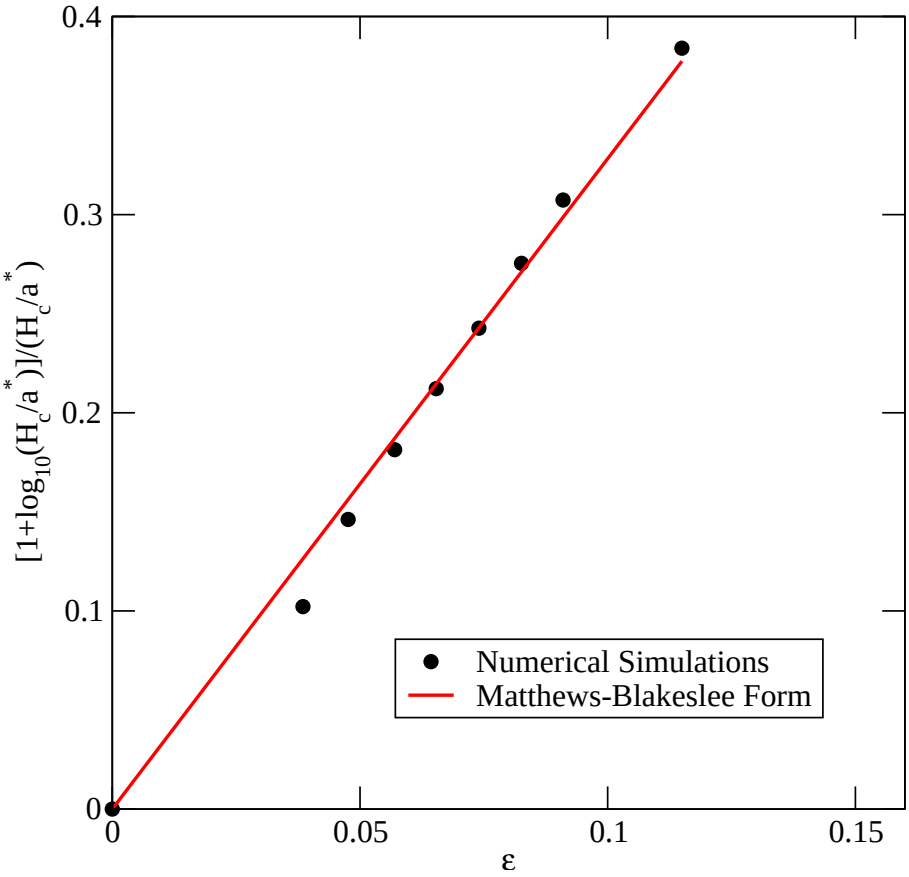

Figure 5.8: Comparison of critical nucleation height of misfit dislocations versus strain as predicted by numerical simulations of amplitude equations, with Matthews-Blakeslee theory.

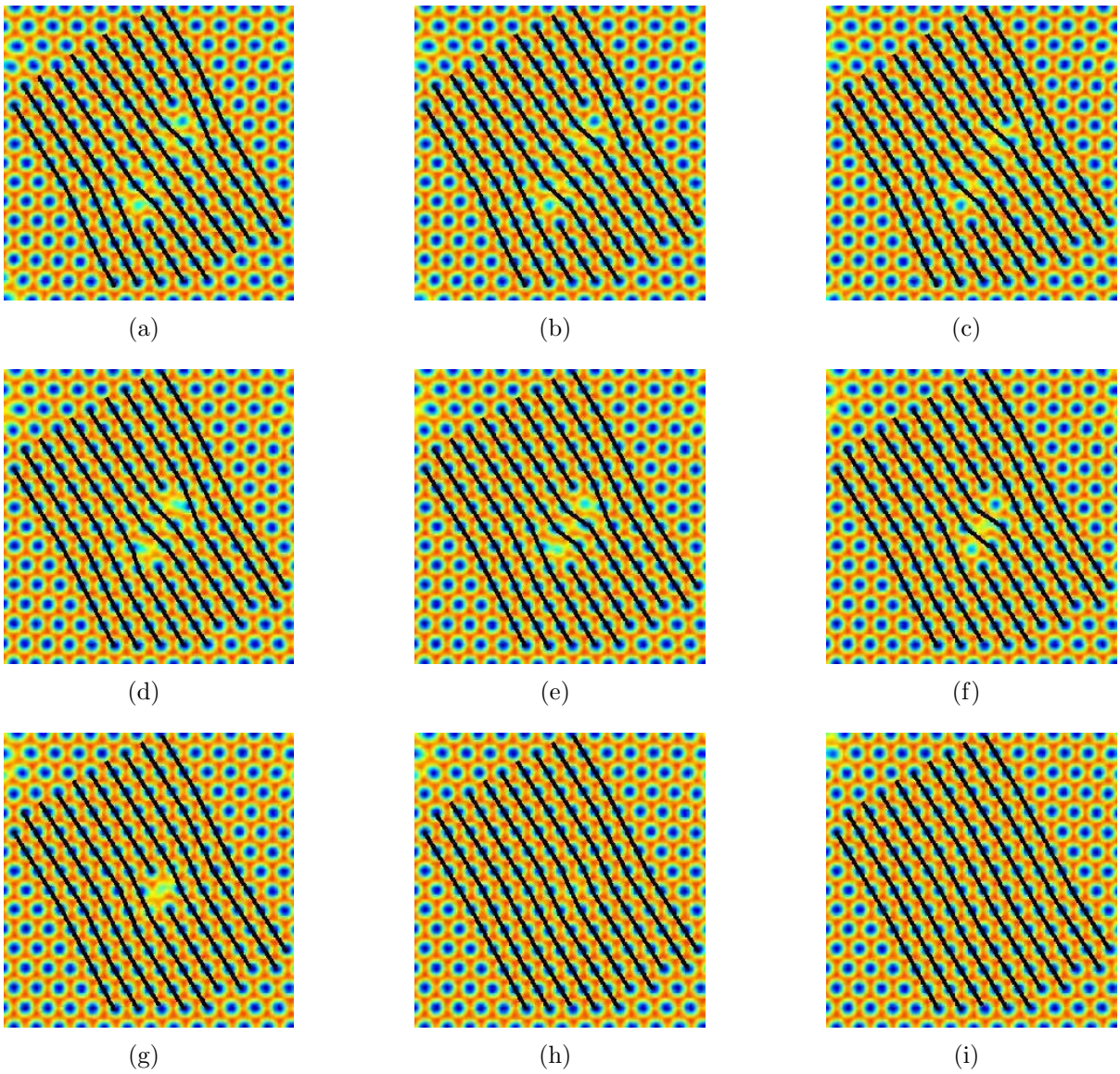

Figure 5.9: Reconstructed density field ψ during simulations of epitaxial film growth. The black lines outline two dislocations with opposite Burger's vectors, gliding towards one another and annihilating.

Viscous glide models assume that glide speeds are proportional to this tension, which implies that

$$\frac{d\delta}{dt} = \alpha T = -\frac{\alpha b a_c}{\delta} \tag{5.15}$$

where we α is some constant, and therefore

$$\delta^2 = -2\alpha b a_c t + I_1, \tag{5.16}$$

where I_1 is an integration constant. Since, $\delta = 0$ when $t = t_a$, i.e. when the dislocations annihilate, $I_1 = 2\alpha b a_c t_a$ and so we have

$$\delta(t) = \sqrt{2\alpha b a_c}(t_a - t)^{1/2}. \tag{5.17}$$

Ambrozic *et al.* [109] have observed a similar scaling during the annihilation of edge dislocations in liquid crystals.

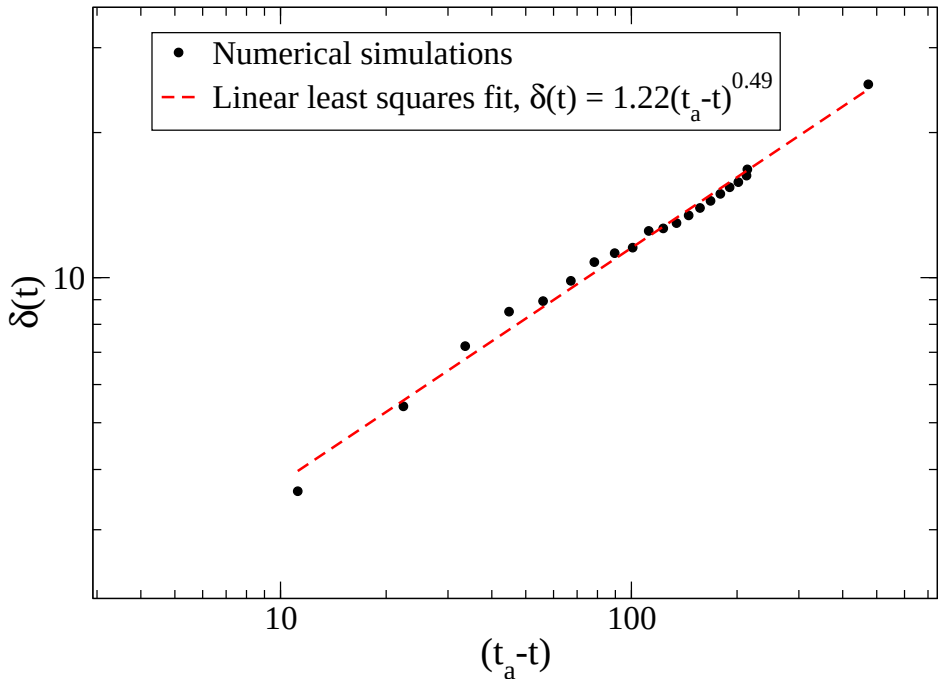

Figure 5.10: Power law scaling of inter-dislocation distance with time to annihilation, $t_a - t$, as calculated with the amplitude equations.

Chapter 6

Numerical Solution of Amplitude Equations on an Adaptive Grid

In this chapter we present a numerical algorithm for solving the amplitude equations in Eq. (5.1) on an adaptively evolving mesh. We demonstrate that with our formulation, it is possible to extend the modeling capabilities of the PFC equation to micro- length scales, once again with the example of 2-D nucleation and growth of polycrystals.

6.1 Complex amplitude equations on an adaptive grid using a cartesian representation

It must be evident from the last chapter, particularly from the discussion in section 5.4, that beats may limit the effectiveness of adaptive mesh refinement. We have verified that this is indeed the case. We simulated, yet again, the problem of heterogeneous nucleation and growth of a two-dimensional film, from twelve randomly oriented and placed crystals (the largest misorientation angle was $\theta = \pi/12$) each with an initial radius 8π, on a square domain of size 256π, but this time on an adaptively evolving mesh[1] with periodic boundary conditions. It is important to note that we solved for the real and imaginary

[1] A summary of the adaptive mesh refinement algorithm and criteria for refinement and coarsening will be given in a later section.

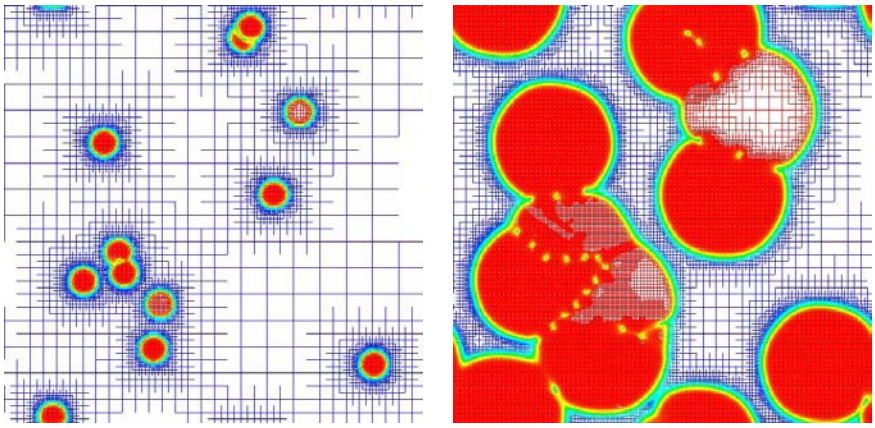

(a) $t = 0$

(d) $t = 248$

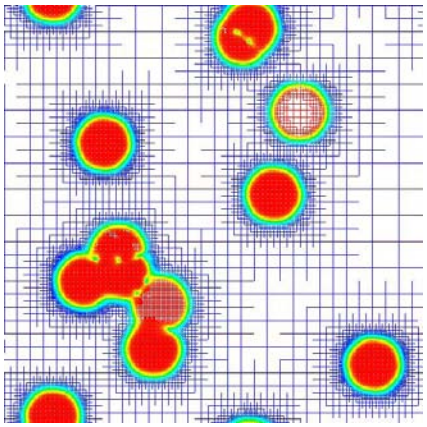

(b) $t = 88$

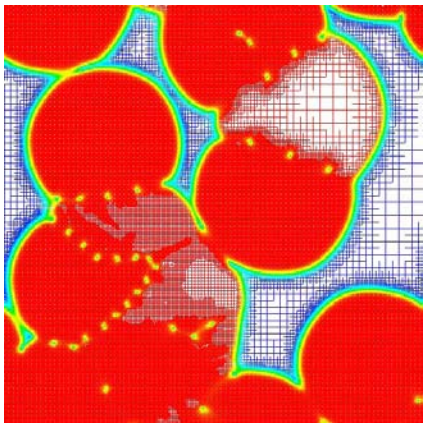

(e) $t = 320$

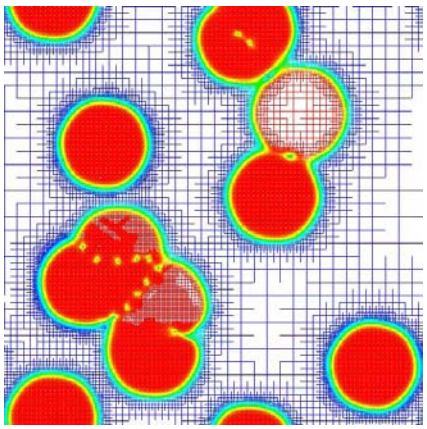

(c) $t = 168$

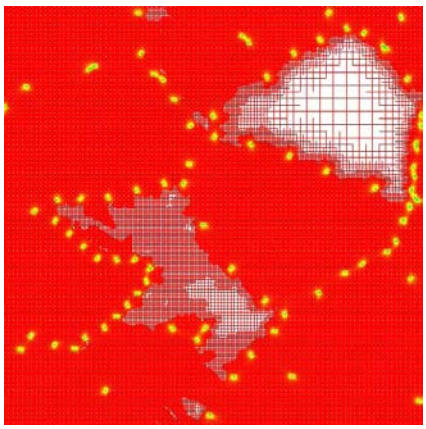

(f) $t = 552$

Figure 6.1: Evolution of a polycrystalline film simulated with complex amplitude equations, Eq. (5.1), on an adaptive grid. Note that the grid does not coarsen inside many of the grains (misoriented with respect to $\mathbf{k}_j$) because of the "beats" problem discussed in Sec. 5.2. The colored field plotted is the average amplitude modulus, which is "red" inside the crystal phase, "blue" in the liquid phase, "green" at the crystal/liquid interface, and "yellow" near defects.

parts of the A_j, which is what is implied by the *cartesian representation*. The simulation parameters were chosen to be $r = -0.25$ and $\bar{\psi} = 0.285$, the smallest mesh spacing was $\Delta x_{min} = \pi/2$, while the largest mesh spacing at any given time was $\Delta x_{max} = 2^4(\Delta x_{min})$ which provided 5 levels of refinement. On a uniform grid, this simulation would have required $1025 \times 1025 = 1,050,625$ nodes with the PFC equation, and $513 \times 513 = 263,169$ nodes with the amplitude equations. A time step of $\Delta t = 0.04$ was used.

Fig. 6.1 shows the crystal boundaries and grid structure[2] at various times during the simulation. Although the grid is quite coarse initially ($t = 0$ and $t = 88$), because of the large liquid fraction in the domain, this advantage falls off dramatically once the crystals evolve, collide, and start to form grain boundaries. In particular, once all the liquid freezes, only a couple of grains that are favorably oriented with respect to $\mathbf{k}_j$ show any kind of grid coarsening at all. The number of nodes in the adaptive grid corresponding to the polycrystal shown in Fig. 6.1(f) is $219,393$, which is very near that on a uniform grid, and therefore the adaptive refinement algorithm appears to be at best a marginal improvement over a fixed grid implementation.

6.2 Complex amplitude equations in a polar representation

Based on the properties of the solution, we anticipate that computational benefits with adaptive mesh refinement would be much higher if, instead of solving for the real and imaginary components of A_j, we solved for the amplitude moduli $\Psi_j = |A_j|$, and the phase angles $\Phi_j = \arctan(\Im(A_j)/\Re(A_j))$, which together constitute a *polar representation* of A_j. In this section we derive evolution equations for Ψ_j and Φ_j directly from Eq. (5.1), by applying Euler's formula for a complex number, i.e. $A_j = \Psi_j e^{i\Phi_j}$, and then by equating corresponding real and imaginary parts on the left hand sides and the right hand sides

[2]The graphics were rendered with software developed by Mike Greenwood and Nik Provatas at McMaster University.

of the resulting equations. In this manner we get the coupled system of equations,

$$\begin{aligned}\frac{\partial \Psi_j}{\partial t} &= (r+3\bar{\psi}^2)\left[-\Psi_j+\mathcal{C}^{\Re}(\Psi_j,\Phi_j)\right]-\left[\mathcal{C}^{\Re\Re}(\Psi_j,\Phi_j)-\mathcal{C}^{\Im\Im}(\Psi_j,\Phi_j)\right] \\ &\quad+\left[\mathcal{C}^{\Re\Re\Re}(\Psi_j,\Phi_j)-\mathcal{C}^{\Re\Im\Im}(\Psi_j,\Phi_j)-\mathcal{C}^{\Im\Im\Re}(\Psi_j,\Phi_j)-\mathcal{C}^{\Im\Re\Im}(\Psi_j,\Phi_j)\right] \\ &\quad-3\Psi_j\left(\Psi_j^2+2\sum_{k\neq j}\Psi_k^2\right)-6\frac{\bar{\psi}}{\Psi_j}\left(\prod_k\Psi_k\right)\cos\left(\sum_k\Phi_k\right) \end{aligned} \tag{6.1}$$

and

$$\begin{aligned}\frac{\partial \Phi_j}{\partial t} &= \left\{(r+3\bar{\psi}^2)\mathcal{C}^{\Im}(\Psi_j,\Phi_j)-\left[\mathcal{C}^{\Re\Im}(\Psi_j,\Phi_j)+\mathcal{C}^{\Im\Re}(\Psi_j,\Phi_j)\right]\right. \\ &\quad\left.+\left[\mathcal{C}^{\Im\Re\Re}(\Psi_j,\Phi_j)-\mathcal{C}^{\Im\Im\Im}(\Psi_j,\Phi_j)+\mathcal{C}^{\Re\Im\Re}(\Psi_j,\Phi_j)+\mathcal{C}^{\Re\Re\Im}(\Psi_j,\Phi_j)\right]\right\}/\Psi_j \\ &\quad+6\frac{\bar{\psi}}{\Psi_j^2}\left(\prod_k\Psi_k\right)\sin\left(\sum_k\Phi_k\right) \end{aligned} \tag{6.2}$$

where

$$\begin{aligned}\mathcal{C}^{\Re}(\Psi_j,\Phi_j) &= \Re\left\{\frac{\left[\nabla^2+2i\mathbf{k}_j\cdot\nabla\right](\Psi_j e^{i\Phi_j})}{e^{i\Phi_j}}\right\} \\ \mathcal{C}^{\Im}(\Psi_j,\Phi_j) &= \Im\left\{\frac{\left[\nabla^2+2i\mathbf{k}_j\cdot\nabla\right](\Psi_j e^{i\Phi_j})}{e^{i\Phi_j}}\right\} \\ \mathcal{C}^{\Re\Re}(\Psi_j,\Phi_j) &= \Re\left\{\frac{\left[\nabla^2+2i\mathbf{k}_j\cdot\nabla\right]\left(\mathcal{C}^{\Re}(\Psi_j,\Phi_j)e^{i\Phi_j}\right)}{e^{i\Phi_j}}\right\} \\ \mathcal{C}^{\Im\Re}(\Psi_j,\Phi_j) &= \Im\left\{\frac{\left[\nabla^2+2i\mathbf{k}_j\cdot\nabla\right]\left(\mathcal{C}^{\Re}(\Psi_j,\Phi_j)e^{i\Phi_j}\right)}{e^{i\Phi_j}}\right\}\end{aligned} \tag{6.3}$$

and so on. From here on we refer to the evolution equations for Ψ_j and Φ_j as the phase/amplitude equations, whereas Eq. (5.1) will be referred to as the complex amplitude equation. Unfortunately, the phase/amplitude equations in Eqs. (6.1) and (6.2) turn out to be quite difficult to solve globally. The principal difficulties are summarized below.

Ψ_j is practically constant within the individual grains and varies sharply only near grain boundaries, rendering its equation ideally suited for solution on adaptive meshes. Φ_j

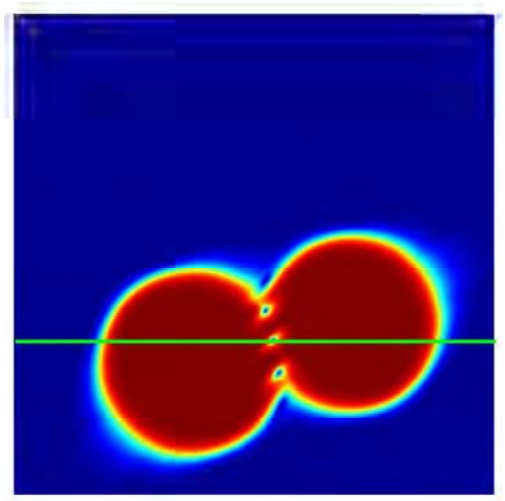

(a) Contours of Ψ_1.

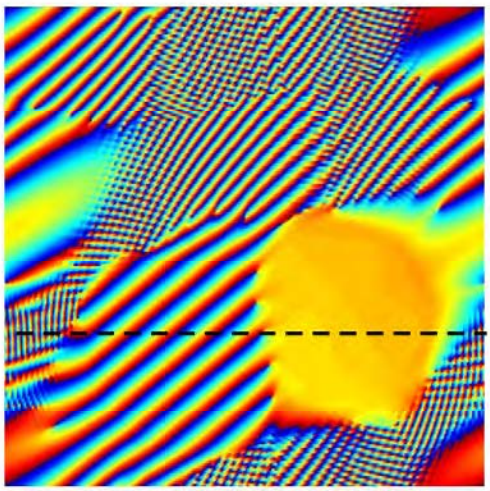

(c) Contours of Φ_1.

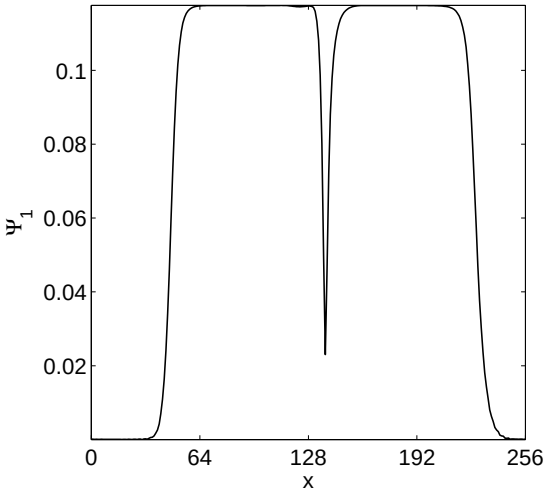

(b) Lineplot of Ψ_1 along solid line in (a).

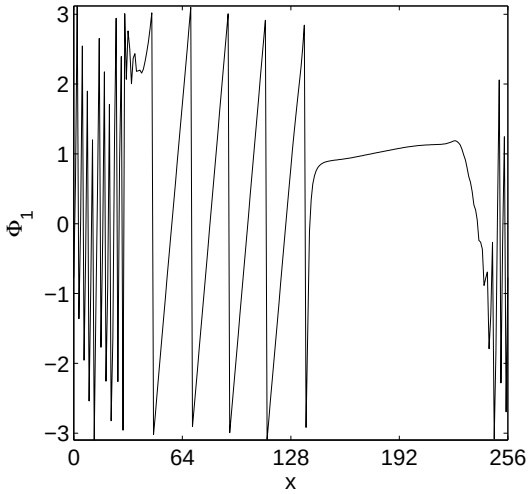

(d) Lineplot of Φ_1 along dashed line in (c).

Figure 6.2: While Ψ_1 is smooth everywhere except near interfaces and defects, Φ_1, which is computed naively as $\arctan(\Im(A_1)/\Re(A_1))$ is periodic and discontinuous. The chaotic fluctuations in (d) near the two ends corresponds to regions in the liquid phase where Φ_1 has no physical meaning. The rapid, but periodic, variations of Φ_1 in the left grain is due to its large misorientation angle of $\pi/6$. In contrast, the grain on the right is oriented along $\mathbf{k}_j$ causing Φ_1 to vary much more smoothly.

on the other hand, if computed naively as $\arctan(\Im(A_j)/\Re(A_j))$, is a periodic and discontinuous function[3] bound between the values $-\pi$ and π, with a frequency that increases with increasing grain misorientation. This poses a problem similar to that previously posed by the beats, with the grid this time having to resolve the fine scale structure of Φ_j. Further, one may need to resort to shock-capturing methods, such as ENO and WENO schemes [110, 111], in order to correctly evaluate higher order derivatives, and resolve jumps where Φ_j changes value from π to $-\pi$ and vice-versa. Complications are also caused by Φ_j being undefined in the liquid phase, and the tendency for Ψ_j, which appears in the denominator on the right hand side of Eq. (6.2), to approach zero at those locations. This calls for some type of robust regularization scheme[4] for the phase equations. These problems are clearly highlighted in Fig. 6.2, which shows the impingement of two misaligned crystals.

Ideally, one would like to reconstruct from the periodic Φ_j, a continuous surface $\Phi_j + 2n\pi$ (where n is an integer) which would be devoid of jumps, and therefore amenable to straightforward resolution on adaptive meshes. The implementation of such a reconstruction algorithm however, even if possible, requires information about individual crystal orientations, and the precise location of solid/liquid interfaces, defects, and grain boundaries at every time step, making it very computationally intensive. Further, such an algorithm would be more appropriate in the framework of an interface-tracking approach such as the level set method [112], rather than our phase-field modeling approach.

Despite these issues with the phase/amplitude equations, progress can be made via certain assumptions, and by recognizing that these equations can be solved locally in conjunction with the complex amplitude equations.

[3] $\Phi_j \approx \mathbf{q}(\theta) \cdot \mathbf{x}$, $\Phi_j \in [-\pi, \pi]$, where $\mathbf{q}(\theta)$ is the phase vector, constant for a particular orientation of the grain, and θ is the misorientation angle of the grain. Thus Φ_j, roughly speaking, has the structure of a sawtooth waveform.

[4] We have determined that simple tricks such as setting Ψ_j to some small non-zero value, or setting a heuristic upper bound on higher-order derivatives, have the effect of destroying defects and other topological features in the pattern.

6.3 Reduced equations and frozen phase gradients

The main idea that will be developed in this and subsequent sections is that of evolving the phase/amplitude and complex amplitude equations simultaneously in different parts of the domain, depending on where they can most appropriately be applied. Based on the discussion in the previous section, it is clear that the phase/amplitude formulation is best suited for numerical solution in the crystal bulk, away from defects, interfacial regions, and the liquid phase. This does away with the need for regularizing the phase equations where $\Psi_j \to 0$, as $\Psi_j \gg 0$ in the crystal interior, and the other issue of the phase being undefined in certain regions. The complex amplitude equations can be solved everywhere else in the computational domain. We overcome the remaining issues with the phase equation, viz. the difficulty of evaluating derivatives of the phase and the need to resolve its periodic variations via certain controlled approximations described below.

Our uniform grid calculations with the complex amplitude equations indicate that the functions Ψ_j and $\nabla\Phi_j$ contain negligible gradients inside crystals as compared to interfaces and defects. This can be seen from Figs. 6.2(b) and 6.3(b) which show one dimensional variations of Ψ_j and one of the components of $\nabla\Phi_j$ through cross-sectional plots of two impinging misoriented crystals. These plots were generated by processing the real and imaginary component fields of A_j. In fact, the uniform nature of these variables can be inferred even from the filled contour plots in Figs. 6.2(a) and 6.3(a).

Based on the above observations, we neglect third and higher order derivatives of Ψ_j and Φ_j [5], which allows us to simplify Eqs. (6.1) and (6.2) to the following second order PDEs

$$\begin{aligned}
\frac{\partial \Psi_j}{\partial t} &= (r + 3\bar{\psi}^2)\left[-\Psi_j + \mathcal{C}^{\Re}(\Psi_j, \Phi_j)\right] \\
&\quad -3\Psi_j\left(\Psi_j^2 + 2\sum_{k\neq j}\Psi_k^2\right) - 6\frac{\bar{\psi}}{\Psi_j}\left(\prod_k \Psi_k\right)\cos\left(\sum_k \Phi_k\right) \qquad (6.4)\\
\frac{\partial \Phi_j}{\partial t} &= \frac{(r + 3\bar{\psi}^2)\mathcal{C}^{\Im}(\Psi_j, \Phi_j)}{\Psi_j} + 6\frac{\bar{\psi}}{\Psi_j^2}\left(\prod_k \Psi_k\right)\sin\left(\sum_k \Phi_k\right), \qquad (6.5)
\end{aligned}$$

[5] To consistent order, we can also neglect second order derivatives of Ψ_j.

where $\mathcal{C}^{\Re}$ and $\mathcal{C}^{\Im}$ contain only first and second order derivatives in Ψ_j and Φ_j. The task of evolving the phase/amplitude equations is now considerably simplified, as only derivatives up to second order in Φ_j need to be computed. While the gradient and Laplacian of Ψ_j can be computed in the usual manner using Eqs. (B.5) and (B.1), the gradient of Φ_j needs to be computed with a little more care (in order to avoid performing derivative operations on a discontinuous function).

$$\begin{aligned}
\because \tan\Phi_j &= \frac{\Im(A_j)}{\Re(A_j)} \\
\implies \sec^2\Phi_j \nabla\Phi_j &= \frac{\Re(A_j)\nabla\Im(A_j) - \Im(A_j)\nabla\Re(A_j)}{\Re(A_j)^2} \\
\implies \left(1 + \frac{\Im(A_j)^2}{\Re(A_j)^2}\right)\nabla\Phi_j &= \frac{\Re(A_j)\nabla\Im(A_j) - \Im(A_j)\nabla\Re(A_j)}{\Re(A_j)^2} \\
\implies \nabla\Phi_j &= \frac{\Re(A_j)\nabla\Im(A_j) - \Im(A_j)\nabla\Re(A_j)}{\Psi_j^2}.
\end{aligned} \tag{6.6}$$

Thus, the gradient operation on a discontinuous function Φ_j is now transformed into gradient operations on the smooth components of the complex amplitude A_j. Further, $\nabla^2\Phi_j$ is computed as $\nabla \cdot \nabla\Phi_j$, where the divergence operator is discretized using a simple second order centered difference scheme. Eqs. (6.4) and (6.5) are the reduced phase/amplitude equations.

However, as can be seen from Eq. (6.6), $\nabla\Phi_j$ now depends on gradients of the real and imaginary components of A_j, which may not be properly resolved in the crystal bulk as we intend to coarsen the mesh there. To address this point, we assume that $\nabla\Phi_j$ is frozen temporally in the crystal bulk. This assumption implies that once $\nabla\Phi_j$ is accurately initialized in the crystal interior via Eq. (6.6), after ensuring adequate resolution of the components of A_j, it need not be computed again. For example, in simulations of crystal growth from seeds, we can start with a mesh that is initially completely refined inside the seeds, so that $\nabla\Phi_j$ is correctly computed. Once initial transients disappear and the crystals reach steady state evolution, the growth is monotonic in the outward direction. From this point on, $\nabla\Phi_j$ hardly changes inside the crystal bulk (see next paragraph),

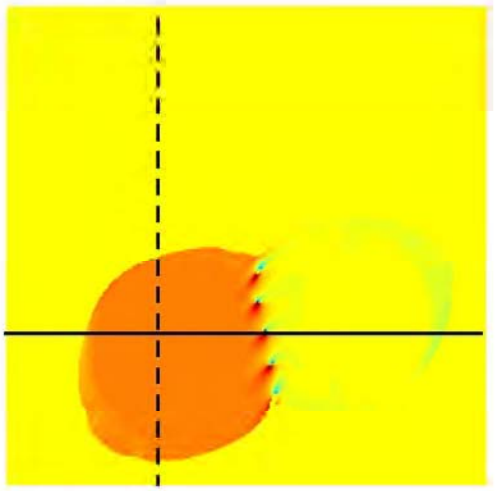

(a) Contours of $\partial\Phi_1/\partial x$.

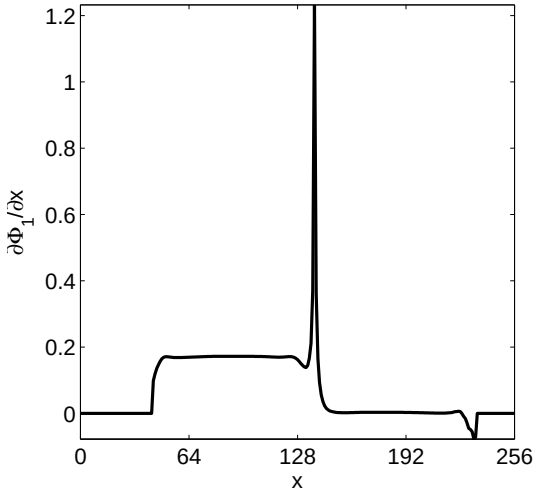

(b) Lineplot of $\partial\Phi_1/\partial x$ along solid line in (a).

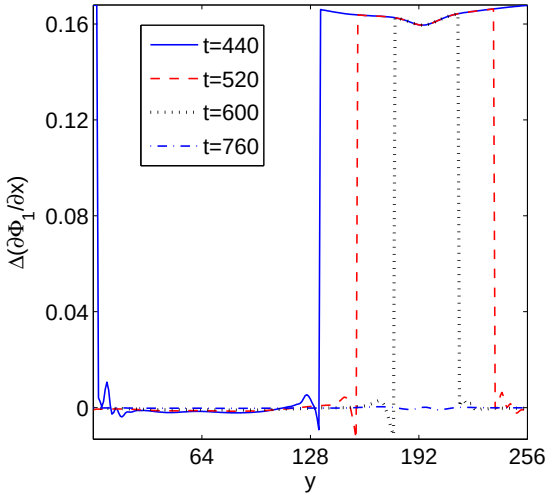

(c) $\Delta(\partial\Phi_1/\partial x)$ along dashed line in (a).

Figure 6.3: Note that this is the same pair of crystals shown in Fig. 6.2. Like Ψ_j, the components of $\nabla\Phi_j$ are also practically constant inside the individual crystals. The spike in (b) corresponds to a defect on the grain boundary. As seen from the time series in (c) for $\partial\Phi_1/\partial x$, $\nabla\Phi_j$ hardly changes in the crystal bulk during its evolution.

and the grid can unrefine inside the grains while correctly resolving gradients in $\nabla\Phi_j$. Note that the apparent discontinuities in Φ_j no longer need be resolved by the grid.

We justify the above approximation of a *locally frozen phase gradient*[6], once again via a fixed grid calculation with the complex amplitude equations, where $\nabla\Phi_j$ inside a steady growing crystal is seen to be essentially time invariant. Fig. 6.3(c) shows a sequence of line plots of the quantity $\Delta(\partial\Phi_1/\partial x) = \partial\Phi_1/\partial x|_{t=840} - \partial\Phi_1/\partial x|_t$, which illustrates the difference between the x component of $\nabla\Phi_1$ at time $t = 840$ and indicated times along the dashed line in Fig. 6.3(a). As the crystal on the left grows (as t increases), it can be seen that $\Delta(\partial\Phi_1/\partial x)$ stays close to zero inside. We have verified that this is also true for the y component of $\nabla\Phi_1$, and both components of $\nabla\Phi_2$ and $\nabla\Phi_3$.

$\nabla\Phi_j$ is a quantity that measures crystal orientation. An assumption that the orientation of a freely evolving crystal does not change with time therefore seems perfectly reasonable. On the other hand, when similarly oriented crystals collide to form a small angle grain boundary, the situation turns out to be more energetically favorable for grains to realign (i.e. $\nabla\Phi_j$ changes inside the grains, close to the grain boundary) locally in order to reduce orientational mismatch [113–116], rather than nucleate dislocations. Fortunately, as such interaction effects originate at the grain boundary, where the full complex equations will be solved, we anticipate that our assumption will not lead to artificially "stiff" grains.

6.4 Domain decomposition

In order to implement our idea of evolving Eq. (5.1), and Eqs. (6.4) and (6.5) selectively, we start by dividing the computational domain into two regions where each set of equations may be evolved simultaneously in a stable fashion. We term the region where A_j is computed X, and the region where Ψ_j and Φ_j are computed Y. It is worth ensuring that subdomain Y is well separated from locations with sharp gradients, such as inter-

[6]Note that the assumption of a frozen phase gradient does not mean that Φ_j itself cannot change. Φ_j can continue to evolve as per Eq. (6.5) under the constraint of a fixed $\nabla\Phi_j$, although the changes may actually be quite small.

faces and defects. Otherwise, errors resulting from our approximations may grow rapidly, causing X to invade Y, which will in turn require us to solve the complex equations everywhere. We will further assume that the decomposition algorithm is implemented after a sufficient time, when initial transients have passed, and that the crystals are evolving steadily, which implies that Ψ_j inside the crystals has reached some maximum saturation value Ψ_j^{max}. The scenario we have in mind is sketched in Fig. 6.4, with Y constituting the shaded regions and everything else being X.

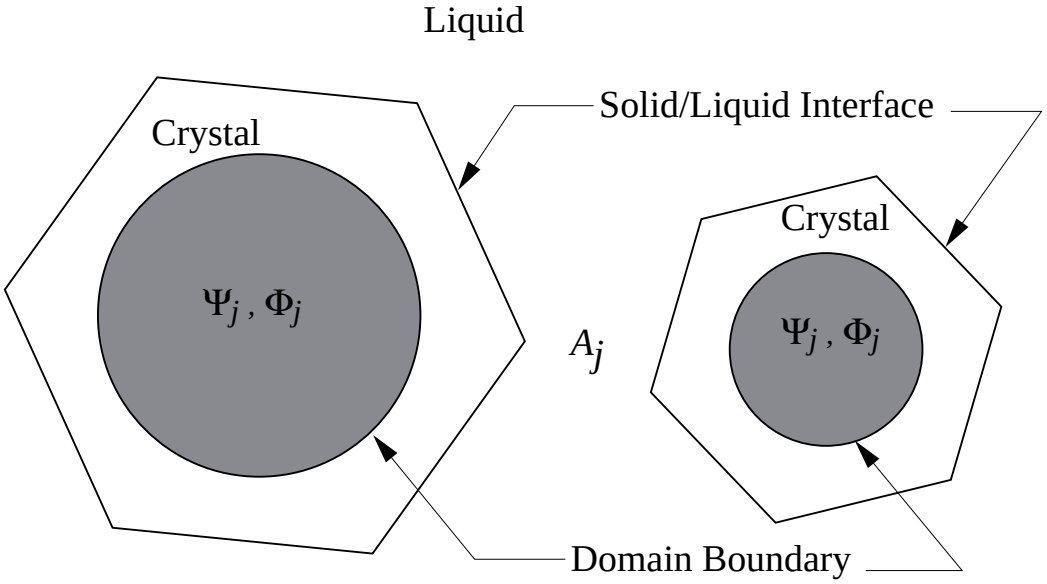

Figure 6.4: Sketch illustrating the idea of selectively evolving the complex amplitude and phase/amplitude equations in different parts of the computational domain. Ψ_j and Φ_j are evolved inside the shaded circles that fall well inside the crystalline phase, while the real and imaginary components of A_j are evolved elsewhere.

The pseudo-code shown in **Algorithm 1** presents a simple algorithm to achieve this decomposition. The algorithm first determines nodes with Ψ_j exceeding some minimum value $\gamma\Psi_j^{max}$, and $|\nabla\Psi_j|$ beneath some limit ϵ_1. The nodes satisfying these conditions constitute domain Y, while those failing to, constitute X. The Y nodes are then checked again to see if the quantity $|\nabla(|\nabla\Phi_j|)|$ is under some limit ϵ_2. Nodes in set Y that fail to satisfy this condition are placed in set X. The parameters γ, ϵ_1, and ϵ_2 are chosen optimally, to ensure the largest possible size of set Y. A small problem is caused by the

fields Ψ_j and $|\nabla\Phi_j|$ not being perfectly monotonic. As the limits ϵ_1 and ϵ_2 are sharp, several small islands (clusters of grid points) of X or Y can be produced, which are detrimental to numerical stability. We have resolved this issue via a coarsening algorithm that eliminates very small clusters of X and Y.

Algorithm 1 Domain decomposition. The parameters γ, ϵ_1, and ϵ_2 are heuristic.

```
Compute Ψ_j^max
Ψ_j^max = γ × Ψ_j^max
{Split domain based on the magnitude of Ψ_j and |∇Ψ_j|}
for i = 1 to maxnode do {loop over all nodes}
  count = 0
  for j = 1 to 3 do {loop over amplitude components}
    if Ψ_j ≥ Ψ_j^max and |∇Ψ_j| ≤ ε_1 then
      count++
    end if
  end for
  if count = 3 then
    domain = Y {passed test, solve phase/amplitude equations}
  else
    domain = X {failed test, solve complex equations}
  end if
end for
{Split domain based on |∇(|∇Φ_j|)|}
for i = 1 to maxnode do {loop over all nodes}
  count = 0
  if domain = Y then {check only nodes that passed previous test}
    for j = 1 to 3 do {loop over amplitude components}
      if |∇(|∇Φ_j|)| ≤ ε_2 then
        count++
      end if
    end for
    if count ≠ 3 then
      domain = X {failed test, solve complex equations}
    end if
  end if
end for
```

Fig. 6.5 shows results from a uniform grid implementation of **Algorithm 1**. No islands are present, and the algorithm appears to do a nice job of decomposing the domain in an unsupervised manner. Notice how the domain boundaries distort in Figs. 6.5(c) and

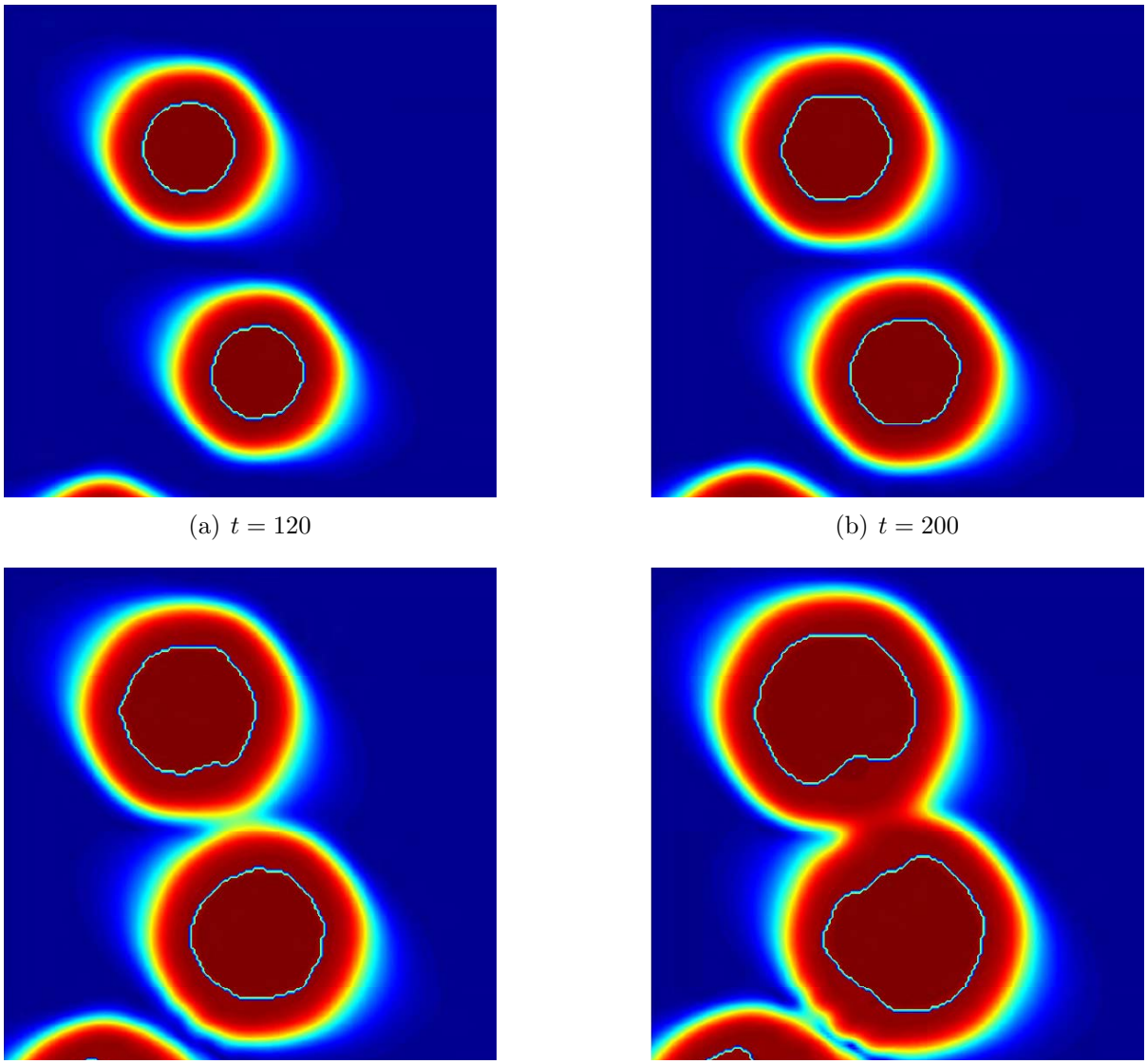

(a) $t = 120$ (b) $t = 200$

(c) $t = 280$ (d) $t = 360$

Figure 6.5: Filled contour plot showing the time evolution of three misoriented crystals. The field plotted is Ψ_3. Superimposed on the plot as solid curves are the boundaries that separate domains X and Y, with Y being enclosed by the curves.

6.5(d) in response to the formation of a grain boundary between the two crystals, after being roughly hexagonal at earlier times. The fact that the domain separatrices maintain a safe distance from the grain boundary ensures that the phase/amplitude equations are not evolved in regions with sharp gradients in $\nabla\Phi_j$. Parameter values used were $\gamma = 0.85$, $\epsilon_1 = 0.0005$, and $\epsilon_2 = 0.003$.

The beauty of this numerical scheme is that solving different sets of equations in X and Y does not call for doing anything special near the domain boundaries, such as creating "ghost" nodes outside each domain, or constraining solutions to match at the boundaries. Both sets of variables, $\{\Psi_j, \Phi_j\}$ and $\{A_j\}$, are maintained at all grid points irrespective of the domain they belong to, with one set allowing easy computation of the other[7]. Therefore the transition between the two domains is a continuous one in terms of field variables, which allows the finite difference stencils in Eqs. (B.1) and (B.5) to be applied to the respective fields without any modification near domain boundaries.

6.5 Adaptive mesh refinement (AMR)

We have built a numerical implementation of our equations on a finite difference adaptive grid module developed by Greenwood and Provatas [117] for phase-field models of solidification. We refer the interested reader to their work for full implementation details of the AMR algorithm and refinement/unrefinement procedures while providing only a gist here.

The adaptive grid module uses a quadtree data structure [118] to store information pertaining to elements, their nodes, nodal connectivity, and element neighbors. Elements with different refinement levels occupy different levels in the tree, with the depth of the tree being equal to the total number of refinement levels. Starting at the root of the tree, if an element, which is a leaf of the tree, satisfies some criterion and needs to be split, it is quadrisected into four smaller elements (four new leaves) which preserve memory of the parent node. Similarly, starting from the leaves of the tree, if elements belonging to

[7]For example in domain X where $\{A_j\}$ is the field variable, $\Psi_j = |A_j|$ and $\Phi_j = \Im(A_j)/\Re(A_j)$, whereas in domain Y where $\{\Psi_j, \Phi_j\}$ are the field variables, $\Re(A_j) = \Psi_j \cos(\Phi_j)$ and $\Im(A_j) = \Psi_j \sin(\Phi_j)$.

the same parent are not to be split, they are merged. The tree is recursively searched for elements that satisfy criteria for refinement/coarsening. An important rule associated with the AMR algorithm is that any two elements sharing a node cannot differ by more than one level of refinement[8]. For this reason, before an element is split, its neighbors are checked to see if they satisfy the one-level rule [19]. If not, they are split as well. A nodal linked list, which stores nodal variables and node neighbor information is also present. Although finite difference methods use a nodal representation of the grid, the element representation is more convenient from the point of view of AMR. The idea of using dynamic data structures such as quadtrees and octrees for AMR goes back to Shephard and co-workers for their work on unstructured finite element mesh generation [119–121] through the 1980s.

We now focus on two aspects of the AMR algorithm that we have had to modify to suit our equations.

6.5.1 Handling of ghost nodes

A nice feature of the AMR implementation in [117] is that each node sits at the center of a uniform 5×5 mini-grid. This is illustrated in Fig. 6.6, where the node represented by the lightly shaded circle (labeled F), has access to all other nodes on the wireframe. The advantage of this is that it allows us to use the uniform grid finite difference stencils for the Laplacian and gradient operators in Eqs. (B.1) and (B.5) respectively, instead of modifying them node-wise to accommodate variations in grid spacing. However, "ghost" nodes now have to be introduced. These nodes, which are shown as dark shaded circles in Fig. 6.6 are non-computational in nature, primarily serving to store field values interpolated from neighboring nodes, which are subsequently used for computing derivatives at the computational nodes (open circles in Fig. 6.6). A similar situation arises in finite element based AMR implementations [19,122] where "hanging" or "disconnected" nodes need to be introduced when the refinement level changes between two adjoining elements.

[8]Described as the one-level rule in [19].

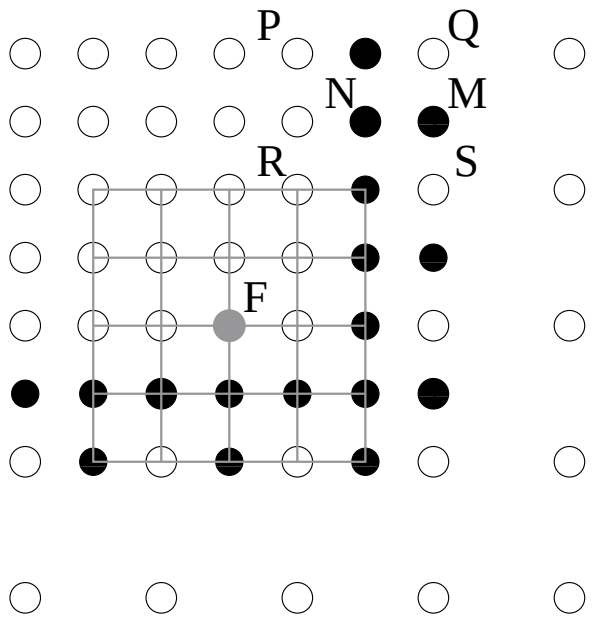

Figure 6.6: Schematic showing a portion of the adaptive grid where the refinement level changes. Open circles (and node F) are real nodes where the fields are computed, whereas the rest are non-computational ghost nodes where the fields need to be interpolated.

The scheme used to interpolate values at the ghost nodes is an important source of error in the numerical solution, and must be chosen carefully to ensure that the error remains bounded. Ψ_j, $\partial\Phi_j/\partial x$, $\partial\Phi_j/\partial y$, $\Re(A_j)$ and $\Im(A_j)$ are very smoothly varying functions, and therefore we *linearly* interpolate their values to the ghost nodes. Values at ghosts residing on element[9] edges, for example node M in Fig. 6.6, are obtained by averaging values of the two end nodes Q and S, whereas values at ghosts residing at the center of an element, node N for example, are obtained by averaging the values at the four corner nodes, P, Q, R, and S. We have found this interpolation scheme to be quite stable. We note however that, given the near-periodic variations in $\Re(A_j)$ and $\Im(A_j)$, especially in misoriented grains, higher order interpolation functions (such as cubic splines) will certainly improve accuracy of solutions, while strongly enforcing continuity of fields across elements. We leave that as a small area for future work.

[9]We define an element as a square with real corner nodes.

The interpolation of Φ_j at the ghost nodes is a little more tricky. Since Φ_j is a discontinuous function, a simple average of the values at the neighboring real nodes may not always give the correct answer, especially if the grid does not resolve the discontinuities (which it does not). Even if it does, a simple average can lead to the wrong result. As a case in point, consider the two real nodes Q and S in Fig. 6.6, with values $\Phi_1^Q = \pi - \delta_1$ and $\Phi_1^S = -\pi + \delta_2$ where δ_1 and δ_2 are very small but positive real numbers, on either side of a discontinuity in Φ_1. We wish to determine the value at the ghost node M, that lies between Q and S. Although the values of Φ_1 at Q and S are essentially equivalent in phase space, differing in magnitude by $\approx 2\pi$, a simple average gives $\Phi_1^M = (\delta_2 - \delta_1)/2 \approx 0$, which is quite wrong.

In order to interpolate correctly we need to make use of $\nabla\Phi_j$. For example in the above case, the total change in the phase from Q to S is obtained by integrating the directional derivative of Φ_1 along the edge QS, i.e.

$$\Delta\Phi_1^{QS} = \int_Q^S \nabla\Phi_1 \cdot d\mathbf{r} = \int_{y=y^Q}^{y^S} \frac{\partial\Phi_1}{\partial y} dy. \tag{6.7}$$

Eq. (6.7) can be evaluated numerically, and the accuracy of the result depends on how well $\partial\Phi_1/\partial y$ is approximated. Consistent with our earlier assumptions, we approximate $\partial\Phi_1/\partial y$ as piecewise constant where

$$\frac{\partial\Phi_1}{\partial y} = \frac{1}{2}\left(\left.\frac{\partial\Phi_1}{\partial y}\right|_S + \left.\frac{\partial\Phi_1}{\partial y}\right|_Q \right) \tag{6.8}$$

which leads to

$$\Delta\Phi_1^{QS} = \frac{1}{2}\left(\left.\frac{\partial\Phi_1}{\partial y}\right|_S + \left.\frac{\partial\Phi_1}{\partial y}\right|_Q \right)\left(y^S - y^Q\right). \tag{6.9}$$

Since $\partial\Phi_1/\partial y$ is constant along the edge QS, Φ_1 must vary linearly along QS. Hence at node M,

$$\Phi_1^M = \Phi_1^S + \frac{1}{2}\Delta\Phi_1^{QS} \ : \ \Phi_1^M \in [-\pi, \pi]. \tag{6.10}$$

Interpolation of Φ_j at element center ghost nodes, such as N, is done in a similar manner by interpolating linearly from ghost nodes at the centers of opposite element edges. Once

again, this scheme can be improved by choosing higher order polynomials to approximate $\nabla\Phi_j$ inside elements.

6.5.2 Refinement criteria

Traditionally, AMR algorithms rely on some kind of local error estimation procedure to provide a criterion for grid refinement. Years ago, Zienkiewicz and Zhu [123] developed a simple scheme for finite element discretization of elliptic and parabolic PDEs by computing the error in the gradients of the fields using higher order interpolation functions. Berger and Oliger [124] on the other hand estimated the local truncation error of their finite difference discretization of hyperbolic PDEs via Richardson extrapolation. As it turns out, depending on the equations being solved and the numerical methods being used, one scheme may work more effectively than another. We use a very simple and computationally inexpensive refinement criterion [117] that works rather nicely for our equations, based purely on gradients in the various fields. The outline of an algorithm to decide whether or not to split an element is given in **Algorithm 2**. **Algorithm 1** needs to be called first in order to split the computational domain into subdomains X and Y.

The routine initially computes absolute changes in the real and imaginary parts of A_j, and the x and y components of $\nabla\Phi_j$, in the element. We use absolute differences in place of derivatives in order for the refinement criterion to be independent of element size.

First, an element flag is checked to see if the element lies on the separatrix between X and Y, or within the Y subdomain, k layers from the boundary. If it does, this element is split. This ensures that the fields are always resolved on the interface between X and Y, and just within the boundary on the Y side. The latter is required because of the higher order derivative operations that need to be performed while evolving the complex amplitude equations in X.

If the element does not split and belongs to X where A_j are the field variables, the variations in the real and imaginary parts of A_j are checked to see if they exceed a certain bound ϵ_1. If any one of them does, this element is split. If on the other hand, the element

Algorithm 2 Criteria for element splitting

{N1, N2, N3 and N4 are the element nodes in clockwise manner}
for i = 1 to 3 **do** {loop over amplitude components}
{Change in real part of A_i over element}
$DR_i = |\text{N1} \rightarrow \Re(A_i) - \text{N2} \rightarrow \Re(A_i)| + |\text{N2} \rightarrow \Re(A_i) - \text{N3} \rightarrow \Re(A_i)|$
$+|\text{N3} \rightarrow \Re(A_i) - \text{N4} \rightarrow \Re(A_i)| + |\text{N4} \rightarrow \Re(A_i) - \text{N1} \rightarrow \Re(A_i)|$
{Change in imaginary part of A_i over element}
$DI_i = |\text{N1} \rightarrow \Im(A_i) - \text{N2} \rightarrow \Im(A_i)| + |\text{N2} \rightarrow \Im(A_i) - \text{N3} \rightarrow \Im(A_i)|$
$+|\text{N3} \rightarrow \Im(A_i) - \text{N4} \rightarrow \Im(A_i)| + |\text{N4} \rightarrow \Im(A_i) - \text{N1} \rightarrow \Im(A_i)|$
{Change in x component of $\nabla\Phi_i$ over element}
$DGPX_i = |\text{N1} \rightarrow \partial\Phi_1/\partial x - \text{N2} \rightarrow \partial\Phi_1/\partial x| + |\text{N2} \rightarrow \partial\Phi_1/\partial x - \text{N3} \rightarrow \partial\Phi_1/\partial x|$
$+|\text{N3} \rightarrow \partial\Phi_1/\partial x - \text{N4} \rightarrow \partial\Phi_1/\partial x| + |\text{N4} \rightarrow \partial\Phi_1/\partial x - \text{N1} \rightarrow \partial\Phi_1/\partial x|$
{Change in y component of $\nabla\Phi_i$ over element}
$DGPY_i = |\text{N1} \rightarrow \partial\Phi_1/\partial y - \text{N2} \rightarrow \partial\Phi_1/\partial y| + |\text{N2} \rightarrow \partial\Phi_1/\partial y - \text{N3} \rightarrow \partial\Phi_1/\partial y|$
$+|\text{N3} \rightarrow \partial\Phi_1/\partial y - \text{N4} \rightarrow \partial\Phi_1/\partial y| + |\text{N4} \rightarrow \partial\Phi_1/\partial y - \text{N1} \rightarrow \partial\Phi_1/\partial y|$
end for
if element on X/Y boundary OR k layers inside Y **then**
Split element and exit
else if element inside X **then**
count=0
for i = 1 to 3 **do** {loop over amplitude components}
if $DR_i \geq \epsilon_1$ OR $DI_i \geq \epsilon_1$ **then**
count++
end if
end for
if count $\neq 0$ **then**
Split element and exit
end if
else {element is inside Y}
count = 0
for i = 1 to 3 **do** {loop over amplitude components}
if $DGPX_i \geq \epsilon_2$ OR $DGPY_i \geq \epsilon_2$ **then**
count++
end if
end for
if count $\neq 0$ **then**
Split element and exit
end if
end if

belongs to Y where the phase/amplitude equations are solved, variations in the x and y components of $\nabla\Phi_j$ are checked to see if they exceed another limit ϵ_2. If they do, this element is split. If none of the above criteria are satisfied, the element is not split and is automatically placed in the list of elements to be checked for coarsening.

As we demonstrate in the next section, by recursively applying the above refinement criteria to the quadtree, the finest elements are automatically placed around domain separatrices, solid/liquid interfaces, and defects.

6.6 Results and computational efficiency

Using the various approximations and algorithms described in the previous sections we are now in a position to solve the phase/amplitude and complex equations simultaneously in different parts of our computational domain using the AMR module of Greenwood and Provatas [117]. **Algorithm 3** shows the flow of control from the main subroutine in our computer program via pseudo-code. The complex amplitude equations, Eq. (5.1), are initially evolved everywhere until time N_{tr}, when initial transients completely vanish and the crystals evolve steadily outward. The domain is then split into subdomains X and Y, following which the reduced phase/amplitude equations, Eqs. (6.4) and (6.5), are evolved using a forward Euler time stepping scheme[10] in subdomain Y. The grid is refined after a predetermined number of time steps N_{adapt}, which is chosen heuristically. We wish to point out that the current implementation can handle only periodic boundary conditions. Work is currently underway to enable handling of more general boundary conditions.

Using this implementation, we simulated the same problem (same initial and boundary conditions and problem parameters) that was solved adaptively in section 6.1 using only the complex amplitude equations. Fig. 6.7 shows the crystal boundaries and grid structure at various times during the simulation. N_{tr} was chosen to be 3000 for this simulation. With $\Delta t = 0.04$, this implies that this simulation is identical to the previ-

[10]We have determined that the discrete versions of Eqs. (6.4) and (6.5) are numerically stable for the same time step size that satisfies the stability criterion in Eq. (5.3) for the complex amplitude equations (which are evolved in subdomain X).

Algorithm 3 Flow of control

```
InitVar() {Initialize program variables and parameters}
InitGrid() {decide where to initially refine/coarsen based on initial condition}
UpdateGhostsFV() {interpolate A_j, Ψ_j, Φ_j at ghost nodes}
ComputePhaseGradients(1) {compute ∇Φ_j everywhere}
UpdateGhostsPG() {interpolate ∇Φ_j at ghost nodes}
for i = 1 to N_tr − 1 do {evolve until initial transients subside}
  if i mod N_adapt = 0 OR i = 1 then
    AdaptGrid() {uses Algorithm 2}
  end if
  EvolveComplexAmp() {evolve Eq. (5.1) everywhere}
  UpdateAllFields() {compute Ψ_j and Φ_j from A_j}
  UpdateGhostsFV()
  ComputePhaseGradients(1)
  UpdateGhostsPG()
end for
DivideDomain() {call Algorithm 1 to split domain into X and Y}
for i = N_tr to N_end do {evolve after transients subside}
  if i mod N_adapt = 0 then
    DivideDomain()
    AdaptGrid()
  end if
  EvolveComplexAmp() {evolve Eq. (5.1) in X}
  EvolvePhaseAmp() {evolve Eqs. (6.4) and (6.5) in Y}
  UpdateAllFields() {evaluate Ψ_j and Φ_j in X, evaluate A_j in Y}
  UpdateGhostsFV()
  ComputePhaseGradients(i) {compute ∇Φ_j in X only, frozen gradient approx.}
  UpdateGhostsPG()
end for
```

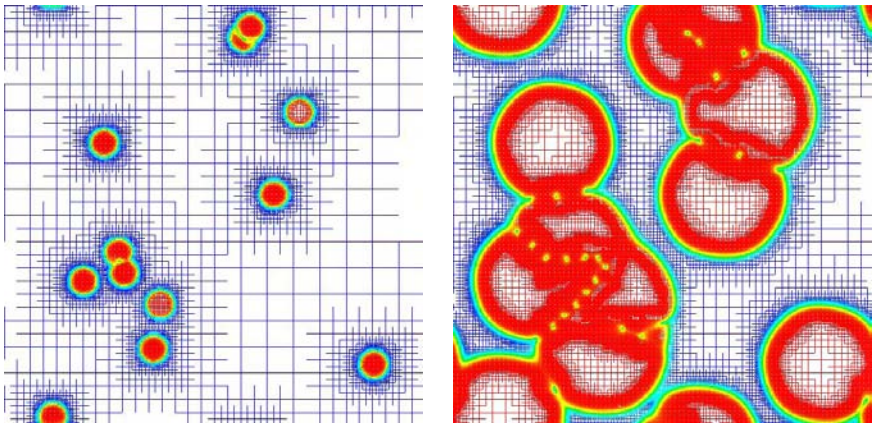

(a) $t = 0$

(d) $t = 248$

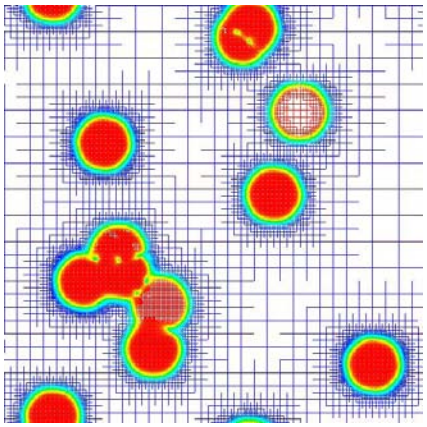

(b) $t = 88$

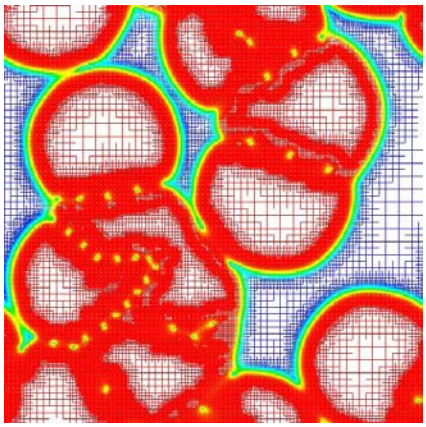

(e) $t = 320$

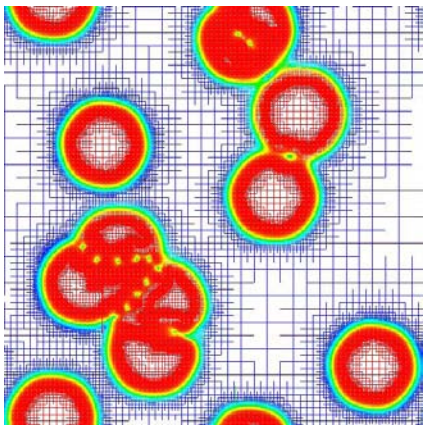

(c) $t = 168$

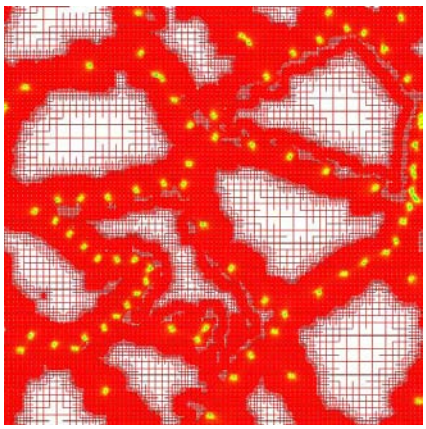

(f) $t = 552$

Figure 6.7: Evolution of a polycrystalline film simulated with Eq. (5.1), and Eqs. (6.4) and (6.5), on an adaptive grid. The conditions in this simulation are identical to those in section 6.1 and Fig. 6.1. Note that this time, the grid coarsens even inside grains that are misoriented with respect to $\mathbf{k}_j$, and "beats" are no longer a limitation. The colored field plotted is the average amplitude modulus, which is "red" inside the crystal phase, "blue" in the liquid phase, "green" at the crystal/liquid interface, and "yellow" near defects.

ous one until $t = N_{tr} \times \Delta t = 120$. Surely enough, Figs. 6.7(a) and 6.7(b) are identical to Figs. 6.1(a) and 6.1(b). The real advantage of the current implementation starts to appear from Fig. 6.7(c), whenceforth, unlike in Fig. 6.1, even grains that are misoriented with respect to the basis $\mathbf{k}_j$ show grid unrefinement within. It is also notable that the grid remains nicely refined near solid/liquid interfaces, grain boundaries, and defects, ensuring that key topological features are correctly resolved.

We now compare solutions from the two simulations quantitatively. We find it more informative to make a pointwise comparison of the two solutions along cross sections of the domain, rather than comparing solution norms, as we believe that this is a more severe test of our implementation. We choose two random cuts, one running parallel to the y axis at $x_{cut} = 70\pi$, and the other parallel to the x axis at $y_{cut} = 118\pi$. The solutions are compared along these cuts at two different times, $t = 168$ and $t = 552$ in Figs. 6.8 and 6.9 respectively. The solid curves in the figures (labeled "hybrid") are variations in Ψ_1 and $\partial\Phi_1/\partial x$ along the entire length of the domain as computed with the current implementation, whereas the symbols (labeled "complex") are variations in the same variables as computed using fully complex equations (section 6.1). The agreement is remarkable, indicating that our simplifications based on approximations in the preceeding sections work reasonably well.

Because the performance of our algorithm is sensitively tied to the type of problem that is being solved, it is difficult to come up with a universal metric that quantifies its computational efficiency. The difficulty lies in accounting for the change in CPU time per time step, which increases with the number of mesh points. For example, Fig. 6.10 shows the number of nodes in the simulation as a function of time steps. Clearly, an adaptive grid implementation would have a significant computational advantage over an equivalent fixed grid implementation at the earlier stages of the simulation.

One performance measure that we can certainly look at is the projected speed of our implementation over a uniform grid implementation of the PFC equation. This speedup

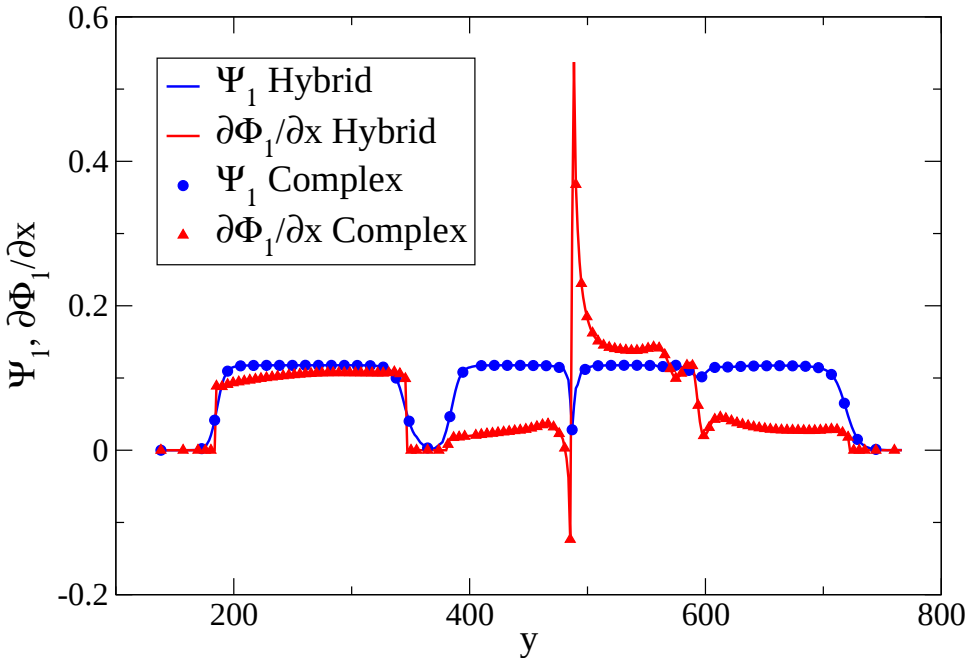

(a) $t = 168$

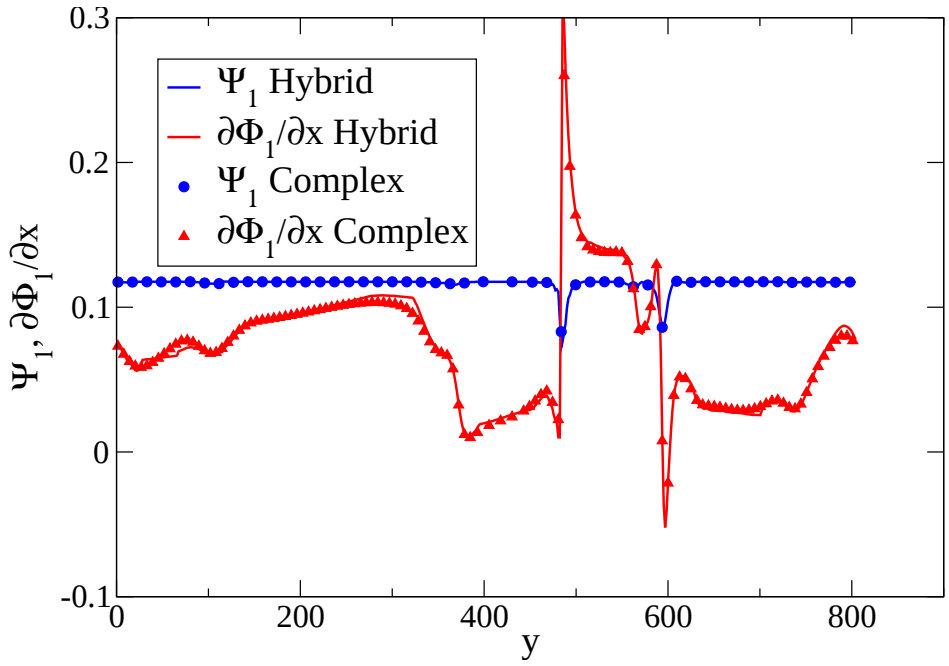

(b) $t = 552$

Figure 6.8: Pointwise comparison of the numerical solution obtained by solving only the complex amplitude equations adaptively, with that obtained by solving the phase/amplitude equations and complex amplitude equations simultaneously (hybrid) in different parts of the domain on an adaptive grid, at different instants of time, along the cross section $x = 70\pi$ in Fig. 6.7. Some of the data points in the complex solution were omitted for clarity of presentation.

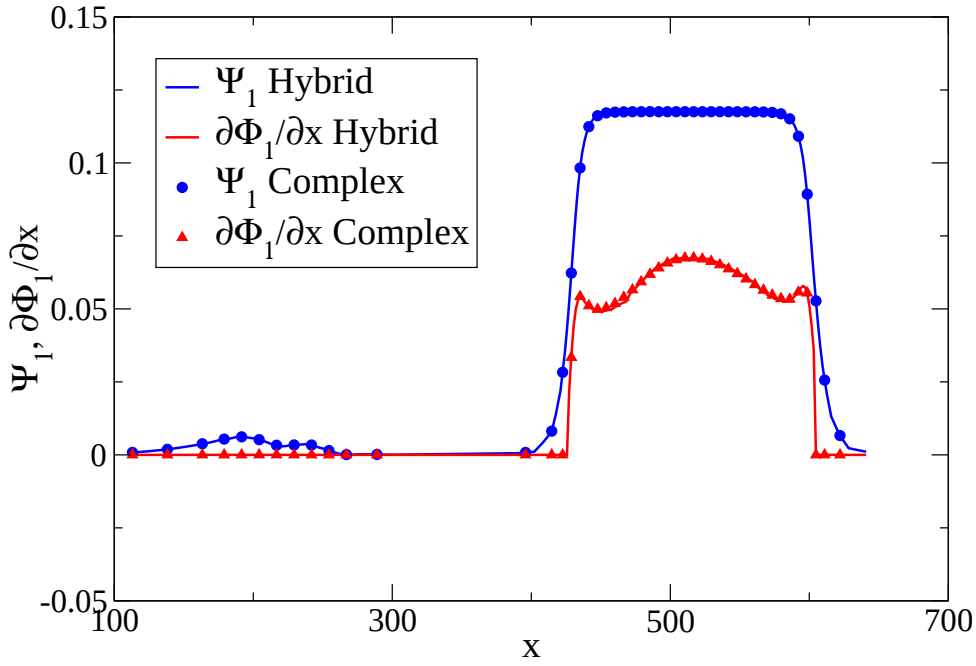

(a) $t = 168$

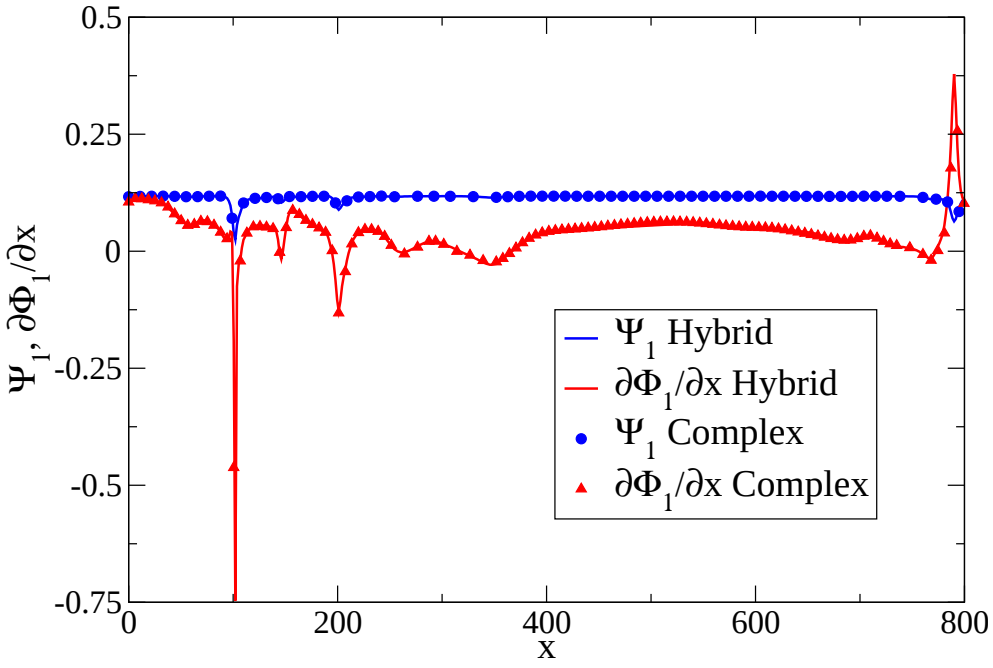

(b) $t = 552$

Figure 6.9: Pointwise comparison of the numerical solution obtained by solving only the complex amplitude equations adaptively, with that obtained by solving the phase/amplitude equations and complex amplitude equations simultaneously (hybrid) in different parts of the domain on an adaptive grid, at different instants of time, along the cross section $y = 118\pi$ in Fig. 6.7. Some of the data points in the complex solution were omitted for clarity of presentation.

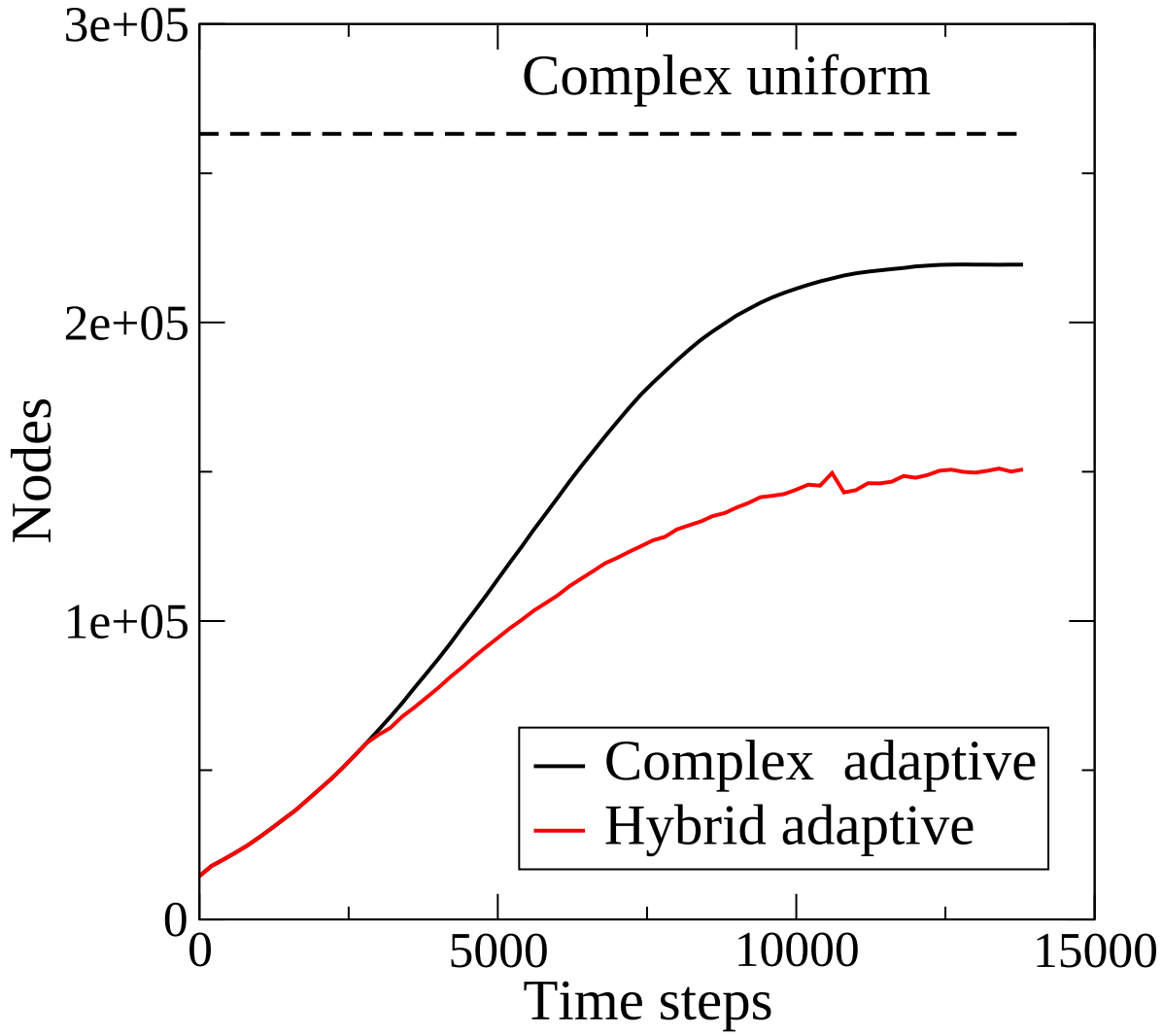

Figure 6.10: Number of computational nodes in the grid as a function of time, for simulations in Fig. 6.1 (black curve) and Fig. 6.7 (red curve). The number of nodes reaches a constant value after all the liquid freezes. The dashed line shows the number of nodes required by a uniform grid implementation of the complex amplitude equations for the same problem.

is estimated by the simple formula,

$$S = \frac{N_{PFC}}{N_{RG-AG}} \times \frac{\Delta t_{RG-AG}}{\Delta t_{PFC}} \times \frac{1}{6} \times \beta \tag{6.11}$$

where N_{PFC} is the number of grid points required to solve the PFC equation, N_{RG-AG} is the number of grid points required in a hybrid implementation of the amplitude/RG equations, Δt_{PFC} and Δt_{RG-AG} are the time steps used in the respective implementations, the factor 1/6 comes from solving six RG equations in place of the PFC equation, and $\beta \in [0, 1]$ is the overhead of the AMR algorithm. The difficulty lies in fixing N_{RG-AG} which is constantly changing with time. One estimate for N_{RG-AG}, that we find reasonable, is the average number of nodes across our simulation. This can be easily computed by dividing the area under the hybrid curve in Fig. 6.10 by the total number of time steps taken, which gives $N_{RG-AG} = 104,747$. Further, based on heuristics collected while running our code, we conservatively estimate mesh refinement/coarsening to constitute about 3% of the CPU time, which gives $\beta = 0.97$. Therefore, from Eq. (6.11) we have

$$S = \frac{1,050,625}{104,747} \times \frac{0.04}{0.008} \times \frac{1}{6} \times 0.97 = 8.1. \tag{6.12}$$

We do recognize that for a more accurate estimate of S we would also need to consider overhead costs that may come from sub-optimal cache and memory usage owing to the data structures used. Hence these numbers should only be considered as rough estimates of true speedup.

While a speedup factor of 8 may not seem a quantum leap in computational efficiency at first glance, the reader needs to bear in mind that the number of nodes in the AMR algorithm scales (roughly) linearly with interface/grain boundary length, which is quite substantial in the system we just simulated. Naturally, we do not expect the maximum computational benefit, when simulating systems with large numbers of grains. On the other hand, we can now simulate the growth of a few crystals in a system that was previously impossible to simulate with the PFC equation on our single processor machine with 1 GB of memory. We choose a square domain of side 4096π, which in physical dimen-

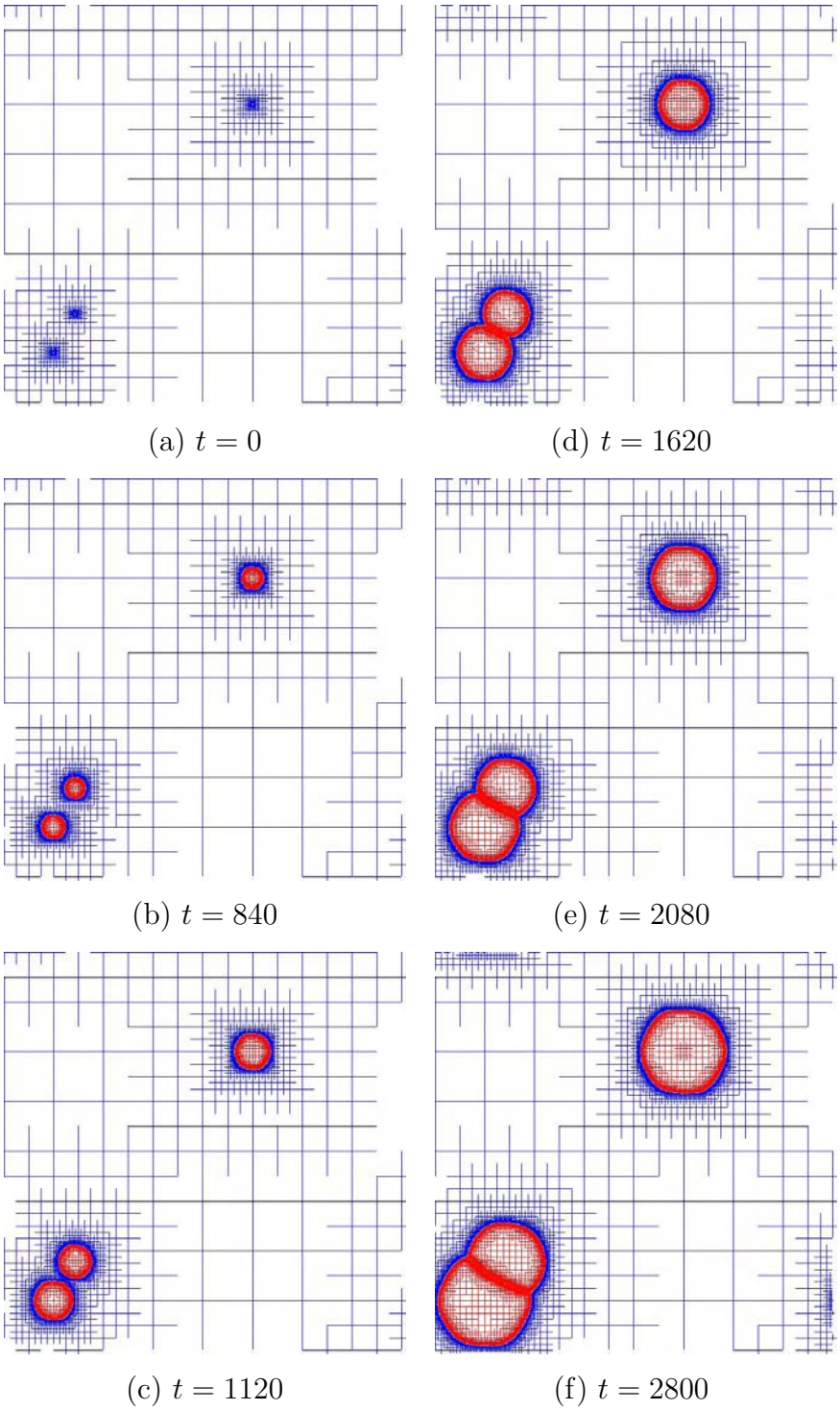

(a) $t = 0$ (d) $t = 1620$

(b) $t = 840$ (e) $t = 2080$

(c) $t = 1120$ (f) $t = 2800$

Figure 6.11: Micro-scale simulation of two dimensional crystal growth with amplitude equations using AMR.

sions translates to 722 nanometers (approaching a micron) if we assume an interatomic spacing of 4 Å units[11]. We initiate three randomly oriented crystals, two a little closer together than the third, so that a grain boundary forms quickly. The crystals are shown at different times in Fig. 6.11. The simulation was terminated at $t = 3960$ when memory requirements exceeded 1 GB, after running on a dedicated processor for about one week.

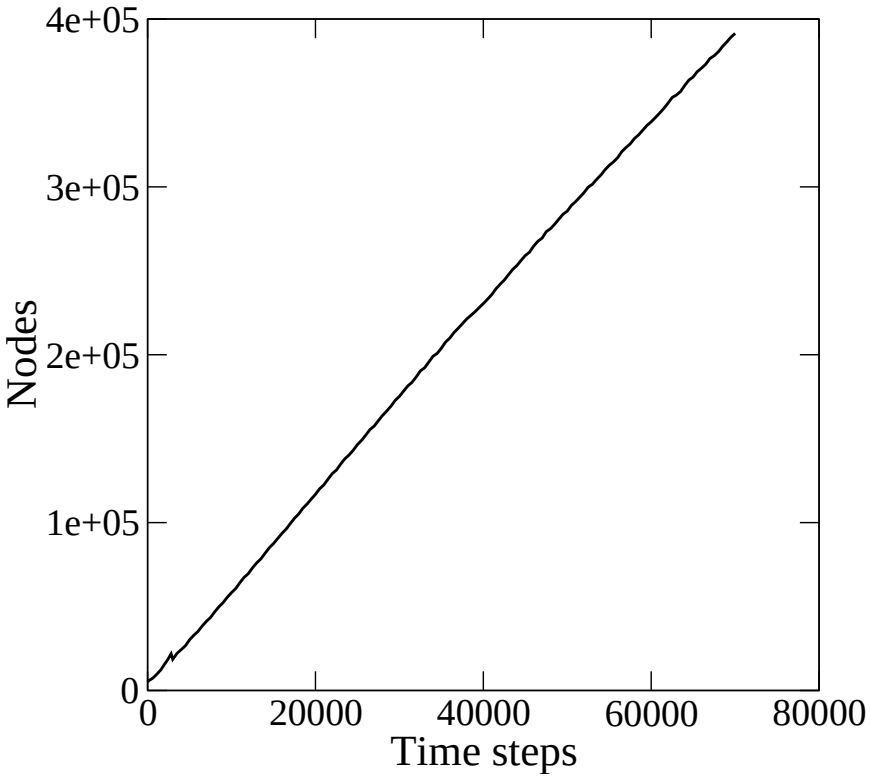

Figure 6.12: Number of computational nodes in the grid as a function of time for the 1 μm $\times$ 1μm domain. The growth is almost linear.

Let us calculate the speedup factor for this simulation as we did previously, after $70,000$ time steps ($t = 2800$, Fig. 6.11(f)). Fig. 6.12 shows the number of nodes in the adaptive grid to be varying nearly linearly with the number of time steps, and we estimate the average number of nodes N_{AG-RG} to be $200,721$. The same simulation on a uniform grid using the PFC equation would have required $268,435,456$ nodes (not possible on our computers). We estimate $\beta = 0.98$. In this case the speedup is about three orders of

[11]This is the interatomic spacing in Aluminum [125], which has a face centered cubic lattice.

magnitude,

$$S = \frac{268,435,456}{200,721} \times \frac{0.04}{0.008} \times \frac{1}{6} \times 0.98 = 1091. \tag{6.13}$$

Fig. 6.13 paints a more vivid picture of the range of length scales from nanometers to microns spanned by our grid in this simulation highlighting its "multiscale" capability.

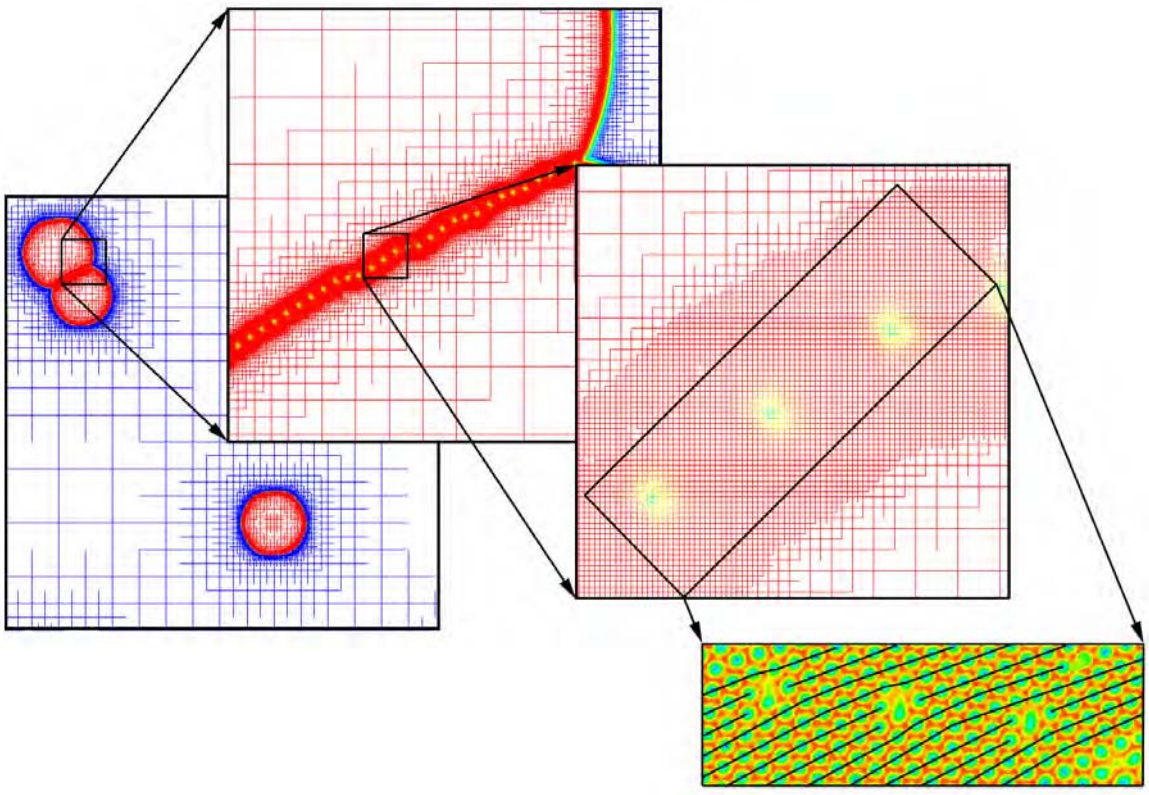

Figure 6.13: The above grid spans roughly three orders of magnitude in length scales, from a nanometer up to a micron. The leftmost box resolves the entire computational domain whereas the rightmost resolves dislocations at the atomic scale.

We would like to emphasize that as with any adaptive grid implementation, refinement criteria can change S by a constant factor, approximately. In order to enable testing our implementation on a much larger domain subject to the available memory resources, the criteria were relaxed. Note however, that even if we had roughly doubled the number of finely spaced nodes near the interfaces and the grain boundary, which would lead to a significantly more accurate calculation, S would still be about 500 times faster than an equivalent implementation of the PFC equation on a uniform grid.

Chapter 7

Conclusions and future directions

To summarize (Chapters 3-6), we first presented a theoretical approach for deriving coarse-grained amplitude equations from the nanoscopic PFC equation, by perturbatively applying the renormalization group. Using solutions to the amplitude equations, high-fidelity approximations to solutions of the PFC equation can be constructed, when the parameters r and $\bar{\psi}$ are chosen in a regime that satisfies the assumptions made in the derivation of these equations. We further demonstrated that by numerically solving the amplitude equations, the evolution of polycrystalline systems can be accurately modeled, with predictions of grain boundary energy as a function of grain misorientation closely adhering to trends shown by the PFC equation and an analytical model of grain boundaries. We also presented some exciting preliminary results from our ongoing work to simulate two dimensional heteroepitaxial growth of thin films and the resulting dislocation dynamics, with amplitude equations.

We showed that even on uniform grids it is computationally efficient to solve amplitude equations in place of the PFC equation. We then proceeded to develop a more efficient hybrid numerical implementation, that combines cartesian and polar representations of the complex amplitude with adaptive mesh refinement, and allows the modeling capabilities of the PFC equation to be extended to micro- length scales, as shown in Fig. 7.1. Depending on the choice of application, we have shown that our scheme can be anywhere between $1-3$ orders of magnitude times faster than an equivalent uniform

grid implementation of the PFC equation, on a single processor machine. We anticipate that this edge will be preserved when both implementations are migrated to a parallel computer, which is an important next step required to give the RG extension of the PFC model full access to micro- and meso- scale phenomena.

In conclusion, we have shown that multiscale modeling of complex polycrystalline materials microstructure is possible using a combination of continuum modeling at the nanoscale using the PFC model, RG and related techniques from spatially-extended dynamical systems theory, and adaptive mesh refinement.

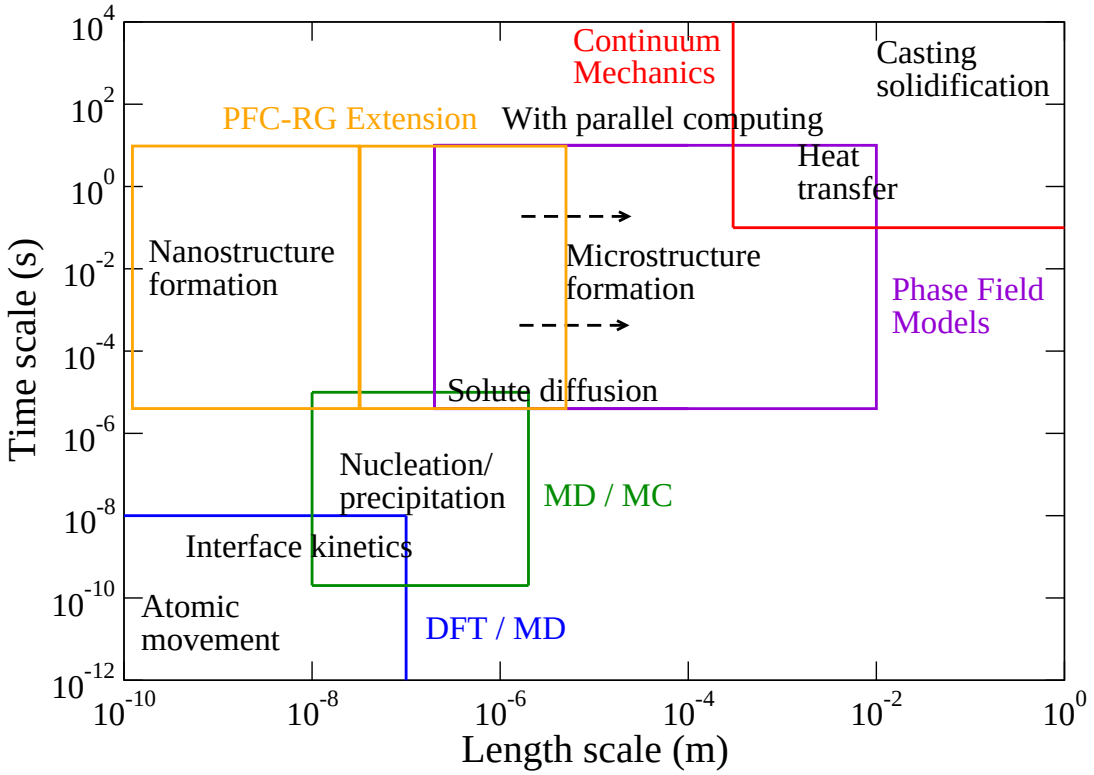

Figure 7.1: Adaptive grid–Renormalization Group extension of the PFC model to micro-length scales.

We regard this work as only a first step out of many that need to taken before our modeling approach with the RG extension of the PFC can be successfully adapted for studying important engineering and materials science applications. We have identified a few issues that require immediate attention. The first, although an implementation

issue, is critical, and has to do with using amplitude equations for applications involving externally applied loads and displacements to a polycrystal that has been evolved with our equations. Simple applications could be, subjecting the polycrystal to shear, uniaxial, or biaxial loading states [28, 86]. Such boundary conditions are difficult enough to apply to the scalar field ψ in the PFC equation. Meaningfully translating them to equivalent boundary conditions on the amplitudes and phases of ψ can be a very difficult task, requiring the solution of systems of nonlinearly coupled equations at the boundaries. Apart from the two dimensional heteroepitaxial growth problem, where the amplitude boundary condition we used was relatively easy to implement, we have not investigated this issue in any detail. An efficient technique to implement such boundary conditions with the amplitude equations needs to be developed.

The next couple of issues are more fundamental. Our derivation of the amplitude equations was based on a one mode approximation to the triangular lattice, and as we always chose parameters fairly close to the boundary between the triangular phase and coexisting triangular and constant phases, i.e. $|r + 3\bar{\psi}^2| \ll 1$, the amplitude equations we derived were within their validity and our results were quite accurate. It is almost certain that a one-mode approximation will not give similarly accurate results if we operated in regimes where $|r + 3\bar{\psi}^2| \sim \mathcal{O}(1)$ (although it would be interesting to see how much the error actually is). It is not clear if this in any way precludes certain phenomena from being studied with our equations, as we can always choose parameters to stay in the regime where the one-mode approximation is valid, but if it does, amplitude equations for dominant higher modes can be systematically developed using the same techniques described in Chapter 4 of this thesis.

An important assumption made in the derivation of our so called "hybrid" formulation of the complex amplitude equations is that of locally freezing the phase gradient vector $\nabla\Phi_j$. In fact, it is this assumption that allows us to effectively unrefine the interior of grains and gain significant speedup over the PFC equation. If for example, the problem we are studying involves the application of a large external shear strain that could change $\nabla\Phi_j$ in the grain interior via grain rotation, it is uncertain if our algorithm would continue

to maintain its superior computational efficiency over the PFC. This is again a matter worth investigating.

Other important future directions involve extending the ideas described herein to materials modeling in three dimensions, and making contact with real materials.

List of References

[1] R. Phillips, *Crystals, defects and microstructures: modeling across scales.* Cambridge University Press, 2001.

[2] E. B. Tadmor, M. Ortiz, and R. Phillips, "Quasicontinuum analysis of defects in solids," *Phil. Mag. A*, vol. 73, pp. 1529–1563, 1996.

[3] V. B. Shenoy, R. Miller, E. B. Tadmor, R. Phillips, and M. Ortiz, "Quasicontinuum models of interfacial structure and deformation," *Phys. Rev. Lett.*, vol. 80, pp. 742–745, 1998.

[4] J. Knap and M. Ortiz, "An analysis of the quasicontinuum method," *J. Mech. Phys. Solids*, vol. 49, pp. 1899–1923, 2001.

[5] R. E. Miller and E. B. Tadmor, "The quasicontinuum method: Overview, applications and current directions," *Journal of Computer-Aided Materials Design*, vol. 9, pp. 203–239, 2002.

[6] W. E, B. Enquist, and Z. Huang, "Heterogeneous multiscale method: a general methodology for multiscale modeling," *Phys. Rev. B*, vol. 67, pp. 092101:1–4, 2003.

[7] W. E and Z. Huang, "Matching conditions in atomistic-continuum modeling of materials," *Phys. Rev. Lett.*, vol. 87, pp. 135501:1–4, 2001.

[8] R. E. Rudd and J. Broughton, "Coarse-grained molecular dynamics and the atomic limit of finite elements," *Phys. Rev. B*, vol. 58, pp. R5893–5896, 1998.

[9] J. Q. Broughton, F. F. Abraham, N. Bernstein, and E. Kaxiras, "Concurrent coupling of length scales: methodology and application," *Phys. Rev. B*, vol. 60, pp. 2391–2403, 1998.

[10] C. Denniston and M. O. Robbins, "Mapping molecular models to continuum theories for partially miscible fluids," *Phys. Rev. E*, vol. 69, pp. 021505:1–19, 2004.

[11] S. Curtarolo and G. Ceder, "Dynamics of an inhomogeneously coarse grained multiscale system," *Phys. Rev. Lett.*, vol. 88, pp. 255504:1–4, 2002.

[12] J. Fish and W. Chen, "Discrete-to-continuum bridging based on multigrid principles," *Comp. Meth. Appl. Mech. Eng.*, vol. 193, pp. 1693–1711, 2004.

[13] J. S. Langer, "Models of pattern formation in first-order phase transitions," in *Directions in Condensed Matter Physics* (G. Grinstein and G. Mazenko, eds.), vol. 1, p. 165, World Scientific, 1986.

[14] A. Karma and W. J. Rappel, "Quantitative phase-field modeling of dendritic growth in two and three dimensions," *Phys. Rev. E*, vol. 57, p. 4323, 1998.

[15] C. Beckermann, H.-J.Diepers, I. Steinbach, A. Karma, and X. Tong, "Modeling melt convection in phase-field simulations of solidification," *J. Comp. Phys.*, vol. 154, p. 468, 1999.

[16] J. A. Warren, R. Kobayashi, A. E. Lobkovsky, and W. C. Carter, "Extending phase field models of solidification to polycrystalline materials," *Acta. Mater.*, vol. 51, pp. 6035–6058, 2003.

[17] D. D. Vvedensky, "Multiscale modelling of nanostructures," *J. Phys.: Condens. Matter*, vol. 16, pp. R1537–R1576, 2004.

[18] N. Provatas, N. Goldenfeld, and J. Dantzig *Phys. Rev. Lett.*, vol. 80, p. 3308, 1998.

[19] J. Jeong, N. Goldenfeld, and J. Dantzig, "Phase field model for three-dimensional dendritic growth with fluid flow," *Phys. Rev. E*, vol. 64, p. 041602:1, 2001.

[20] R. Kobayashi, J. A. Warren, and W. C. Carter, "Vector-valued phase field model for crystallization and grain boundary formation," *Physica D*, vol. 119, p. 415, 1998.

[21] R. Kobayashi, J. A. Warren, and W. C. Carter, "A continuum model of grain boundaries," *Physica D*, vol. 140, p. 141, 2000.

[22] A. Onuki, "Ginzburg-landau approach to elastic effects in the phase separation of solids," *J. Phys. Soc. Jpn.*, vol. 58, p. 3065, 1989.

[23] A. Onuki, "Long-range interactions through elastic fields in phase-separating solids," *J. Phys. Soc. Jpn.*, vol. 58, p. 3069, 1989.

[24] J. Muller and M. Grant, "Model of surface instabilities induced by stress," *Phys. Rev. Lett.*, p. 1736, 1999.

[25] K. Kassner, C. Misbah, J. Muller, J. Kappey, and P. Kohlert, "Phase-field modeling of stress-induced instabilities," *Phys. Rev. E*, p. 036117, 2001.

[26] A. Karma, D. A. Kessler, and H. Levine, "Phase-field model of Mode III dynamic fracture," *Phys. Rev. Lett.*, vol. 87, p. 045501, 2001.

[27] K. R. Elder, M. Katakowski, M. Haataja, and M. Grant, "Modeling elasticity in crystal growth," *Phys. Rev. Lett.*, vol. 88, pp. 245701:1–4, 2002.

[28] K. R. Elder and M. Grant, "Modeling elastic and plastic deformations in non-equilibrium processing using phase field crystals," *Phys. Rev. E*, vol. 70, pp. 051605:1–18, 2004.

[29] N. Goldenfeld, O. Martin, Y. Oono, and F. Liu, "Anomalous dimensions and the renormalization group in a nonlinear diffusion process," *Phys. Rev. Lett.*, vol. 64, pp. 1361–1364, 1990.

[30] N. Goldenfeld, *Lectures on phase transitions and the renormalization group.* Addison-Wesley, 1992.

[31] C. Bowman and A. C. Newell, "Natural patterns and wavelets," *Rev. Mod. Phys.*, vol. 70, pp. 289–301, 1998.

[32] L. Chen, N. Goldenfeld, and Y. Oono, "The renormalization group and singular perturbations: multiple-scales, boundary layers and reductive perturbation theory," *Phys. Rev. E*, vol. 54, pp. 376–394, 1996.

[33] R. Graham, "Systematic derivation of a rotationally covariant extension of the two-dimensional newell-whitehead-segel equation," *Phys. Rev. Lett.*, vol. 76, pp. 2185–2187, 1996.

[34] K. Nozaki, Y. Oono, and Y. Shiwa, "Reductive use of renormalization group," *Phys. Rev. E*, vol. 62, pp. R4501–R4504, 2000.

[35] S. Sasa, "Renormalization group derivation of phase equations," *Physica D*, vol. 108, pp. 45–59, 1997.

[36] Y. Shiwa, "Renormalization group theoretical reduction of the swift-hohenberg equation," *Phys. Rev. E*, vol. 63, pp. 016119:1–7, 2000.

[37] M. C. Cross and A. C. Newell, "Convection patterns in large aspect ratio systems," *Physica D*, vol. 10, pp. 299–328, 1984.

[38] T. Passot and A. C. Newell, "Towards a universal theory of patterns," *Physica D*, vol. 74, pp. 301–352, 1994.

[39] A. C. Newell, T. Passot, and J. Lega, "Order parameter equations for patterns," *Annu. Rev. Fluid Mech.*, vol. 25, pp. 399–453, 1993.

[40] M. C. Cross and P. C. Hohenberg, "Pattern formation outside of equilibrium," *Rev. Mod. Phys.*, vol. 65, pp. 851–1112, 1993.

[41] B. P. Athreya, J. A. Dantzig, S. Liu, and R. Trivedi, "On the role of confinement on solidification in pure materials and binary alloys," *Philos. Mag.*, vol. 86, p. 3739, 2006.

[42] B. P. Athreya and J. A. Dantzig, "Dendritic growth in confined spaces," in *Solidification Processes and Microstructures: A symposium in honor of Wilfried Kurz* (M. Rappaz, C. Beckermann, and R. Trivedi, eds.), p. 357, TMS-AIME, 2004.

[43] N. Provatas, M. Greenwood, B. P. Athreya, N. Goldenfeld, and J. A. Dantzig, "Multiscale modeling of solidification: Phase-field methods to adaptive mesh refinement," *Int. J. Mod. Phys. B*, vol. 19, p. 4525, 2005.

[44] B. P. Athreya, N. Goldenfeld, and J. A. Dantzig, "Renormalization-group theory for the phase-field crystal equation," *Phys. Rev. E*, vol. 74, p. 011601, 2006.

[45] N. Goldenfeld, B. P. Athreya, and J. A. Dantzig, "Renormalization group approach to multiscale simulation of polycrystalline materials using the phase field crystal model," *Phys. Rev. E*, vol. 72, p. 020601(R), 2005.

[46] N. Goldenfeld, B. P. Athreya, and J. A. Dantzig, "Renormalization group approach to multiscale modelling in materials science," *J. Stat. Phys.*, vol. Online First, 2006.

[47] G. P. Ivantsov, "Temperature field around spherical, cylindrical, and needle-shaped crystals which grow in supercooled melts," *Dokl. Akad. Nauk USSR*, vol. 58, p. 1113, 1947.

[48] D. E. Temkin, "Growth rate of the needle-crystal formed in a supercooled melt," *Dokl. Akad. Nauk SSSR*, vol. 132, p. 1307, 1960.

[49] J. S. Langer and H. Müller-Krumbhaar, "Stability effects in dendritic crystal growth," *J. Cryst. Growth*, vol. 42, p. 11, 1977.

[50] J. S. Langer and H. Müller-Krumbhaar, "Theory of dendritic growth I: Elements of a stability analysis," *Acta Metall.*, vol. 26, p. 1681, 1978.

[51] R. Brower, D. Kessler, J. Koplik, and H. Levine, "Geometrical approach to moving-interface dynamics," *Phys. Rev. Lett.*, vol. 51, p. 1111, 1983.

[52] E. Ben-Jacob, N. Goldenfeld, J. Langer, and G. Schön, "Dynamics of interfacial pattern formation," *Phys. Rev. Lett.*, vol. 51, p. 1930, 1983.

[53] E. Ben-Jacob, N. Goldenfeld, B. Kotliar, and J. Langer, "Pattern selection in dendritic solidification," *Phys. Rev. Lett.*, vol. 53, p. 2110, 1984.

[54] M. E. Glicksman and R. J. Schaefer, "Investigations of solid/liquid interface temperatures via isenthalpic solidification," *J. Cryst. Growth*, vol. 1, p. 297, 1967.

[55] S.-C. Huang and M. Glicksman, "Fundamentals of dendritic solidification. I - Steady-state tip growth. II - Development of sidebranch structure," *Acta Metall.*, vol. 29, p. 1697, 1981.

[56] M. B. Koss, M. E. Glicksman, A. O. Lupulescu, L. A. Tennenhouse, J. C. LaCombe, D. C. Corrigan, J. E. Frei, and D. C. Malarik, "Comparison of dendritic growth in pivalic acid and succinonitrile under microgravity and terrestrial gravity conditions." 36th Aerospace Sciences Meeting, January 12-15, 1998, Reno, NV, AIAA-98-0809.

[57] N. Provatas, J. Dantzig, and N. Goldenfeld, "Efficient computation of dendritic microstructures using adaptive mesh refinement," *Phys. Rev. Lett.*, vol. 80, p. 3308, 1998.

[58] N. Provatas, J. Dantzig, and N. Goldenfeld, "Adaptive mesh refinement computation of solidification microstructures using dynamic data structures," *J. Comp. Phys.*, vol. 148, p. 1, 1999.

[59] W. N. Gill, Y. W. Lee, K. K. Koo, and R. Ananth, "Interaction of thermal and forced convection with the growth of dendritic crystals," in *Interactive Dynamics of Convection and Solidification* (S. H. Davis, H. E. Huppert, U. Müller, and M. G. Worster, eds.), Kluwer Academic Publishers, 1992.

[60] Y.-W. Lee, R. Ananth, and W. N. Gill, "Selection of length scale in unconstrained dendritic growth with convection in melt," *J. Cryst. Growth*, vol. 132, p. 226, 1993.

[61] P. Bouissou, B. Perrin, and P. Tabeling, "Influence of an external flow on dendritic crystal growth," *Phys. Rev. A*, vol. 40, p. 509, 1989.

[62] D. A. Saville and P. J. Beaghton, "Growth of needle-shaped crystals in the presence of convection," *Phys. Rev. A*, vol. 37, no. 9, pp. 3423–3430, 1988.

[63] R. Trivedi, "Theory of dendrite growth during the directional solidification of binary alloys," *J. Cryst. Growth*, vol. 49, p. 219, 1980.

[64] W. Kurz and D. J. Fisher, *Fundamentals of Solidification.* Trans Tech Publications, third ed., 1989.

[65] K. Somboonsuk, J. T. Mason, and R. Trivedi, "Interdendritic spacing. I.–Experimental studies," *Met. Trans. A*, vol. 15A, p. 967, 1984.

[66] S. Liu and R. Trivedi, private communications.

[67] A. Karma, "Phase-field formulation for quantitative modeling of alloy solidification," *Phys. Rev. Lett.*, vol. 87, p. 115701:1, 2001.

[68] B. Echebarria, R. Folch, A. Karma, and M. Plapp, "Quantitative phase field model of alloy solidification," *Phys. Rev. E*, vol. 70, p. 061604, 2004.

[69] P. M. Gresho, S. T. Chan, M. A. Christon, and A. C. Hindmarsh, "A little more on stabilized Q_1Q_1 for transient viscous incompressible flow," *Int. J. Numer. Methods Fluids*, vol. 21, p. 837, 1995.

[70] A. Sémoroz, S. Henry, and M. Rappaz, "Application of the phase-field method to the solidification of hot-dipped galvanized coatings," *Met. Trans. A*, vol. 31A, p. 487, 2000.

[71] W. W. Mullins and R. F. Sekerka, "Stability of a planar interface during solidification of a dilute binary alloy," *J. Appl. Physics*, vol. 35, pp. 444–451, 1964.

[72] L. X. Liu and J. S. Kirkaldy, "Systematics of thin film cellular dendrites and the cell-to-dendrite transition in succinonitrile-salol, succinonitrile-acetone and pivalic acid-ethanol," *J. Cryst. Growth*, vol. 140, p. 115, 1994.

[73] H. Henry and H. Levine, "Dynamic instabilities of fracture under biaxial strain using a phase field model," *Phys. Rev. Lett.*, vol. 93, p. 105504, 2004.

[74] R. Spatschek, M. Hartmann, E. Brener, H. Muller-Krumbhaar, and K. Kassner, "Phase field modeling of fast crack propagation," *Phys. Rev. Lett.*, vol. 96, p. 015502, 2006.

[75] F. H. Fenton, E. M. Cherry, A. Karma, and W.-J. Rappel, "Modeling wave propagation in realistic heart geometries using the phase-field method," *Chaos*, vol. 15, p. 013502, 2005.

[76] Y. U. Wang, Y. M. Jin, A. M. Cuitino, and A. G. Khachaturyan, "Nanoscale phase field microelasticity theory of dislocations: Model and 3D simulations," *Acta. Mater.*, vol. 49, p. 1847, 2001.

[77] M. Koslowski, A. M. Cuitino, and M. Ortiz, "A phase-field theory of dislocation dynamics, strain hardening and hysteresis in ductile single crystals," *J. Mech. Phys. Solids*, vol. 50, p. 2597, 2002.

[78] L.-Q. Chen, "Phase-field models for microstructure evolution," *Ann. Rev. Mat. Research*, vol. 32, p. 113, 2002.

[79] C.-A. Gandin and M. Rappaz, "A coupled finite element-cellular automaton model for the prediction of dendritic grain structures in solidification processes," *Acta. Mater.*, vol. 42, p. 2233, 1994.

[80] I. Steinbach, C. Beckermann, B. Kauerauf, Q. Li, and J. Guo, "Three-dimensional modeling of equiaxed dendritic growth on a mesoscopic scale," *Acta. Mater.*, vol. 47, p. 971, 1999.

[81] B. Cantor and A. Vogel, "Dendritic solidification and fluid flow," *J. Cryst. Growth*, vol. 41, p. 109, 1977.

[82] M. Haataja, J. Muller, A. D. Rutenberg, and M. Grant, "Dislocations and morphological instabilities: Continuum modeling of misfitting heteroepitaxial films," *Phys. Rev. B*, p. 165414, 2002.

[83] B. I. Halperin, P. C. Hohenberg, and S. K. Ma, "Renormalization group methods for critical dynamics: I. Recursion relations and effects of energy conservation," *Phys. Rev. B*, vol. 10, p. 139, 1974.

[84] R. Kubo, "The fluctuation-dissipation theorem," *Reports on Progress in Physics*, vol. 29, p. 255, 1966.

[85] I. Prigogine and R. Defay, *Chemical Thermodyanics*. Longman, 1967.

[86] J. Berry, M. Grant, and K. R. Elder, "Diffusive atomistic dynamics of edge dislocations in two dimensions," *Phys. Rev. E*, vol. 73, p. 031609, 2006.

[87] P. Stefanovic, M. Haataja, and N. Provatas, "Phase-field crystals with elastic interactions," *Phys. Rev. Lett.*, 2006. To appear. Preprint at http://arxiv.org/abs/cond-mat/0601619.

[88] K. Nozaki and Y. Oono, "Renormalization-group theoretical reduction," *Phys. Rev. E*, vol. 63, p. 046101, 2001.

[89] J. Swift and P. C. Hohenberg, "Hydrodynamic fluctuations at the convective instability," *Phys. Rev. A*, vol. 15, pp. 319–328, 1977.

[90] H. S. Greenside and W. M. Coughran, "Nonlinear pattern formation near the onset of Rayleigh-Bénard convection," *Phys. Rev. A*, vol. 30, p. 398, 1984.

[91] G. H. Gunaratne, Q. Ouyang, and H. Swinney, "Pattern formation in the presence of symmetries," *Phys. Rev. E*, vol. 50, pp. 2802–2820, 1994.

[92] M. C. Cross, "Ingredients of a theory of convective textures close to onset," *Phys. Rev. A*, vol. 25, p. 1065, 1982.

[93] A. C. Newell and J. A. Whitehead, "Finite bandwidth, finite amplitude convection," *J. Fluid Mech.*, vol. 38, p. 279, 1969.

[94] L. A. Segel, "Distant side-walls cause slow amplitude modulation of cellular convection," *J. Fluid Mech.*, vol. 38, p. 203, 1969.

[95] P. A. Sturrock, "Nonlinear effects in electron plasmas," *Proc. Roy. Soc. London*, p. 277, 1957.

[96] E. A. Frieman, "On a new method in the theory of irreversible processes," *J. Math. Phys.*, vol. 4, p. 410, 1963.

[97] C. Bender and S. A. Orszag, *Advanced mathematical methods for scientists and engineers*. McGraw-Hill, 1978.

[98] A. H. Nayfeh, *Introduction to perturbation techniques*. Wiley, 1981.

[99] P. C. Matthews and S. M. Cox, "Pattern formation with a conservation law," *Nonlinearity*, vol. 13, p. 1293, 2000.

[100] S. M. Cox and P. C. Matthews, "Instability and localisation of patterns due to a conserved quantity," *Physica D*, vol. 175, p. 196, 2003.

[101] M. Bestehorn and H. Haken, "Traveling waves and pulses in a two-dimensional large-aspect-ratio system," *Phys. Rev. A*, vol. 42, pp. 7195–7203, 1990.

[102] J. Guckenheimer and P. Holmes, *Nonlinear Oscillations, Dynamical Systems, and Bifurcations of Vector Fields*. Springer-Verlag, New York, 1983.

[103] S. Wiggins, *Introduction to applied nonlinear dynamical systems and chaos*. Springer, 2003.

[104] E. Buzano and M. Golubitsky, "Bifurcation involving the hexagonal lattice and the planar Bénard problem," *Philos. Trans. Roy. Soc. London A*, vol. 308, pp. 617–667, 1983.

[105] S. Ciliberto, P. Coullet, J. Lega, E. Pampaloni, and C. Perez-Garcia, "Defects in roll-hexagon competition," *Phys. Rev. Lett.*, vol. 65, pp. 2370–2373, 1990.

[106] W. T. Read and W. Shockley, "Dislocation models of crystal grain boundaries," *Phys. Rev.*, vol. 78, p. 275, 1950.

[107] J. W. Matthews and A. E. Blakeslee, "Defects in epitaxial multilayers. II. Dislocation pile-ups, threading dislocations, slip lines and cracks," *J. Cryst. Growth*, vol. 29, p. 273, 1975.

[108] C. Eisenmann, U. Gasser, P. Keim, G. Maret, and H. H. von Grünberg, "Pair interaction of dislocations in two-dimensional crystals," *Phys. Rev. Lett.*, vol. 95, p. 185502, 2005.

[109] M. Ambrozic, S. Kralj, T. J. Sluckin, S. Zumer, and D. Svensek, "Annihilation of edge dislocations in smectic-A liquid crystals," *Phys. Rev. E*, vol. 70, p. 051704, 2004.

[110] C.-W. Shu and S. Osher, "Efficient implementation of essentially non-oscillatory shock-capturing schemes, II," *J. Comp. Phys.*, vol. 83, p. 32, 1989.

[111] X.-D. Liu, S. Osher, and T. Chan, "Weighted essentially non-oscillatory schemes," *J. Comp. Phys.*, vol. 115, p. 200, 1994.

[112] J. A. Sethian, "A fast marching level set method for monotonically advancing fronts," *Proc. Nat. Acad. Sci.*, vol. 93, p. 1591, 1996.

[113] K. E. Harris, V. V. Singh, and A. H. King, "Grain rotation in thin films of gold," *Acta. Mater.*, vol. 46, p. 2623, 1998.

[114] D. Moldovan, V. Yamakov, D. Wolf, and S. R. Phillpot, "Scaling behavior of grain-rotation-induced grain growth," *Phys. Rev. Lett.*, vol. 89, p. 206101, 2002.

[115] D. Moldovan, D. Wolf, S. R. Phillpot, and A. J. Haslam, "Role of grain rotation during grain growth in a columnar microstructure by mesoscale simulation," *Acta. Mater.*, vol. 50, p. 3397, 2002.

[116] D. Moldovan, D. Wolf, S. R. Phillpot, and A. J. Haslam, "Mesoscopic simulation of two-dimensional grain growth with anisotropic grain-boundary properties," *Philos. Mag. A*, vol. 82, p. 1271, 2002.

[117] J. Fan, M. Greenwood, M. Haataja, and N. Provatas, "Phase field simulations of velocity selection in rapidly solidified binary alloys," Under review.

[118] H. Samet, "The quadtree and related hierarchical data structures," *ACM Computing Surveys*, vol. 16, p. 187, 1984.

[119] M. A. Yerry and M. S. Shephard, "Automatic three-dimensional mesh generation by the modified octree technique," *Int. J. Num. Meth. Eng.*, vol. 20, p. 1965, 1984.

[120] M. A. Yerry and M. S. Shephard, "Trends in engineering software and hardware: Automatic mesh generation for three-dimensional solids," *Computers and Structures*, vol. 20, p. 31, 1985.

[121] P. L. Baehmann, S. L. Wittchen, M. S. Shephard, K. R. Grice, and M. A. Yerry, "Robust, geometrically based, automatic two-dimensional mesh generation," *Int. J. Num. Meth. Eng.*, vol. 24, p. 1043, 1987.

[122] J. Jeong, J. A. Dantzig, and N. Goldenfeld, "Dendritic growth with fluid flow in pure materials," *Met. Trans. A*, vol. 34, pp. 459–466, 2003.

[123] O. C. Zienkiewicz and J. Z. Zhu, "A simple error estimator and adaptive procedure for practical engineering analysis," *Int. J. Num. Meth. Eng.*, vol. 24, p. 337, 1987.

[124] M. J. Berger and J. E. Oliger, "Adaptive mesh refinement for hyperbolic partial differential equations," *J. Comp. Phys.*, vol. 53, p. 484, 1984.

[125] W. D. Callister, *Materials science and engineering.* Wiley, 1997.

[126] H. Tomita, "Preservation of isotropy at the mesoscopic stage of phase separation processes," *Prog. Theor. Phys.*, vol. 85, p. 47, 1991.

[127] J. A. Sethian and J. Strain, "Crystal growth and dendritic solidification," *J. Comp. Phys.*, vol. 98, p. 231, 1992.

Appendix A

RG Analysis of the Van der Pol Oscillator

In this appendix, we explore the commuting of differentiation and renormalization with a simple ordinary differential equation example: the Van der Pol oscillator. Note that this yet another case in which a differential operator is multiplied by a small parameter (see right hand side of Eq.(A.1)).

The autonomous ODE is given by

$$y'' + y = \epsilon(1 - y^2)y', \tag{A.1}$$

where $'$ denotes differentiation with respect to the variable t. As there is a derivative on the right hand side of this equation we anticipate that the proto-RG amplitude equation will fail to capture certain terms that turn out in the multiple scales analysis.

It is known that the scaling $\tau = \epsilon t$ works for this problem [97]. Hence,

$$\begin{aligned} y' &\rightarrow (\partial_t + \epsilon\partial_\tau)y \\ y'' &\rightarrow (\partial_t^2 + 2\epsilon\partial_\tau\partial_t + \epsilon^2\partial_\tau^2)y, \end{aligned} \tag{A.2}$$

where the subscripts denote partial differentiation. Expanding y in a perturbation series

$$y = y_0 + \epsilon y_1 + \epsilon^2 y_2 + \ldots \tag{A.3}$$

we obtain

$$\begin{aligned}
\mathcal{O}(1) : (\partial_t^2 + 1) y_0 &= 0 \\
\mathcal{O}(\epsilon) : (\partial_t^2 + 1) y_1 &= -2\partial_\tau \partial_t y_0 + (1 - y_0^2)\partial_t y_0 \\
\mathcal{O}(\epsilon^2) : (\partial_t^2 + 1) y_2 &= -2\partial_\tau \partial_t y_1 + (1 - y_0^2)\partial_t y_1 - \partial_\tau^2 y_0 \\
&\quad -2y_0 y_1 \partial_t y_0 + (1 - y_0^2)\partial_\tau y_0.
\end{aligned} \tag{A.4}$$

From this we find

$$\begin{aligned}
y_0 &= A_{01}(\tau) e^{it} + \text{c.c.} \\
y_1 &= A_{11}(\tau) e^{it} + A_{13}(\tau) e^{3it} + \text{c.c.}
\end{aligned} \tag{A.5}$$

Application of the Fredholm alternative at $\mathcal{O}(\epsilon)$ and $\mathcal{O}(\epsilon^2)$ yields the following amplitude equations

$$\begin{aligned}
2i\partial_\tau A_{01} &= i A_{01} \left(1 - |A_{01}|^2\right) \\
\partial_\tau^2 A_{01} + 2i\partial_\tau A_{11} &= i \left(A_{11} - 2A_{11}|A_{01}|^2 - A_{01}^2 A_{11}^*\right) \\
&\quad + \partial_\tau \left(A_{01} - A_{01}|A_{01}|^2\right) + \frac{A_{01}|A_{01}|^4}{8}
\end{aligned} \tag{A.6}$$

which can be combined after scaling back to original variables to get

$$\partial_t^2 A + 2i\partial_t A = \epsilon \left[iA(1 - |A|^2) + \partial_t A(1 - |A|^2) \right] + \mathcal{O}(\epsilon^2). \tag{A.7}$$

Nozaki and Oono [88] on the other hand have obtained the following equation using the proto-RG method

$$\partial_t^2 A + 2i\partial_t A = \epsilon i A(1 - |A|^2) + \mathcal{O}(\epsilon^2). \tag{A.8}$$

Note that the missing term $\partial_t A(1 - |A|^2)$ can be captured by differentiating the lower order result, i. e.

$$2i\partial_t A = \epsilon i A(1 - |A|^2) \tag{A.9}$$

but this does not seem a very general approach. In particular, it is not obvious how this can be extended to PDEs.

The $\mathcal{O}(\epsilon)$ equation using the proto-RG method reads

$$y_1'' + y_1 = (1 - y_0^2)y_0', \tag{A.10}$$

where

$$\begin{aligned} y_0 &= Ae^{it} + \text{c.c.} \\ y_1 &= P(t)e^{it} + Qe^{3it} + \text{c.c.} \end{aligned} \tag{A.11}$$

where A can be a constant while P cannot. Thus, the proto-RG operator turns out to be

$$\mathcal{L} = \partial_t^2 + 2i\partial_t, \tag{A.12}$$

and the proto-RG equation reads

$$\mathcal{L}A = \epsilon \mathcal{L}P + \mathcal{O}(\epsilon^2), \tag{A.13}$$

where A is now the renormalized amplitude. When evaluating $\mathcal{L}P$ however, we allow for the possibility that A, which appears on the right hand side of the equation can also be a function of t, or equivalently renormalize A on the right hand side before differentiating

y_0, which gives us

$$\mathcal{L}P = \epsilon \left[iA(1 - |A|^2) + \partial_t A(1 - |A|^2) \right]. \tag{A.14}$$

Therefore the true amplitude equation should read (using Eq. A.13)

$$\mathcal{L}A = \epsilon \left[iA(1 - |A|^2) + \partial_t A(1 - |A|^2) \right] + \mathcal{O}(\epsilon^2), \tag{A.15}$$

which is identical to the multiple scales result of Eq. (A.7).

Appendix B

Discretization of Operators

B.1 Laplacian

The Laplacian of a function $f(x, y)$ is discretized at point $(x_i, y_j) = (i\Delta x, j\Delta x)$ using a nine point finite difference stencil as shown below, where Δx is the mesh spacing.

$$\begin{aligned} \nabla^2 f\big|_{i,j} &= \frac{f_{i+1,j} + f_{i-1,j} + f_{i,j+1} + f_{i,j-1}}{2\Delta x^2} + \frac{f_{i+1,j+1} + f_{i-1,j-1} + f_{i-1,j+1} + f_{i+1,j-1}}{4\Delta x^2} \\ &\quad -\frac{3f_{i,j}}{\Delta x^2} + \mathcal{O}(\Delta x^2). \end{aligned} \tag{B.1}$$

A Fourier transform of this *isotropic* discretization, described by Tomita in [126], is shown to very nearly follow the $-k^2$ isocontours.

B.2 Gradient

The gradient of a function $f(x, y)$ is discretized at point $(x_i, y_j) = (i\Delta x, j\Delta x)$ using a nine point second order finite difference stencil as shown below, where Δx is the mesh spacing. The stencil is designed to minimize effects of grid anisotropy which can introduce

artifacts in the solution, especially on adaptive grids. We have

$$\begin{aligned}\nabla f|_{i,j} &= \widetilde{\nabla}_{\oplus} f\Big|_{i,j} + \mathcal{O}(\Delta x^2) \\ &= \left(\frac{f_{i+1,j} - f_{i-1,j}}{2\Delta x}\right)\vec{i} + \left(\frac{f_{i,j+1} - f_{i,j-1}}{2\Delta x}\right)\vec{j} + \mathcal{O}(\Delta x^2). \end{aligned} \tag{B.2}$$

But

$$\nabla f = \left(\frac{f_x + f_y}{\sqrt{2}}\right)\left(\frac{\vec{i}+\vec{j}}{\sqrt{2}}\right) + \left(\frac{-f_x + f_y}{\sqrt{2}}\right)\left(\frac{-\vec{i}+\vec{j}}{\sqrt{2}}\right) \tag{B.3}$$

and hence we also have

$$\begin{aligned}\nabla f|_{i,j} &= \widetilde{\nabla}_{\otimes} f\Big|_{i,j} + \mathcal{O}(\Delta x^2) \\ &= \left(\frac{f_{i+1,j+1} - f_{i-1,j-1}}{2\sqrt{2}\Delta x}\right)\left(\frac{\vec{i}+\vec{j}}{\sqrt{2}}\right) + \left(\frac{f_{i-1,j+1} - f_{i+1,j-1}}{2\sqrt{2}\Delta x}\right)\left(\frac{-\vec{i}+\vec{j}}{\sqrt{2}}\right) + \mathcal{O}(\Delta x^2) \\ &= \left(\frac{f_{i+1,j+1} - f_{i-1,j-1} - f_{i-1,j+1} + f_{i+1,j-1}}{4\Delta x}\right)\vec{i} \\ &\quad + \left(\frac{f_{i+1,j+1} - f_{i-1,j-1} + f_{i-1,j+1} - f_{i+1,j-1}}{4\Delta x}\right)\vec{j} + \mathcal{O}(\Delta x^2). \end{aligned} \tag{B.4}$$

Using the discrete forms for the gradient in Eqs. (B.2) and (B.4) we can write the isotropic second order discretization as

$$\nabla f|_{i,j} = \frac{1}{2}\left(\widetilde{\nabla}_{\oplus} f\Big|_{i,j} + \widetilde{\nabla}_{\otimes} f\Big|_{i,j}\right) + \mathcal{O}(\Delta x^2). \tag{B.5}$$

A discretization scheme similar to Eq. (B.5) is given by Sethian and Strain [127].

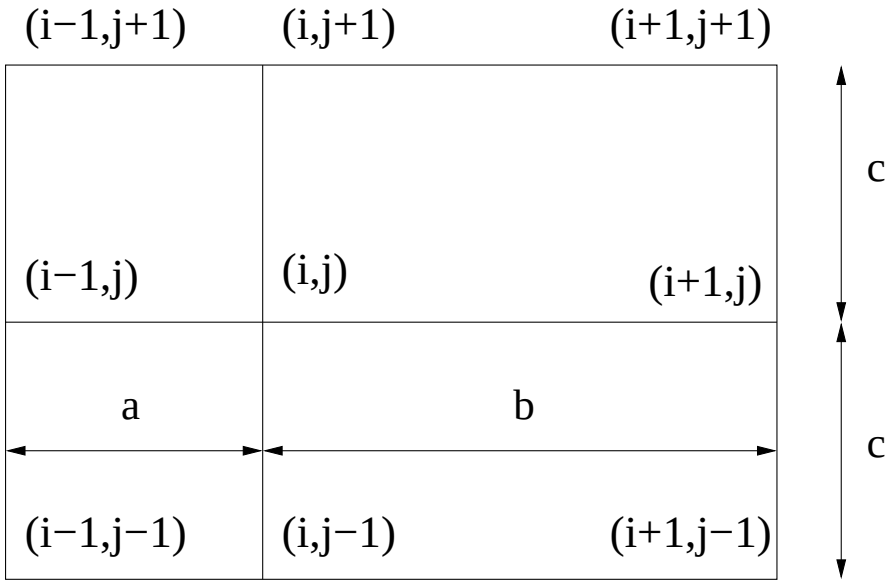

Figure B.1: Schematic showing the node neighbors surrounding a typical node (i, j), on a 1-D non-uniform grid.

B.3 Laplacian on a 1-D non-uniform grid

The Laplacian of a function $f(x, y)$ is discretized at point (x_i, y_j), shown in Fig. B.1, using a nine point finite difference stencil as shown below.

$$\begin{aligned}\nabla^2 f\big|_{i,j} &= C_1 f_{i+1,j} + C_2 f_{i-1,j} + C_3 f_{i,j+1} + C_4 f_{i,j-1} \\ &\quad + C_5 f_{i+1,j+1} + C_6 f_{i+1,j-1} + C_7 f_{i-1,j-1} + C_8 f_{i-1,j+1} \\ &\quad - \Sigma_{k=1}^{8} C_k f_{i,j} + \mathcal{O}(a^2, b^2, c^2) \end{aligned} \tag{B.6}$$

where

$$\begin{aligned} C_1 &= \frac{1}{a^2 + ab}, & C_2 &= \frac{1}{ab + b^2} \\ C_3 = C_4 &= \frac{1}{c^2} - \frac{1}{2ab}, & C_5 = C_6 &= \frac{1}{2\,(a^2 + ab)} \\ C_7 = C_8 &= \frac{1}{2\,(ab + b^2)}, & \Sigma_{k=1}^{8} C_k &= \frac{1}{ab} + \frac{2}{c^2}. \end{aligned} \tag{B.7}$$

It is easily verified that Eq. (B.6) reduces to Eq. (B.1) for the special case of a uniform grid where $a = b = c = \Delta x$.

B.4 Gradient on a 1-D non-uniform grid

The gradient of a function $f(x, y)$ is discretized at point (x_i, y_j), shown in Fig. B.1, using the following four point second order finite difference stencil

$$\nabla f|_{i,j} = \left(\frac{a}{b(a+b)} f_{i+1,j} + \frac{b-a}{ab} f_{i,j} - \frac{b}{a(a+b)} f_{i-1,j} \right) \vec{i} + \left(\frac{f_{i,j+1} - f_{i,j-1}}{2c} \right) \vec{j} + \mathcal{O}(a^2, b^2, c^2). \tag{B.8}$$

Again, it can be verified that Eq. (B.8) reduces to Eq. (B.2) for the special case of a uniform grid where $a = b = c = \Delta x$.

Vita

Badri Athreya was born on February 28, 1979 in Madras, India. He obtained his Bachelor's degree in Mechanical Engineering from Victoria Jubilee Technical Institute, Bombay, in 2000, and his Master's degree in Mechanical Engineering from the University of Colorado at Boulder in 2002, after which he joined Professor Jon Dantzig's group in the Mechanical Engineering Department at UIUC. His research is co-supervised by Professor Nigel Goldenfeld in the Department of Physics.

Upon graduation, Badri will join the technical center in Caterpillar, Peoria, IL, as senior engineer.